

# A Study of the Pyramid Sensor: Analytic Theory, Simulation and Experiment

by  
Jeffrey Matthew LeDue  
B.Sc., Dalhousie University, 2002

A Thesis Submitted in Partial Fulfillment of the  
Requirements for the Degree of  
MASTER OF SCIENCE  
in the Department of Physics and Astronomy

© Jeffrey Matthew LeDue, 2005  
University of Victoria.

*All rights reserved. This dissertation may not be reproduced in whole or in part,  
by photocopying or other means, without the permission of the author.*

# Abstract

The Pyramid Sensor (PS) is a promising wavefront sensor (WFS) for astronomical adaptive optics (AO) due to its potential to increase the number of accessible scientific targets by more efficiently using guide star (GS) photons. This so-called magnitude gain, as well as the key role played by the PS in several novel multi-reference wavefront sensing schemes have generated intense interest in the device. The diffraction based theory of PS and the underlying optical shop test, the Foucault knife-edge test, is reviewed. The theory is applied to calculate the magnitude gain. The impact of the magnitude gain on the number of galaxies accessible to observation with classical AO on a TMT sized telescope for the Virgo Cluster Catalogue is assessed via simulations. Additional simulation results are shown to elucidate the impact of various parameters of the pyramidal prism on the magnitude gain. The results of experiments conducted in the UVIC AO lab with a prototype 1d PS are discussed. The 1d PS uses a novel optical element called a holographic diffuser to linearize the response of the PS to wavefront tilt. The results of calibrating the sensor are given as well as caveats to the use of such a device. The results of using the 1d PS to measure a static aberration as well as spatial and temporal characterization of turbulence produced by the UVIC AO lab's Hot-Air Turbulence Generator are given.

# Contents

<b>List of Figures</b>	<b>v</b>
<b>List of Tables</b>	<b>ix</b>
<b>Abstract</b>	<b>xii</b>
<b>Acknowledgements</b>	<b>xiii</b>
<b>List of Abbreviations</b>	<b>xiv</b>
<b>1 Introduction</b>	<b>1</b>
1.1 Background: AO, ELT's and the PS . . . . .	1
1.1.1 Adaptive Optics: From Babcock to ELT's . . . . .	1
1.1.2 The Pyramid Sensor . . . . .	4
1.2 Objectives of the thesis project . . . . .	6
<b>2 Pyramid Sensor Theory and on-going developments</b>	<b>9</b>
2.1 Fourier Optics AO Model . . . . .	10

## CONTENTS

iii

---

2.1.1	Principle . . . . .	10
2.1.2	Open loop VS Closed loop fundamental equation . . . . .	12
2.2	Fourier Optics Modeling of the PS . . . . .	17
2.2.1	Geometrical Discussion of the Knife-Edge Test and the PS . . . . .	17
2.3	Diffraction Theory of the Knife-Edge Test . . . . .	19
2.3.1	A Discussion of Modulation . . . . .	29
2.3.2	Expectation of a Magnitude Gain . . . . .	31
2.3.3	Unification of R. Conan's Work with CAOS techniques . . . . .	38
2.4	Signal Variance and Sensor Noise . . . . .	50
2.5	An Alternative to the pyramid . . . . .	53
2.5.1	Amplitude Modulated PS: Simulation . . . . .	54
2.5.2	Analytic Signal Equations . . . . .	56
2.6	Generalization of the PS technique to focal plane masks and the Zernike Phase contrast method . . . . .	57
<b>3</b>	<b>Guide Star Counts and Interfacing PAOLA with Catalogues</b>	<b>59</b>
3.1	Searching the USNO catalogue . . . . .	59
3.2	Simulation Results . . . . .	61
3.3	Caveats to the Guide Star Search . . . . .	65
<b>4</b>	<b>Laboratory work with 1d Pyramid Wavefront Sensor</b>	<b>66</b>
4.1	Design and Layout . . . . .	67

## CONTENTS

---

iv

4.1.1	Component Considerations . . . . .	67
4.1.2	Zemax Layout . . . . .	70
4.2	Calibration . . . . .	74
4.2.1	Principle . . . . .	74
4.2.2	Laboratory Setup and Data Collection . . . . .	77
4.2.3	Data Analysis and Results . . . . .	79
4.2.4	Caveats to Modulation using a Holographic Diffuser . . . . .	84
4.3	Measurement of a Static Aberration . . . . .	86
4.3.1	Principle, Setup, Data Collection and Analysis . . . . .	88
4.3.2	Results . . . . .	89
4.4	Dynamic Characterization of the PS . . . . .	94
4.4.1	Principle of characterization of real turbulence . . . . .	95
4.4.2	Laboratory Setup and Data Collection . . . . .	102
4.4.3	Data Analysis and Results . . . . .	106
4.5	1d PS with no Diffuser . . . . .	124
4.6	Other Data Products . . . . .	127
4.6.1	Turbulator Heating Curves . . . . .	127
4.6.2	Static Tilts in the Turbulator . . . . .	128
4.6.3	Further Temporal Analysis . . . . .	132
4.6.4	Air flow in the Vertical Turbulator . . . . .	135

---

<b>5</b>	<b>Conclusions and Outlook</b>	<b>138</b>
5.1	The Magnitude Gain . . . . .	138
5.2	Static Modulation with a Diffuser . . . . .	139
5.3	Modulation by Atmospheric Turbulence . . . . .	141
5.4	Open Loop Measurements of Turbulence . . . . .	142
5.5	NextGen: PS and Turbulator . . . . .	143
5.5.1	Future PS Research . . . . .	143
5.5.2	Turbulator Development . . . . .	145
<b>A</b>	<b>PS Signal Variance Derivation</b>	<b>148</b>
<b>B</b>	<b>Parameters of the Data Sets</b>	<b>152</b>
<b>C</b>	<b>Data Tables: Temporal Parameters</b>	<b>156</b>
<b>D</b>	<b>Data Tables: Spatial Parameters</b>	<b>159</b>
<b>E</b>	<b>Other Data Products</b>	<b>167</b>

# List of Figures

2.1	Open Loop and Closed Loop Configurations . . . . .	13
2.2	Schematic Diagram of AO in Closed Loop . . . . .	15
2.3	Timing Diagram for AO loop . . . . .	16
2.4	Schematic of Knife-Edge test for an Aberrated Lens . . . . .	17
2.5	Schematic Diagram of 1d PS using a Prism . . . . .	18
2.6	Rayleigh Ring Observed with the 1d PS . . . . .	20
2.7	Cross Section of the Rayleigh Ring . . . . .	21
2.8	Observed Bright and Dark regions of the re-imaged pupil . . . . .	22
2.9	Appearance of Re-imaged Pupils for a Segmented Aperture . . . . .	23
2.10	Delta Function Phase Error . . . . .	25
2.11	Magnitude Gain, Ragazzoni and Farinato, 1999 . . . . .	33
2.12	Magnitude Gain, C. Vérinaud, 2004 . . . . .	35
2.13	Magnitude Gain, calculated using R. Conan 2d Model . . . . .	37
2.14	Functional Form of the Reconstructors . . . . .	39
2.15	Schematic of the pyramid roof . . . . .	43

---

2.16	Signal Degradation due to Pyramid Roof . . . . .	44
2.17	Re-imaged pupils in the presence of a roof . . . . .	46
2.18	Effect of Pupil Separation . . . . .	47
2.19	Cross-talk between the Re-imaged Pupils . . . . .	49
2.20	Amplitude Modulated PS Response to Tilt . . . . .	55
2.21	Zernike Phase Contrast WFS Simulation . . . . .	58
3.1	Flow chart of PAOLA catalogue interface . . . . .	60
3.2	Limiting Magnitude for a SH WFS on a 30 m Telescope . . . . .	62
3.3	Strehl Ratio Histogram for VCC Galaxies . . . . .	64
4.1	Schematic Diagram of the PS with a diffuser . . . . .	67
4.2	Zemax Layout of 1d PS . . . . .	71
4.3	Zemax Calculation of the Re-imaged pupil . . . . .	73
4.4	Demonstration of 1d Sensitivity . . . . .	74
4.5	Calibration Setup . . . . .	75
4.6	Mini-Wavescope Calibration Procedure . . . . .	78
4.7	Calibration Curve for 0.5° Diffuser . . . . .	81
4.8	Histogram of the Calibration Constant for the 0.5° Diffuser . . . . .	82
4.9	Calibration Curve for 1.0° Diffuser . . . . .	83
4.10	PS Pupil image from the PS CCD with the 0.5° diffuser . . . . .	84
4.11	Scatter plot of sensitivity and intensity . . . . .	87

---

4.12	Wavefront tilt measured with PS and mini-Wavescope . . . . .	90
4.13	Scatter Plot of Tilt Measurements . . . . .	91
4.14	Tilt Measurements, subaperture by subaperture . . . . .	92
4.15	Photograph of Bench Setup . . . . .	103
4.16	Schematic of Bench Setup . . . . .	104
4.17	Direct Fourier Transform vs Auto-Correlation . . . . .	109
4.18	Temporal Power Spectrum Comparison, $\Delta T = 140$ , Data Set 1 . . . . .	112
4.19	Temporal Power Spectrum Comparison, $\Delta T = 140$ , Data Set 2 . . . . .	113
4.20	Change in Variance of Zernike Coefficients with Array Size . . . . .	115
4.21	Variances of Zernike Coefficients, $\Delta T = 140$ . . . . .	117
4.22	Spatial Characterization Using PS, $\Delta T = 140$ . . . . .	118
4.23	Fried Parameter dependence on $\Delta T$ . . . . .	120
4.24	Temperature dependence of the Outer Scale . . . . .	121
4.25	Temperature dependence of the Inner Scale . . . . .	123
4.26	Temperature dependence of $r_0$ for PS without the diffuser . . . . .	125
4.27	Turbulator Heating Curve . . . . .	126
4.28	Static Modes in the Turbulator . . . . .	129
4.29	Temporal Power Spectrum, Data Set 2, $\Delta T = 40$ . . . . .	131
4.30	Temporal Power Spectrum, Data Set 2, Wind 900 . . . . .	133
4.31	Air flow restriction in the vertical turbulator . . . . .	136

---

5.1 Set-up for Integration and Testing of SE's . . . . . 144

B.1 Schematic of Horizontal and Vertical turbulators . . . . . 153

E.1 Variac setting dependence on fan speed ( $\Delta T \sim 40^\circ\text{C}$ ) . . . . . 168

E.2 Temporal Power Spectra calculated for Runs  $\Delta T = 40, 600, 750$  . . . 169

E.3 Temporal Power Spectra calculated for Runs Wind 900, 105, 120 . . . 170

# List of Tables

2.1	Summary of Variables and Parameters used in AO Modeling . . . . .	12
2.2	Description of Simulations in Buechler Costa et al., 2003 . . . . .	31
3.1	Number of Accessible Galaxies at Different Limiting Magnitudes . . . . .	63
3.2	Bahcall and Soneira Star Densities . . . . .	65
4.1	Description of Equipment Used . . . . .	76
4.2	Calibration Slope, 1° Diffuser . . . . .	80
4.3	Zernike Coefficients of CD Cover Aberration . . . . .	88
4.4	Zernike–Kolmogorov Covariance Matrix . . . . .	97
4.5	Zernike Derivative Matrix . . . . .	100
4.6	Temporal Power Spectrum . . . . .	110
4.7	Summary of Wind Speed Experiment Parameters . . . . .	134
4.8	Results of the Airflow Experiments . . . . .	135
B.1	Data Set 1 (Horizontal Turbulator) . . . . .	154
B.2	Data Set 2 (Vertical Turbulator) . . . . .	155

---

C.1	Data Set 1 Temporal Power Spectra Parameters, PS with no Diffuser	156
C.2	Temporal Power Spectra Parameters, mini-Wavescope . . . . .	157
C.3	Temporal Power Spectra Parameters, PS . . . . .	158
D.1	Spatial Parameters Calculated using the PS with no diffuser . . . . .	160
D.2	Zernike2Seeing Results, mini-Wavescope . . . . .	161
D.3	Hill-Andrew Results, mini-Wavescope . . . . .	162
D.4	Zernike2Seeing Results, PS 7x7 . . . . .	163
D.5	Slope Variance Parameters, PS 7x7 . . . . .	164
D.6	Zernike2Seeing Results, PS 14x14 . . . . .	165
D.7	Slope Variance Parameters, PS 14x14 . . . . .	166

# Acknowledgements

First, I would like to thank Dr. David Crampton and Dr. Colin Bradley for furnishing me with the opportunity to pursue my M.Sc. within the wider context of the VLOT study and the TMT project. The experiences I have gained in the course of my time at UVIC and HIA have truly made me appreciate the multi-disciplinary nature and unprecedented scale on which 21st century scientific endeavor is (beginning) to take place.

I would like to acknowledge and thank Dr. Laurent Jolissaint for his guidance and support in the course of my studies. He has been a scientific mentor as well as a friend. I am also indebted to Dr. Christophe Vérinaud for sharing his ideas while working with me in Heidelberg and Dr. Rodolphe Conan for sharing his work and sharp mathematical insights with me. I would also like to thank Dr. Jean-Pierre Véran for his interest in, and enthusiasm for my project.

I would like to thank my fellow Astronomy grad students at UVIC for moral support over the past few years. For financial support, I acknowledge NSERC, the NRC GSSSP program, HIA and UVIC.

On a personal note, I would like to thank my parents, John and Rita LeDue for their support during my time in Victoria. I am grateful to my sister, Emily, for her help during the six weeks she spent in Victoria while my leg was healing. Lastly, I want to thank Sarah Burke for her love and encouragement, as well as poignant scientific discussions and careful reading of my typescript.

# List of Abbreviations

ALFA	Adaptive Optics with a Laser for Astronomy
AO	Adaptive Optics
CAOS	Code for Adaptive Optics Systems
CASCA	Canadian Astronomical Society
CCD	Charge Coupled Device
CFHT	Canada-France-Hawaii Telescope
DM	Deformable Mirror
ELT	Extremely Large Telescope
ESO	European Southern Observatory
FFT	Fast Fourier Transform
FWHM	Full-Width at Half Maximum
GS	Guide Star
HIA	Herzberg Institute of Astrophysics
IDL	Interactive Data Language
LBT	Large Binocular Telescope
LGS	Laser Guide Star
LSD	Light Shaping Diffuser
LO	Layer-Oriented
LO-MCAO	Layer-Oriented Multi-Conjugate Adaptive Optics
MAD	Multi-Conjugate Adaptive Optics Demonstrator
MCAO	Multi-Conjugate Adaptive Optics
MEMS	Micro-Electromechanical Systems
MMT	Multiple Mirror Telescope

---

MOAO	Multi-Object Adaptive Optics
MPIA	Max Planck Institute for Astronomy
NED	NASA Extragalactic Database
NRC	National Research Council of Canada
OTF	Optical Transfer Function
OWL	Overwhelmingly Large Telescope
PAOLA	Performance of Adaptive Optics for Large (little) Apertures
POC	Physical Optics Corporation
PS	Pyramid Wavefront Sensor
PSD	Power Spectral Density
PSF	Point Spread Function
PV	Peak-to-Valley
PYRAMIR	Pyramid Wavefront Sensor for the Infrared
RMS	root-mean-square
RSI	Research Systems Incorporated
SE	Star Enlarger
SH	Shack-Hartmann
SH WFS	Shack-Hartmann Wavefront Sensor
SLODAR	Slope Detection and Ranging
SNR	Signal-to-Noise Ratio
SR	Strehl Ratio
SVD	Singular Value Decomposition
TMT	Thirty Meter Telescope
TNG	Telescopio Nazionale Galileo
UNSO	United States Naval Observatory
UVIC	University of Victoria
VCC	Virgo Cluster Catalogue
VLOT	Very large Optical Telescope
VLT	Very Large Telescope
WFAO	Wide Field Adaptive Optics
WFS	Wavefront Sensor

# Chapter 1

## Introduction

### 1.1 Background: AO, ELT's and the PS

#### 1.1.1 Adaptive Optics: From Babcock to ELT's

The imaging quality of large astronomical telescopes is limited by the turbulent atmosphere. Resolution ('seeing') is not typically better than  $0.5''$  at the best astronomical sites. This is  $\sim 40$  times the diffraction limited image size of a 10 m class telescope. Adaptive Optics (AO) attempts to correct, in real-time, for the distortion induced by the turbulence in the incoming wavefront from the astronomical object of interest, and thereby enable the telescope to reach diffraction-limited image quality. AO was first proposed by Babcock in 1953 as a method for compensating for astronomical seeing, and the basic operating principle has not changed since then. The AO system uses a wavefront sensor which relies on the light of a guide star (GS) to make measurements of the perturbations introduced by the atmosphere into an otherwise flat wavefront coming from a distant astronomical object. These measurements feed a control system which drives a deformable mirror (DM) into a shape that removes the atmospheric distortions. Thus, the light reflected from the DM delivers high quality, diffraction-limited imaging to the science instruments and cameras (Tyson, 1998).

The first astronomical images at the diffraction limit were attained in 1989 with the COME-ON system by a French team at Observatoire Haute Provence on a 1.58 m telescope. The system was then tested on a 3.6 m telescope (Rigaut et al., 1991). AO systems eventually became facility class instruments on 4 m class telescopes, including the CHFT Adaptive Optics Bonnette (PUEO) (Crampton, 1999).

The limitations of the technique were perceived early on in the development of AO. The necessity of a bright GS to perform wavefront sensing limits the percentage of the sky accessible to observation with AO (the sky coverage) to  $\sim 1\%$  at K band (Beckers, 1993). In addition to this the guide star must be close to the astronomical target as the correction degrades with increasing separation, an effect known as anisoplanatism (Fried, 1982).

Despite the limitations, the enormous promise of AO pushed development in new directions. To extend the sky coverage it was suggested that a synthetic beacon be generated using back-scattered laser light from high altitude atmospheric layers (Foy and Labeyrie, 1985). Such a laser guide star (LGS) could, in principle, be generated at any position in the sky, eliminating the restriction of a bright natural GS and allowing AO to achieve 100% sky coverage. Unfortunately, this is not the the case for two main reasons: the global tilt of the wavefront cannot be recovered from LGS measurements, making a faint natural GS necessary and, due to the finite height of the synthetic beacon, the path of the LGS light shares a smaller volume of turbulent atmosphere with the target than would a natural GS (Rigaut and Gendron, 1992). This later issue is referred to as the cone effect or focal anisoplanatism (Tallon and Foy, 1990). Despite these challenges LGS's were demonstrated in the early 1990's and are now in use, for example the LGS AO system at the Lick Observatory's Shane 3 m telescope (Murphy et al., 1991).

To increase the size of the corrected field, the idea of multi-conjugate adaptive optics (MCAO) was put forth (Beckers, 1988; Beckers, 1989; Merkle and Beckers, 1989). MCAO widens the corrected field by using multiple guide stars in different directions, sensed by the an equal number of wavefront sensors, to drive at least two DM's conjugated to different altitudes. MCAO represents a significant increase in complexity over classical AO. The technique immediately poses interesting questions: What is

the performance across the corrected field and what is its angular size?, What are the optimal conjugation heights of the DM's?, How many GS's (laser and natural) are necessary?, and What is the optimal asterism? These issues have been addressed by simulation over the years (Johnston and Welsh, 1994; Ellerbroek, 1994; Femenia et al., 2002; Femenía and Devaney, 2003). In practice, the answers to these questions are unknown as MCAO has not yet been tested on the sky.

Combining the two techniques, LGS's and MCAO, one could imagine the possibility of diffraction-limited performance over a large field anywhere on the sky. Simulations have shown a Strehl Ratio of  $\sim 0.5$  which is nearly constant over a  $0.5'$  field in J band for an MCAO system employing 5 LGS's on an 8 m telescope (Le Louarn, 2002).

Currently there are many successful AO systems running on 10 m class telescopes, including the Keck Observatory and Gemini North (Wizinowich et al., 2000; Stoesz et al., 2004b). Astronomers and astrophysicists are now thinking about the next generation of giant astronomical telescopes which will serve to complement the science accessible with the James Webb Space Telescope and the Atacama Large Millimeter Array (CASCA, 2005). In fact, CASCA is recommending that an investment of \$125 million be made in the Thirty Meter Telescope (TMT) project. Many Extremely Large Telescope (ELT) studies exist, such as the TMT, the Overwhelmingly Large Telescope (OWL), and the Euro50. The massive scale of these telescopes has put forth an enormous challenge to the AO community in solving the technical and engineering problems associated with performing AO correction on an ELT. The kinds of devices required, WFS CCD's with grids of  $2500 \times 2500$  pixels, DM's having 500 000 actuators, and computers capable of  $10^6$  Gflops, do not yet exist (Rigaut et al., 2000; Le Louarn et al., 2000).

The challenges presented by ELT's have led to the exploration of more novel AO modes such as Wide Field Adaptive Optics (WFAO) and Multi-Object Adaptive Optics (MOAO) which is being implemented at VLT with the FALCON instrument (Rigaut, 2002; Hammer et al., 2004). WFAO attempts to provide an improved seeing over a large field-of-view, suitable for multi-object spectroscopy, using only one DM. On the other hand, MOAO attempts to provide diffraction-limited performance locally, around the objects of interest, in a large field-of-view.

The large aperture of ELT's may produce the side effect of increasing the sky coverage with natural GS's compared to LGS's. It has been suggested that the diameter at which an ELT reaches 90% sky coverage with natural GS's alone is between 50 and 100 m for a WFS capable of using 14th magnitude GS's (Ragazzoni, 1999). However, regardless of whether natural GS's or LGS's are used to provide the necessary WFS measurements, the technological problems associated with performing multi-reference wavefront sensing for ELT's has led to a great deal of interest in Layer-Oriented wavefront sensing and a new type of WFS which is particularly well suited to this technique, the pyramid sensor (Ragazzoni, 2000; Ragazzoni et al., 2000a).

### 1.1.2 The Pyramid Sensor

The pyramid wavefront sensor (PS) grew out of efforts to develop pupil plane wavefront sensors based on focal plane filters by building instruments that provided quantitative measurements from familiar optical shop tests (Wilson, 1975; Horwitz, 1978). The PS is based on the Foucault knife-edge test and a WFS based on this test, using crossed bi-prisms as the focal plane filter, was suggested in the mid-1990's (Pugh et al., 1995). Pugh et al., 1995 carried out a computer simulation to determine the tilt response as well as ray tracing of a potential optical design. The PS was first proposed in its more familiar form, i.e., employing a pyramidal prism as the focal plane filter, by Ragazzoni in 1996, and its subsequent development has largely been driven by his research group and collaborators. Initially, the interest in this device came from theoretical and simulation studies that suggested it could provide the needed measurements of the wavefront slope at a given SNR using fewer photons than the more conventional Shack-Hartmann wavefront sensor (SH WFS) (Ragazzoni and Farinato, 1999; Esposito and Riccardi, 2001). The benefit of this is that an AO system employing a PS could function using a fainter GS. This gain in limiting magnitude increases the sky coverage, addressing one of AO's main limitations.

However, as the focus of AO shifted to more ambitious projects involving MCAO, a variant of MCAO, based on the PS, called Layer-Oriented MCAO (LO-MCAO) was proposed (Ragazzoni, 2000; Ragazzoni et al., 2000a). In this scheme, DM's

conjugated to different altitudes are driven independently of each other by WFS measurements at those same conjugate altitudes. The PS is well suited to this task because, as the wavefront sensor signals are derived from images of the pupil, it lends itself to allowing the light of multiple GS's to be optically co-added on the detector. This reduces the amount of read noise introduced into the system by CCD's as well as allows the light from faint GS's, that would not normally be usable, to contribute to the signal. This technique has been shown analytically to be stable in closed loop and to be equivalent to the classical MCAO approach (Diolaiti et al., 2001). This technique was also extended to Multiple field-of-view LO-MCAO (Ragazzoni et al., 2002a). In this case the GS within the inner part of the field-of-view are used to drive a low altitude DM, while the stars in the outer portion are used to drive a higher altitude DM. This allows an optimization of the SNR for the two heights and leads to a sky coverage of up to nearly 100% at low galactic latitudes and  $\sim 50\%$  at high galactic latitudes if low read noise detectors are used.

Interest in the promising Layer-Oriented concept has fueled further development of PS techniques and AO systems using them. These include the European Southern Observatory's Multi-Conjugate Adaptive Optics Demonstrator (MAD) and the LINC-NIRVANA project at the Large Binocular Telescope (LBT) (Ragazzoni et al., 2001). MAD is a test instrument designed for VLT which is capable of performing MCAO using both the usual (Star-Oriented) and LO techniques. The LBT is an ambitious project consisting of two 8.4 m telescope on the same mount. Each telescope will be equipped with an MCAO system employing LO techniques.

Another interesting PS project is being undertaken at the Max Planck Institute for Astronomy in Heidelberg. Here the interest is in using a PS designed for the infrared to increase the sky coverage of the AO system ALFA on the 3.5 m telescope of the German-Spanish Astronomical Center at Calar Alto (Costa et al., 2003a; Costa et al., 2004a; Costa et al., 2004b).

## 1.2 Objectives of the thesis project

The impetus for this project was to develop PS know-how for the NRC/UVIC AO collaboration through both theoretical and laboratory studies of this interesting device.

The Herzberg Institute of Astrophysics (HIA) is home to many of the scientists and engineers making high-level decisions within the framework of the TMT collaboration, and formerly the VLOT study. Simulation of the performance of new AO modes and new AO components, such as the PS, are of paramount importance to those deciding where to invest the project's resources. Much of the modeling effort at HIA for characterizing the performance of potential AO systems is carried out using the code PAOLA, which has been developed in house. An important step in assessing the potential impact of the PS on AO performance is the integration of the PS into this code. To achieve this, Fourier optics modeling of the PS is required to obtain an understanding of the sensor's noise propagation and aliasing properties. There have been recent developments to address this which has revived the diffraction theory of Schlieren optical tests (Malacara, 1978; V erinaud, 2004).

Studying the noise propagation of the PS would allow the magnitude gain to be calculated, and at this stage the science accessible to a system using a PS must be compared to that of a SH WFS. This requires an extension of PAOLA to enable it to search through catalogues to find guide stars around interesting astronomical targets. This would allow a direct comparison of the performance of a given AO system using a SH WFS and a PS for particular scientific applications, which is perhaps a more satisfying calculation than general sky coverage calculation based on general models of the distribution of stars in the galaxy, like that of Bahcall and Soneira, 1980.

In addition to the modeling, a PS was to be designed and tested in the UVIC AO lab to gain practical experience with the device. The UVIC AO lab has many interesting AO projects underway. A hot-air turbulence generator (turbulator) has been developed to provide a simulation of atmospheric turbulence for AO related experimentation (Keskin, 2003). It has been characterized in the past using an Angle-of-Arrival

Variance experiment and is currently being studied by SLODAR (Keskin et al., 2003; Jolissaint et al., 2004a). The lab has also set up a closed loop AO system to be used in conjunction with the turbulator as a simulation of a classical AO system on an 8 m telescope. This allows for development and testing of novel control systems designed in house (Hampton et al., 2003; Hampton et al., 2004).

As the PS is based on the Foucault knife-edge test, it is sensitive to the sign of the wavefront slope (Malacara, 1978). To enable the PS to give a linear measurement of tilt, it was first suggested that the position of the pyramid apex be modulated in the focal plane (Ragazzoni, 1996). Later a tip/tilt mirror was used to modulate the position of the focus relative to the pyramid apex (Riccardi et al., 1998). The time scale of this modulation is faster than the WFS CCD integration time and thus it serves to blur the focus over the four facets of the pyramid, and as a result the PS gives a linear response to tilt (Ragazzoni, 1996; Riccardi et al., 1998). Thus, the technique of modulation allows the PS to provide wavefront slope measurements, comparable to those of the SH WFS.

Modulation does not have to be accomplished dynamically and it has been suggested that a modulation effect could be provided by a static diffusing element which serves to blur the focal spot on the apex of the pyramid. The idea of static modulation had not been previously tested, and the PS for the UVIC AO lab was designed to use a holographic diffuser, called a Light Shaping Diffuser (LSD), from Physical Optics Corporation to provide modulation (Ragazzoni et al., 2002b). Thus, the first objective of the laboratory test was to calibrate the PS implemented with the diffuser and verify this calibration by measuring a static aberration. The next logical step of the PS characterization is to measure turbulence in open loop using the turbulator, and, as a final step, the PS could be integrated into the classical AO system. This would allow a study of the closed-loop behaviour of the PS.

It has also been suggested in the literature that the turbulence itself produces a modulating effect (Costa et al., 2003b). This is an attractive idea because it simplifies the optical design and reduces the complexity of the sensor, especially compared to dynamic modulation techniques which use moving parts to oscillate the pyramid or tilt the beam focused on the pyramid apex. This idea is readily investigated by removing the holographic diffuser.

## Chapter 2

# Pyramid Sensor Theory and on-going developments

There are intense simulation and modeling efforts being pursued in the field of AO. Two main streams of calculation exist: end-to-end Monte Carlo Simulations, and codes exploiting analytical results both from Fourier optics and turbulence theory. The goal of both techniques is to characterize the performance of the AO system and this typically means understanding the properties of the image plane given the atmosphere, telescope, and AO system.

There is a consensus that analytic codes, due to their speed, should be used as a first attempt to model a system. It can be argued that the analytical approach often leads to a deeper understanding of the system as its components must be boiled down to their essentials before an appropriate analytic representation is found. This being said there is no replacement for a thorough simulation to improve confidence in the results of a calculation or to provide the flexibility to handle many effects which lack tractable, analytical expression. Two main codes will be discussed throughout this chapter. These are CAOS and PAOLA. CAOS stands for ‘Code for Adaptive Optics Systems’ and employs a Monte Carlo method, and is mainly developed by European researchers (Carbillet et al., 2001; Carbillet et al., 2005). PAOLA stands for Performance of Adaptive Optics for Large (and Little) Apertures. The code has

been developed by L. Jolissaint and J. Stoesz at HIA, and the underlying analytic technique has been developed by many authors (Rigaut et al., 1998; Tokovinin and Viard, 2001; Conan et al., 2003; Jolissaint et al., 2005; Stoesz et al., 2004a).

The PS is just one component of the AO system, and an appropriate analytic formulation of it is continuing to be developed. Many authors have studied its properties both analytically and through simulation, and the expectation of a magnitude gain over the SH WFS has fueled development and research. Whether or not there is a magnitude gain and whether or not it can be realized and exploited in practice are open questions which the body of this chapter attempts to address.

## 2.1 Fourier Optics AO Model

### 2.1.1 Principle

Analytic modelling of AO systems relies on Fourier transform techniques. The Fourier domain model for classical AO systems takes as input the power spectral density (PSD) of the phase due to the turbulent atmosphere (see section 4.4.1), and, as output, it gives five error terms which contribute to the PSD of the corrected phase: fitting error, anisoplanatism, servo system lag, wavefront sensor (WFS) spatial aliasing, and WFS noise (Rigaut et al., 1998). This is accomplished through a decomposition of the phase into its high frequency (those frequencies not corrected by the DM) and low frequency (those frequencies corrected by the DM) components. Using the usual notation, where the high frequency terms are denoted by a  $\perp$  subscript and the low frequency terms are denoted by a  $\parallel$  subscript, the corrected phase,  $\varphi_c$ , is the difference of the incoming phase,  $\varphi$ ,

$$\varphi(\mathbf{x}, \boldsymbol{\alpha}) = \varphi_{\parallel}(\mathbf{x}, \boldsymbol{\alpha}) + \varphi_{\perp}(\mathbf{x}, \boldsymbol{\alpha}) \quad (2.1)$$

and the phase estimated by the AO system,  $\hat{\varphi}$ ,

$$\hat{\varphi}(\mathbf{x}) = \hat{\varphi}_{\parallel}(\mathbf{x}, 0) + \hat{\varphi}_{\parallel}^{alias}(\mathbf{x}) + \hat{\varphi}_{\parallel}^{noise}(\mathbf{x}). \quad (2.2)$$

Taking the difference of equation 2.1 and equation 2.2,  $\varphi_c(\mathbf{x}, \boldsymbol{\alpha})$  can be written as

$$\varphi_c(\mathbf{x}, \boldsymbol{\alpha}) = (\varphi_{\parallel}(\mathbf{x}, \boldsymbol{\alpha}) - \varphi_{\parallel}(\mathbf{x}, 0)) + (\varphi_{\parallel}(\mathbf{x}, 0) - \hat{\varphi}_{\parallel}(\mathbf{x})) - \hat{\varphi}_{\parallel}^{alias}(\mathbf{x}) - \hat{\varphi}_{\parallel}^{noise}(\mathbf{x}) + \varphi_{\perp}(\mathbf{x}, \boldsymbol{\alpha}). \quad (2.3)$$

The first term of equation 2.3 leads to the anisoplanatism error and the second term is the servo-lag error in equation 2.4. The last term in equation 2.3 is the fitting error term.

Taking modulus squared of the Fourier transform of equation 2.3 and, assuming that the error terms are uncorrelated, all of the cross terms can be neglected. Hence the PSD of the corrected phase is given by

$$W_{\varphi_c}(\mathbf{f}, \boldsymbol{\alpha}) = W_{fit}(\mathbf{f}) + W_{aniso}(\mathbf{f}, \boldsymbol{\alpha}) + W_{servo}(\mathbf{f}) + W_{alias}(\mathbf{f}) + W_{noise}(\mathbf{f}). \quad (2.4)$$

Integrating equation 2.4 over frequency space gives the variance of each error term which contributes to the overall wavefront variance

$$\sigma_{\varphi_c}^2(\boldsymbol{\alpha}) = \sigma_{fit}^2 + \sigma_{aniso}^2(\boldsymbol{\alpha}) + \sigma_{servo}^2 + \sigma_{alias}^2 + \sigma_{noise}^2. \quad (2.5)$$

The variance due to WFS noise is of particular interest in calculating the magnitude gain of the PS.

The properties of the image plane are calculated from the important result that the optical transfer function (OTF) of the corrected phase is the product of the OTF of the telescope and the OTF of the atmospheric turbulence filtered by the AO system. The OTF of the atmospheric turbulence filtered by the AO system is given by

$$OTF_{AO} = \exp\left(-\frac{1}{2}D_{\phi}(\lambda f)\right) \quad (2.6)$$

where  $D_{\phi}$  is the structure function of the atmospheric turbulence filtered by AO (Fried, 1966). It is given by

$$D_{\phi} = 4\pi \int_0^{\infty} (1 - J_0(\kappa x)) W_{\phi}(\kappa) \kappa d\kappa \quad (2.7)$$

symbol	decription	typical value
$\mathbf{x} = (x, y)$	position vector	-
$\mathbf{f} = (f_x, f_y)$	spatial frequency vector	-
$f$	magnitude of $\mathbf{f}$	-
$r_0$	Fried Parameter	.15 m @ V band
$\mathbf{v}_l$	wind velocity of layer $l$	10 m/s
$d$	DM actuator pitch, WFS sub-aperture size	.83 m
$t_i$	WFS integration time	1 ms
$\tau$	servo-lag time constant	1 ms
$D$	diameter of telescope primary	30 m
$\alpha$	vector from target to GS	$< 20''$

Table 2.1: **Summary of Variables and Parameters used in AO Modelling:**Typical values are presented where possible.

where  $\kappa = 2\pi f$ . Thus, the OTF can be calculated from the power spectrum,  $W_\phi$ , and the image plane point spread function (PSF) is the Fourier transform of the OTF (Jolissaint, 2003).

### 2.1.2 Open loop VS Closed loop fundamental equation

Typically AO systems operate in closed loop. This configuration is shown very schematically on the right hand side of figure 2.1. In closed loop the WFS measures the residual phase, i.e. it placed downstream of the DM in the optical path. This means that once the AO correction is operating effectively (the loop is closed) the WFS must measure small aberrations compared to those present in the incoming turbulent phase. The measurements made by the WFS drive the DM via the control system, and in this configuration the WFS measures the changes on the DM. In this way the WFS monitors the changes that are made by the control system and closed loop systems are stable for this reason. In closed loop the correction applied to the DM is usually scaled by a factor,  $g$ , called the loop gain. The gain is always less than one and limits the magnitude of the change made to the DM setting in one loop and thus contributes to the stability of the loop. The open loop configuration is shown in figure 2.1 on the left. In this system the WFS measures the incoming phase directly. In the derivation of the equations 2.3 and 2.4, the WFS measures the incoming phase,

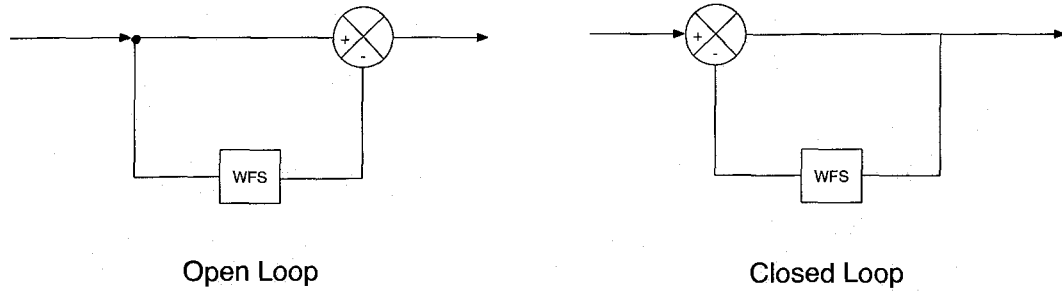


Figure 2.1: **Open Loop and Closed Loop Configurations:** In this diagram the lines present the incoming phase as it propagates through the AO system. In a closed loop system the DM, represented by the  $\otimes$  symbol, is upstream of the WFS in the optical path allowing the WFS to measure residuals. In an open loop system the incoming phase proceeds directly to both the DM and the WFS.

not the residual. This means that the model outlined in section 2.1.1 is technically open loop. In this section the possibly inclusion of closed effects in to the Fourier space model is considered.

### Loop gain

As mentioned above, equation 2.3 represents open loop AO, but it can also be seen as one step of a closed loop system with gain one. Including the loop gain,  $g$ ,  $\varphi_c$  is

$$\varphi_c = \varphi - g\hat{\varphi}. \quad (2.8)$$

This gives

$$\varphi_c(\mathbf{x}, \boldsymbol{\alpha}) = (\varphi_{\parallel}(\mathbf{x}, \boldsymbol{\alpha}) - \varphi_{\parallel}(\mathbf{x}, 0)) + (\varphi_{\parallel}(\mathbf{x}, 0)) - g\hat{\varphi}_{\parallel}(\mathbf{x}) - g\hat{\varphi}_{\parallel}^{alias}(\mathbf{x}) - g\hat{\varphi}_{\parallel}^{noise}(\mathbf{x}) + \varphi_{\perp}(\mathbf{x}, \boldsymbol{\alpha}) \quad (2.9)$$

as the counterpart to equation 2.3. It would be possible to simulate a closed loop system by iteratively passing the output PSD of each loop as the input to the next; however, this is not implemented in PAOLA.

### WFS Measurements

In order to develop the fundamental equation for a closed loop system it is necessary to understand the notation and framework in which WFS's are modeled in the Fourier domain. A WFS measurement,  $\mathbf{m}(\mathbf{x}, t)$ , is related to the signal provided by the WFS,  $\mathbf{S}(\mathbf{x}, t)$  by

$$\mathbf{m}(\mathbf{x}, t) = \mathcal{M}[\mathbf{S}(\mathbf{x}, t)] + \mathbf{n}(\mathbf{x}) \quad (2.10)$$

where the operator  $\mathcal{M}$  represents the process of making the measurement and  $\mathbf{n}(\mathbf{x})$  is the additive noise. The quantities  $\mathbf{m}$ ,  $\mathbf{S}$ , and  $\mathbf{n}$  are vectors with two components corresponding to the two sets of measurements provided by the WFS, i.e., the two components of the wavefront gradient at each point  $\mathbf{x}$  in the pupil. The  $\mathcal{M}$  includes the effect of WFS integration time, spatial filtering by the subapertures and sampling of the pupil by the subapertures. It is defined by

$$\mathcal{M}[\mathbf{S}(\mathbf{x}, t)] = \left( \frac{1}{t_i} \int_{-t_i/2}^{t_i/2} \mathbf{S}(\mathbf{x}, t - \tau) d\tau \otimes \Pi(\mathbf{x}/d) \right) III(\mathbf{x}/d) \quad (2.11)$$

where  $t_i$  is the integration time of the WFS detector,  $\otimes$  denotes convolution,  $\Pi$  is the two dimensional rectangle function,  $d$  is the subaperture size, and  $III$  is the two dimensional Dirac comb distribution (Rigaut et al., 1998).

In the Fourier domain, it is tractable to calculate an analytic function representing the controller which provides a least squares estimate of the phase from the WFS measurements. Stated mathematically the reconstruction operator (reconstructor) is

$$\tilde{\mathcal{R}}(\mathcal{M}[\mathbf{S}(\mathbf{x}, t)]) = \varphi_{\parallel}(\mathbf{x}; t). \quad (2.12)$$

The calculation of the reconstructor proceeds exactly as one might imagine: by minimizing the variance of the corrected, or residual phase. It is tractable for both the SH WFS and the PS because the signals of these sensors can be represented by analytic functions in the Fourier domain (under certain assumptions). The PS is discussed in section 2.3. For the SH WFS, the reader is referred to Rigaut et al., 1998.

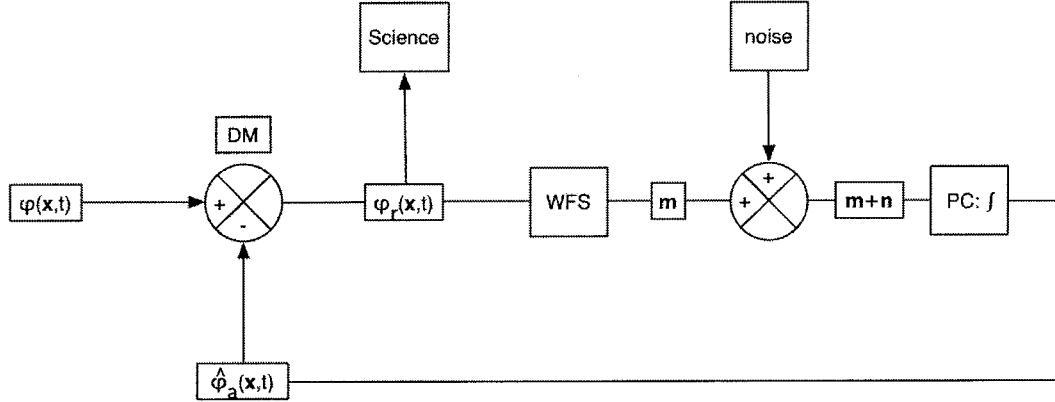


Figure 2.2: Schematic Diagram of AO in Closed Loop.

### Derivation of Closed loop fundamental equation

Figure 2.2 shows a schematic diagram of an AO loop. The incoming phase,  $\varphi(\mathbf{x}; t)$ , enters the system via the telescope and fore-optics. It reflects off the DM which is shaped to subtract the estimated atmospheric phase,  $\hat{\varphi}_a$ . This gives the residual or corrected phase,  $\hat{\varphi}_r$  or  $\hat{\varphi}_c$ , which is responsible for the image quality in the science instrumentation arm as well as the errors measured by the WFS. The fact that the WFS measures, or sees, the residual phase is important for two reasons. First and most importantly it allows the control system to function in closed loop, as the changes made by the DM contribute to the signals of the WFS. Secondly, it reduces the dynamic range needed by the WFS thereby increasing its potential sensitivity. However, the results of section 2.1.1 do not take into consideration the effect of having the WFS measure the residual phase. The following paragraphs describe a derivation of the ‘Fundamental Equation’ (equation 2.3) for this case.

The corrected phase is given by

$$\varphi_c(\mathbf{x}; t) = \varphi(\mathbf{x}, \alpha; t) - \hat{\varphi}_a(\mathbf{x}, \mathbf{0}; t) \quad (2.13)$$

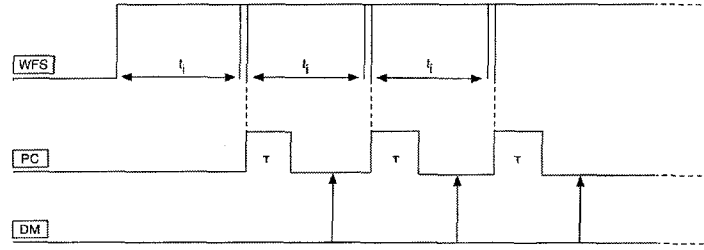


Figure 2.3: Timing Diagram for AO loop.

where the estimated atmospheric phase is

$$\hat{\varphi}_a(\mathbf{x}, \mathbf{0}; t) = \tilde{\mathcal{R}}(\mathbf{m} + \mathbf{n}) + \hat{\varphi}_a(\mathbf{x}, \mathbf{0}; t - t_i). \quad (2.14)$$

This can be seen clearly in figure 2.3. The current estimated phase is the sum of the reconstructed phase coming from the WFS measurements (corrupted by noise) and the previous DM setting one integration time of the WFS ago.

Repeating the analysis that leads to equation 2.3, gives a similar result with an additional term:

$$\varphi_c(\mathbf{x}, \boldsymbol{\alpha}) = \text{O.L. terms} + \frac{1}{t_i} \int_{t-t_i/2}^{t+t_i/2} \tilde{\mathcal{R}}\mathcal{M}[\mathcal{S}[\hat{\varphi}_a(\mathbf{x}, t - t_i/2 - \tau)]] dt - \hat{\varphi}_a(\mathbf{x}, t - t_i/2) \quad (2.15)$$

where the argument of the WFS signal has been included explicitly. This term is essentially the difference between the true DM shape,  $\hat{\varphi}_a(\mathbf{x}, t - t_i/2)$ , and what the WFS measures it to be. This term is not dominant for classical AO systems, or AO systems which plan to provide a moderate correction, i.e., Strehls of  $\sim 50\%$ . However, for extreme AO, where Strehls  $> 90\%$  are desired, this term could become important. Its inclusion into analytic models requires further research into the properties of the DM influence functions and the couplings between actuators (non-superposition), something which is being pursued at the UVIC AO lab.

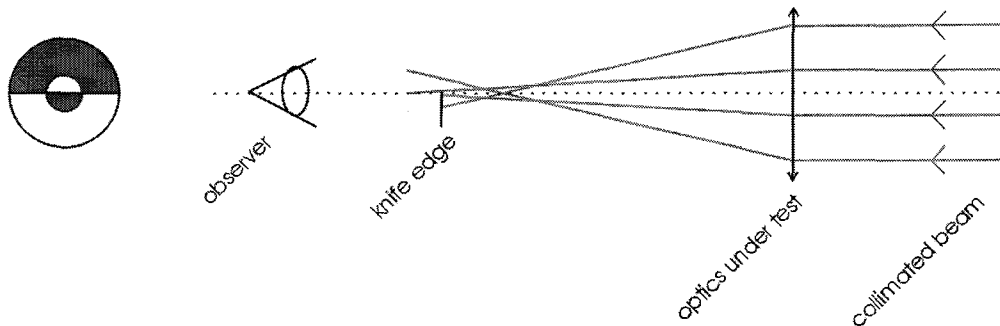


Figure 2.4: **Schematic of Knife-Edge test for an Aberrated Lens:** The is figure shows schematically the sorting of the rays in the focal plane by the knife edge. The example of a spherically aberrated lens is used. In this case rays passing through the lens at the edges focus at a point on the optical axis before the paraxial rays. This generates the shadow pattern seen by the observer shown schematically on the left.

## 2.2 Fourier Optics Modeling of the PS

### 2.2.1 Geometrical Discussion of the Knife-Edge Test and the PS

The Foucault knife-edge test is the optical shop test which underlies the PS. It was invented in 1858 by Foucault to test the optical quality of telescope primaries (Malacara, 1978). Figure 2.4 shows a schematic diagram of the knife-edge test, as it might be used to test a lens. The test is usually used to examine mirrors and in that case a point source is placed on one side of the optical axis and the knife edge is inserted into the focus directly on the opposite side of the optical axis. However, the configuration shown in figure 2.4 leads more naturally to the PS and demonstrates the same principles as the mirror testing configuration.

The idea of the knife-edge test is quite elegant in its simplicity. Geometrically all of

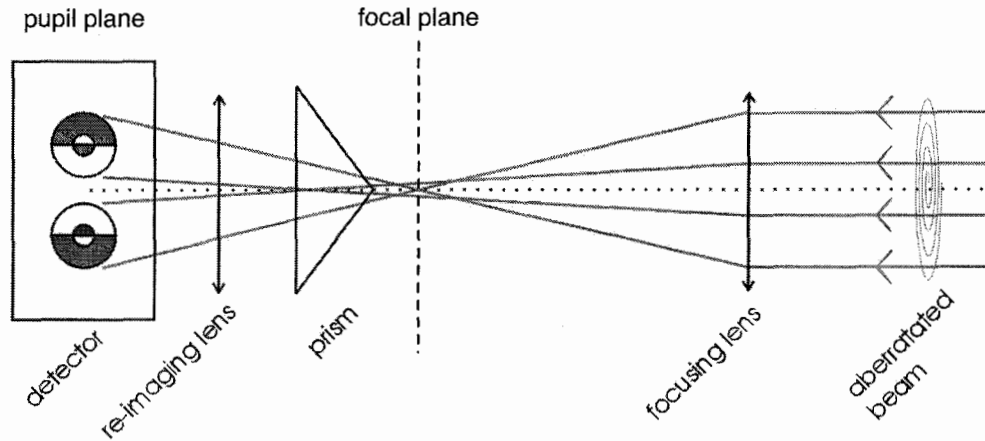


Figure 2.5: **Schematic Diagram of 1d PS using a Prism:** This diagram shows the same arrangement as figure 2.4, but this time for a 1d PS using a prism. The prism splits the light into two beams giving two shadow patterns captured by the detector.

the rays passing through a perfect lens would come to a focus at one point. Thus, if a knife edge is moved into the focal plane perpendicular to the optical axis, the observer will see the whole pupil illuminated and as soon as the knife edge reaches the focus the pupil will go dark. If an aberration is present, the knife edge inserted into the focus sorts the rays coming from various parts of the pupil. From the observer's perspective, regions of the pupil corresponding to rays blocked by the knife edge will appear dark. Figure 2.4 is meant to show schematically the situation for a lens with spherical aberration. The rays passing through the lens far from the optical axis come to a focus before the rays passing through the lens closer to the optical axis. In this case, the knife edge blocks rays coming from the top of the lens above the optical axis and rays passing through the lens closer to the optical axis but beneath it. This leads to the shadow pattern shown on the left.

The shadow patterns viewed by the observer are called Foucault graphs, and can be calculated from geometrical ray theory for all of the primary Seidel aberrations (focus, coma, astigmatism, and spherical aberration) (Malacara, 1978).

The situation is very similar for the PS. The knife edge is replaced by a refractive prism. In this case the prism sorts the rays but instead of blocking one side of the focal plane (and wasting photons) it splits the incoming beam into two beams. Each beam corresponds to one side of the focal plane. Figure 2.5 shows a schematic diagram of a PS. The lens of the human eye and the retina have been replaced with a lens which re-images the pupil corresponding to each beam onto a detector (CCD). The re-imaging lens provides an image of the pupil plane and thus the detector is conjugate to the entrance pupil. Here the bottom re-imaged pupil is a reflection of the top as the rays present in the upper image are missing from the lower and vice-versa. Thus, the sum of the upper and lower pupils is a constant, i.e.,  $I_p^+ + I_p^- = cont$ . This is an important point for the particular PS implemented in the UVIC AO lab and will be discussed again later.

At this point, it is not hard to imagine adding sensitivity to both x and y directions by replacing the prism with a four-faceted pyramid. Instead of two re-imaged pupils there would be four, the Foucault graphs for the x direction are simply the sum of the re-imaged pupils in the y direction and vice versa for the y Foucault graphs. However, a difficulty that presents itself even in these highly schematic diagrams is that the signals landing on the detector are quite non-linear, i.e., all of the light is in one of the re-imaged pupils while the other is dark. This is a property of the knife-edge test: it reveals readily the sign of the slope of the wavefront, but not its magnitude. This leads to the concept of modulation which will be discussed in section 2.3.1.

## 2.3 Diffraction Theory of the Knife-Edge Test

The diffraction theory of the knife-edge test dates back to a paper written by Lord Rayleigh (Rayleigh, 1917). In this paper, Rayleigh derives the intensity profile across the re-imaged pupil for the cases of no aberration, a phase step centered on the optical axis and a tilt over half the beam. In the absence of any aberration Rayleigh finds that the intensity profile across the re-imaged pupil is sharply peaked at the edges. This phenomena was named after him and it is now called the Rayleigh ring. Figure 2.6 shows three images of this phenomena captured with the CCD camera of



Figure 2.6: **Rayleigh Ring Observed with the 1d PS:** These images captured with the DALSA CCD of the 1d PS in the UVIC AO lab show the bright Rayleigh ring appearing around the re-imaged pupil. It is hard to make out, but the prism has been moved between the images. In the centre image the prism is centered and the intensity of the Rayleigh ring on either side of the re-imaged pupil is equal. On the left and right hand side the prism is off-centre. On the right side the bottom of the ring is brighter and on the left the top is brighter. This provides a very sensitive method to centre the prism in the focal spot.

the 1d PS. Rayleigh's work was clarified and extended by a series of papers published in the mid 20th century (Gascoigne, 1944; Linfoot, 1946; Linfoot, 1948b; Linfoot, 1948a). This work, and in particular Linfoot's, serves as the basis for the pyramid sensor models which follow.

The most striking and readily derived result is an analytic function describing the illumination of the re-imaged pupil in the absence of an aberration. Using Linfoot's notation, it is given by

$$I = \begin{cases} \pi^2 + \ln^2 \left| \frac{1+X}{1-X} \right| & , |X| < 1 \\ \ln^2 \left| \frac{1+X}{1-X} \right| & , |X| > 1 \end{cases} \quad (2.16)$$

where  $X$  is the normalized coordinate (-1 and 1 at either edge) across a chord of the re-imaged pupil. The result is derived assuming a monochromatic input beam. Figure 2.7 shows a 1d vertical cross section of the middle of the centre image of figure 2.6. Equation 2.16 has been plotted without fitting after being appropriately scaled to the size of the re-imaged pupil on the DALSA CCD. It is evident in the plot that the Rayleigh ring consumes the entire dynamic range of the DALSA CCD. The Rayleigh ring is not limited to the knife-edge test, but occurs in the PS as well.

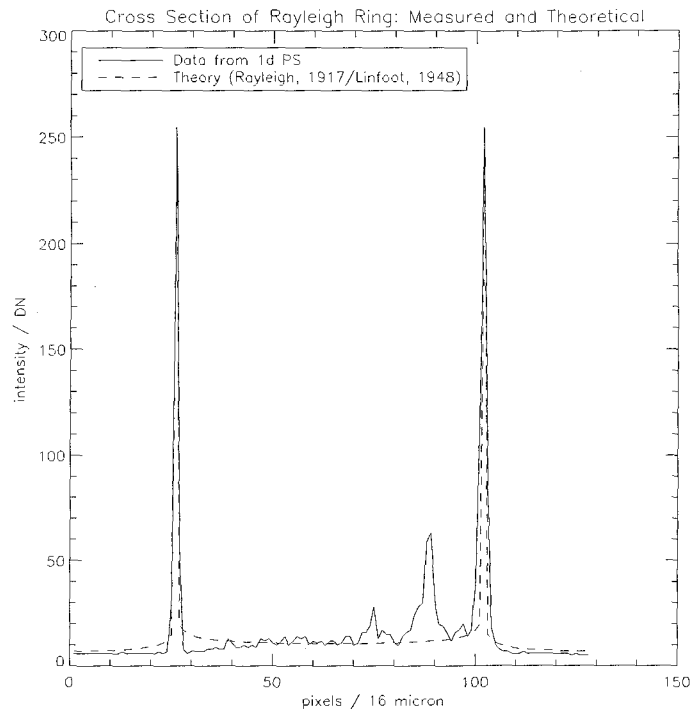


Figure 2.7: **Cross Section of the Rayleigh Ring:** The plot shows the intensity profile of the Rayleigh ring plotted with equation 2.16 scaled appropriately for the size of the re-imaged pupil on the DALSA CCD.

It is a general feature of the Fourier transform of the Heaviside step function. It can be seen around the outer edges of the four re-imaged pupils in PS simulations shown in figures 2.17 and 2.19.

The Rayleigh ring is an important phenomenon for working with the PS because it gives the observer information useful in the alignment process. The brightness of the ring changes as the prism moves around in the focal point at its apex. The prism can be centred by moving it such that the Rayleigh ring's intensity is equal on either side. In addition to this, the Rayleigh ring aides in aligning the rest of the optical system because unless there is a diffraction-limited image formed on the apex of the prism the Rayleigh ring will not appear.

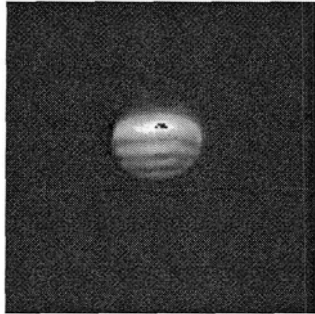


Figure 2.8: Observed Bright and Dark regions of the re-imaged pupil.

Another feature that was pointed out and explained early in the development of the diffraction theory of the knife-edge test is the brightening and darkening of the re-imaged pupil as the knife edge is moved through the focus (Banerji, 1918). An image of this phenomenon captured with the 1d PS is shown in figure 2.8. These bands appear to roll across the image as the prism is moved through focus.

It should also be pointed out that for a real AO system employing a PS, the secondary mirror will generate a secondary Rayleigh ring around its shadow in the re-imaged pupil. This illumination pattern also has an analytic form (Linfoot, 1946). The same is true for a telescope employing a Cassegrain focus, like Gemini/Altair. This effect is also present in segmented mirrors, and this could have implications for ELT's. Figure 2.9 shows the results of a simulation of the PS's response to an aberration free wavefront for a pupil consisting of square segments. The plot on the right hand side of the figure shows the illumination profile across the upper left re-imaged pupil. The discontinuous effects of the segments are clear. However, the effect of the segment gaps is greatly diminished if the size of the gap is less than a pixel in the re-imaged pupil. This feature is also being exploited to use a PS to co-phase the segmented primary of an ELT (Vérinaud and Esposito, 2002; Esposito and Devaney, 2002; Esposito et al., 2003).

The next important result from the diffraction theory of the knife-edge test is again due to Linfoot. The relationship between the electric field in re-imaged pupils ex-

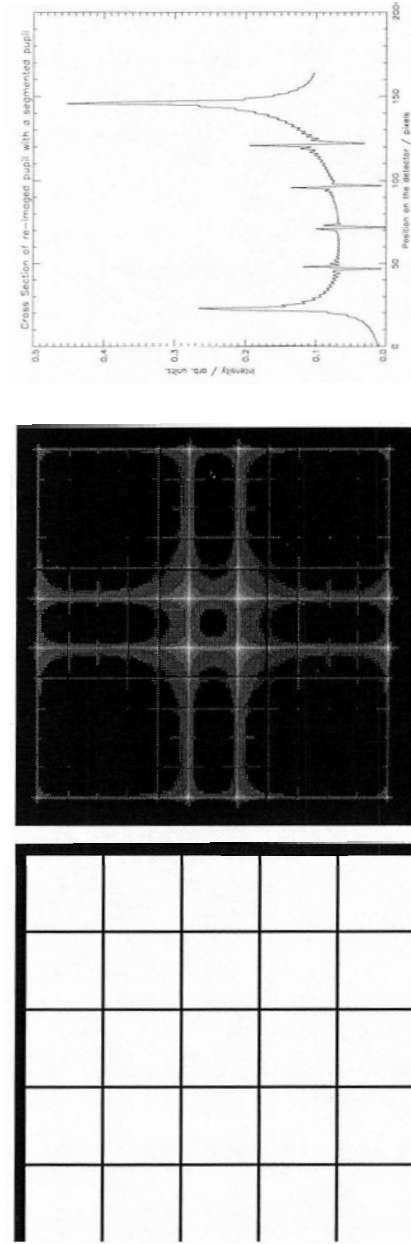


Figure 2.9: **Appearance of Re-imaged Pupils for a Segmented Aperture:** The left hand images shows the square aperture consisting of square segments that was used for the simulation. The centre image shows the appearance of the re-imaged pupils on the PS CCD. The re-imaged pupils are separated by 1.28 their width, from centre to centre. Each quadrant of the CCD contains one re-imaged pupil corresponding to the entire square-segmented pupil on the left. The right hand image shows a cross section of the upper left re-imaged pupil. The discontinuities in the intensity profile at the segment edges are clearly visible.

pressed for an arbitrary electric field in the entrance pupil is given by

$$U_p^\pm(x, y) = \frac{1}{2}E(x, y) \mp \frac{i}{2\pi} \int_{-\infty}^{\infty} \frac{E(t, y)}{t - x} dx \quad (2.17)$$

where the  $\pm$  and  $\mp$  take care of the image inversion that occurs in the re-imaging lens system. The equation has been written using the notation of V erinaud, 2004. The result is easily calculated from the Fourier transform of the Heaviside step function:

$$\mathcal{F}[H(x)](k) = \frac{1}{2}\delta(k) + \frac{p.v.}{2\pi k} \quad (2.18)$$

where  $\delta$  is the Dirac delta distribution and *p.v.* indicates that the Cauchy Principle Value must be taken (Weisstein, 2005). Writing the second term of equation 2.18 as a convolution the equation becomes

$$U_p^\pm(x, y) = \frac{1}{2}E(x, y) \mp \frac{i}{2\pi} E(x, y) \otimes \frac{1}{x} \quad (2.19)$$

and using the property of distributions that  $f(x) \otimes \frac{1}{x} = f'(x) \otimes \ln|x|$  (Conan, 2004)

$$U_p^\pm(x, y) = \frac{1}{2}E(x, y) \mp \frac{i}{2\pi} E'(x, y) \otimes \ln|x|. \quad (2.20)$$

If the usual approximation is made, i.e. that the phase aberrations are small, then the electric field phasor becomes

$$\begin{aligned} E(x, y) &= A \exp(i\phi(x, y)) \\ &\approx A(1 + i\phi(x, y)) \\ E'(x, y) &= iA\phi'(x, y) \end{aligned} \quad (2.21)$$

and substituting this into equation 2.20 gives

$$U_p^\pm(x, y) = \frac{1}{2}E(x, y) \pm \frac{1}{2\pi} \phi'(x, y) \otimes \ln|x| \quad (2.22)$$

where  $A = 1$  has been used for convenience. The convolution product in this equation spreading of the PS signals perpendicular to the direction of the knife edge, an effect which has been commented on and observed in simulations (V erinaud et al., 2003;

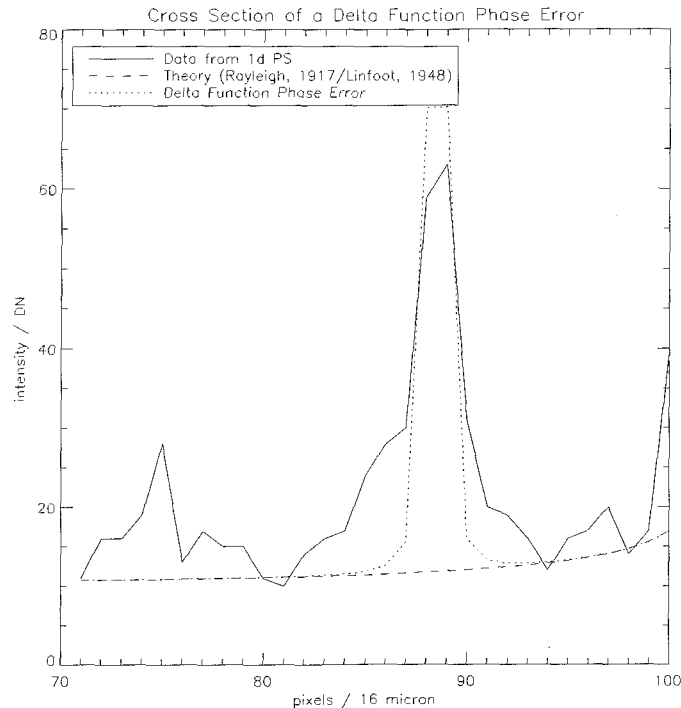


Figure 2.10: **Delta Function Phase Error:** This plot shows the intensity profile through a dust spot visible in the re-imaged pupil in figure 2.6. The dotted curve is equation 2.22 evaluated for a delta function phase error scaled appropriately for the size of the re-imaged pupil on the DALSA CCD. It has been scaled vertically to fit on the plot because of the strong divergence of the function  $\frac{\ln^2|x|}{x^2}$ .

Vérinaud, 2004). Furthermore, if the phase error is a  $\delta$ -function then the convolution can be carried out using the fact that  $\delta'(x) = -\frac{\delta(x)}{x}$  and, using the properties of convolution products, the profile on the CCD should be described by  $\frac{\ln^2|x|}{x^2}$ . There is a dust spot observed in the re-imaged pupil in figure 2.6 and its profile is visible in figure 2.7. In figure 2.10 the function  $\frac{\ln^2|x|}{x^2}$  is shown plotted with the data and equation 2.16. No fitting is performed: the curve is scaled to the size of the re-imaged pupil on the CCD camera. This profile diverges at its centre even more quickly than the Rayleigh ring due to the factor of  $x^2$  in the denominator. It has been scaled to fit on the plot.

All of this being said, equation 2.17 serves as the basis for much of the modeling of the PS, as it allows the PS signals to be calculated by computing

$$S(x, y) = \frac{|U_p^+(x, y)|^2 - |U_p^-(x, y)|^2}{A^2}. \quad (2.23)$$

Equation 2.23 defines the PS signals which leads to the calculation of the signals in the Fourier domain. The reader is referred to V erinaud, 2004 for an excellent description of how this is accomplished both with and without modulation, as well as the retrieval of the phase from  $S$  (calculation of the reconstructor operator). Here the results of the signal calculation in the Fourier domain will be discussed.

The calculation of the signal of the PS (really the knife-edge test) in the Fourier domain is only tractable analytically for an infinite aperture. That is to say that the limits of integration on the integral in equation 2.17 really are  $-\infty$  to  $\infty$  and the integral is not done across a chord of the re-imaged pupil. Under this approximation the signal is given by

$$S = \begin{cases} -i \operatorname{sgn}(f) & , |f| > \frac{\alpha}{\lambda} \\ -\frac{i\lambda}{\alpha} f & , |f| < \frac{\alpha}{\lambda} \end{cases} \quad (2.24)$$

where  $u$  is the spatial frequency and  $\alpha$  is the tip/tilt modulation angle (V erinaud, 2004). This is a beautiful result as it directly shows the two behaviours of the PS. The regime where  $|f| < \frac{\alpha}{\lambda}$  corresponds to modulation at angle  $\alpha$  and the fact that the signal is proportional to  $f$  directly associates it with the phase slope because  $\mathcal{F}[\phi'](f) \propto f \mathcal{F}[\phi](f)$  (see section 2.5 and equation 2.56). Above the spatial frequency associated with the modulation the signal is related to the  $\operatorname{sgn}$  function which is given by

$$\operatorname{sgn}(x) = \begin{cases} 1 & , \text{ for } x > 0 \\ 0 & , \text{ for } x = 0 \\ -1 & , \text{ for } x < 0. \end{cases} \quad (2.25)$$

Equation 2.24 describes the behaviour of the knife-edge test. However, despite the fact that this equation has been derived using diffraction theory, it lacks diffraction effects because the approximation of an infinite aperture is equivalent to assuming  $\lambda \rightarrow 0$  which returns us to the geometrical limit. Rewriting equation 2.17 including

the pupil function,  $P(x, y)$ , which defines the telescope aperture gives

$$U_p^\pm(x, y) = \frac{1}{2}P(x, y)E(x, y) \mp \frac{i}{2\pi}P(x, y)E(x, y) \otimes \frac{1}{x}. \quad (2.26)$$

The integrals involved in equation 2.26, which account for the PSF shape, are not easily solved and perhaps these effects are better studied by a simulation.

Up until this point the discussion has really been about the knife-edge test; the only feature of the PS that has been mentioned is modulation which defines the two regimes of the PS signals in equation 2.24. The first thing that can be done to model the PS is to make it two dimensional, i.e. capable of measuring both the  $x$  and  $y$  components of the phase gradient simultaneously. This is the approach taken in the first implementation in CAOS referred to as the ‘transmission mask’ method (Carbillet et al., 2005). It can also be studied analytically. The process is exactly the same as that that leads to equation 2.17. A Fourier transform relates the input electric field phasor in the pupil plane to the image plane where it is masked by the function representing the pyramid, and a second Fourier transform is performed on the product to return to the pupil plane. In this case the transmission masks for the 2d PS are

$$\begin{aligned} T_1(\tilde{x}, \tilde{y}) &= H(\tilde{x})H(\tilde{y}) \\ T_2(\tilde{x}, \tilde{y}) &= T_1(-\tilde{x}, \tilde{y}) \\ T_3(\tilde{x}, \tilde{y}) &= T_1(-\tilde{x}, -\tilde{y}) \\ T_4(\tilde{x}, \tilde{y}) &= T_1(\tilde{x}, -\tilde{y}) \end{aligned} \quad (2.27)$$

where  $H(\tilde{x})$  is the Heaviside step function. The Fourier transform of  $T_1(\tilde{x}, \tilde{y})$  (see equation 2.18) is given by

$$\mathcal{F}[T_1(\tilde{x}, \tilde{y})] = \frac{1}{4} \left[ \delta(x)\delta(y) + i\delta(x)\frac{p.v.}{\pi y} + i\delta(y)\frac{p.v.}{\pi x} - \frac{p.v.}{\pi^2 xy} \right] \quad (2.28)$$

where  $p.v.$  indicates that the Cauchy Principle Value must be used. The Fourier transforms of the other three transmission masks can be found by the Similarity

theorem, i.e.  $\mathcal{F}[g(ax)](f) = \frac{1}{a}\mathcal{F}[g(x)](f/a)$  where  $a \in \Re$ ,

$$\begin{aligned}\mathcal{F}[T_2(\tilde{x}, \tilde{y})] &= \mathcal{F}[T_1](-x, y) \\ \mathcal{F}[T_3(\tilde{x}, \tilde{y})] &= \mathcal{F}[T_1](-x, -y) \\ \mathcal{F}[T_4(\tilde{x}, \tilde{y})] &= \mathcal{F}[T_1](x, -y)\end{aligned}\tag{2.29}$$

and the electric field in the re-imaged pupils is then given by assuming an infinite aperture

$$\begin{aligned}U_p^{++} &= E(x, y) \otimes \mathcal{F}[T_1](x, y) \\ U_p^{-+} &= E(x, y) \otimes \mathcal{F}[T_2](x, y) \\ U_p^{--} &= E(x, y) \otimes \mathcal{F}[T_3](x, y) \\ U_p^{+-} &= E(x, y) \otimes \mathcal{F}[T_4](x, y).\end{aligned}\tag{2.30}$$

The effects of a finite aperture can be included by inserting a factor of  $P(x, y)$  in equation 2.30 as was done to obtain equation 2.26. The 2d PS signals are defined by

$$\begin{aligned}S_x(x, y) &= \frac{(U_p^{++} + U_p^{-+}) - (U_p^{--} + U_p^{+-})}{A^2} \\ S_y(x, y) &= \frac{(U_p^{++} + U_p^{+-}) - (U_p^{--} + U_p^{-+})}{A^2}.\end{aligned}\tag{2.31}$$

Carrying out the signal calculation reveals that this configuration is entirely equivalent to two knife-edge tests carried out at  $90^\circ$  to one another. This means that all of the results of V erinaud, 2004 apply to this situation as well, with the exception that the shape of the modulation path (the trajectory of the focus relative to the pyramid apex for tip/tilt modulation) now plays a role. This being said, it is beneficial that the results extend to 2d, particularly the signals, as these are important inputs into the calculation of the noise propagation of the sensor, which leads to an assessment of the sensitivity and magnitude gain.

Another approach to modeling the pyramid which is used in CAOS is called the ‘phase mask method’. The analytic theory of this method has been studied by R. Conan (Conan, 2004). A powerful notational formalism has been developed to express the PS equations, which has allowed the computation of the rather complex expressions that

give the Fourier transform of the phase mask and the resulting intensity in the re-imaged pupils. No attempt will be made to describe this work here, other than to reconcile the details of the representation of the phase mask used by CAOS and that used by R. Conan. This is the subject of section 2.3.3. The result of the signal calculation, in the infinite aperture limit, remains the same as the 2d model above and the 1d model of C. Vérinaud. This result and that of the error propagation have been used to estimate the magnitude gain, which is discussed in section 2.3.2.

### 2.3.1 A Discussion of Modulation

In the original presentation of the PS, the signals were linearized by movement of the actual prism (Ragazzoni, 1996). In the geometrical interpretation, the gradient of the wavefront,  $W$ , is simply related to the position,  $x$ , of a ray in the in the focal plane by

$$\frac{x}{f} = \frac{\partial W}{\partial u} \quad (2.32)$$

where  $f$  is the focal length. Hence, the centroid of the PSF is proportional to the average wavefront slope. If the largest wavefront error in the incoming beam causes a deflection of the associated ray of  $x_{max}$  then the pyramid must be moved at least this far in order to have this ray pass through the opposite facet. If the pyramid is oscillated between  $-x_{max}$  and  $x_{max}$  at a rate that is fast compared to the time scale of the turbulence, then the intensity becomes proportional to the wavefront gradient. The signal no longer simply gives the sign of the wavefront gradient, but is proportional to its magnitude. This is the basis of the modulation technique, and it is accomplished in 2d by moving the pyramid on a circular (sinusoidal) or square (ramp) path (Ragazzoni, 1996). This is how the PS is implemented at the Italian Telescopio Nazionale Galileo (TNG) (Ragazzoni et al., 2000b; Ghedina et al., 2003).

A tip-tilt mirror has also been proposed to provide modulation for the PS (Riccardi et al., 1998). In this case a tip-tilt mirror is used to steer the beam on a circular path over the four facets of the pyramid. It is placed in a plane conjugate to the pupil and the PS detector to ensure that the re-imaged pupils do not move on the CCD. Since

the angles involved are small, this method can be considered equivalent to the first one.

As both of the previous modulation methods require moving parts and hence add complexity to the WFS and AO system, a static method would be preferable. Such a ‘static’ modulation was proposed by Ragazzoni et al., 2002. Here several methods were outlined for an optical element that could be used to provide modulation. These include a glass plate which is rough at spatial frequencies greater than the DM cut-off, an array of negative micro-lenses, a 2d diffraction grating, and a holographic diffuser. A holographic diffuser is a novel optical element which changes the impulse response of the system, convolving the PSF with another well defined function. This is the method implemented in the PS for the UVIC AO lab.

Finally it has been suggested that the turbulence itself may provide modulation (Costa et al., 2003b). This is an interesting idea because it removes the necessity for modulation entirely and thereby simplifies the optical design and layout of the PS, particularly for multi-reference applications like MAD. The authors make the point that there are always residual phase errors reaching the WFS while the loop is running because the AO system cannot correct the wavefront perfectly. Thus, the residual aberrations from the turbulence may serve to modulate the beam by blurring the image on the apex of the pyramid in a similar manner to a diffuser.

To test this hypothesis the authors performed simulations in the same manner as those described in section 2.3.3. Wavefronts are generated based on the RMS of the coefficients of the Zernike expansion of the turbulent wavefront according to the results of Noll, 1976.<sup>1</sup> Four simulations were done and in all cases the coefficient of focus,  $Z_4$ , was measured by the PS for increasing values of the input focus error. The four different simulations correspond to four different input wavefronts. Table 2.2 summarizes the simulations. Simulation (a) is equivalent to measuring focus with no modulation. Simulation (b) represents measuring focus in the presence of residual wavefront error on the corrected modes of the AO system. Simulations (c) and (d) represent making the measurement in the presence of both residual aberration on

---

<sup>1</sup>These results are used extensively in the analysis described in section 4.4.1.

Table 2.2: Description of Simulations in Buechler Costa et al., 2003.

Simulation	Wavefront added to varying focus term
(a)	pure focus
(b)	$\frac{1}{10}$ of the Noll RMS: $Z_4$ to $Z_{36}$
(c)	$\frac{1}{10}$ of the Noll RMS: $Z_4$ to $Z_{28}$ full Noll RMS for $Z_{28}$ to $Z_{36}$
(d)	$\frac{1}{10}$ of the Noll RMS: $Z_4$ to $Z_{36}$ full Noll RMS for $Z_{36}$ to $Z_{45}$

the corrected modes and full atmospheric perturbations on the uncorrected modes. Simulation (d) has a larger number of corrected modes than simulation c. The dynamic range of the linear portion of the measurement of the focus error increases from one simulation to the next with d exhibiting the largest linear regime. While this simulation does not quite capture the dynamic nature of the modulation effect provided by the turbulent atmosphere, it does suggest the desired behaviour.

The authors address this issue with an on-sky test at TNG, and find that without modulation the PS in AdOpt performs marginally better than with modulation for the bright guide stars chosen. The authors point out that the correction on the apex of the pyramid is still far from the diffraction limit and hence diffraction effects are still not playing a large role. If this is indeed the case, then turning the modulation off is equivalent to reducing it, not eliminating it. The SNR for a given aberration increases as the modulation is decreased and hence the AO system could simply be performing better because of this. In any case, this paper is important in its implications for simplifying the design of the PS.

### 2.3.2 Expectation of a Magnitude Gain

The PS has received a lot of attention in the AO community because it is expected to show a gain in limiting magnitude over the SH WFS which is currently used in many state of the art facilities including ESO's NAOS/CONICA and Gemini's Altair. A magnitude gain refers to an increase in the magnitude of the guide star used by

the WFS to make wavefront gradient measurements. One of the main drawbacks of classical AO systems is their inherently low sky coverage (and hence limited available astronomical targets) due to a lack of suitably bright guide stars to effectively operate the AO system (Ellerbroek and Tyler, 1998). If the sky coverage of existing systems can be significantly increased simply by switching to a different WFS this is well worth the research and development effort. The magnitude gain of the PS has been studied by many authors and this section will give a summary of the results and the analyses done in the course of this thesis project.

### Ragazzoni and Farinato, 1999

The first paper on the magnitude gain is that of Ragazzoni and Farinato, 1999. In this work the authors argue that the response to tilt of the PS suggests that its noise propagation properties are similar to those of a SH WFS but scaled by a factor which is inversely proportional to the radial order of the Zernike mode in question. That is to say that compared to a SH WFS, the noise propagation coefficient for the PS is attenuated at low radial orders, (tip, tilt, focus, etc) and approaches the SH WFS value at highest radial order corrected.

The magnitude gain is calculated using the equation

$$\Delta m = -2.5 \log \left( \frac{\sigma_{PS}^2}{\sigma_{SH}^2} \right) \quad (2.33)$$

where the  $\sigma_{SH}$  and  $\sigma_{PS}$  are the noise variance of each sensor (i.e., the contribution of the sensor noise to the variance of the corrected wavefront) (Ragazzoni and Farinato, 1999). This is the same variance as in equation 2.5. The noise variances are calculated based on the results of noise propagation on the Zernike modes for the SH WFS (Rigaut and Gendron, 1992). The effect of the PS is added in *ad hoc* as described above.

Figure 2.11 shows the results of this calculation. It has been reproduced using the equations given in the original work. The magnitude gain here approaches 3 magnitudes for large apertures.

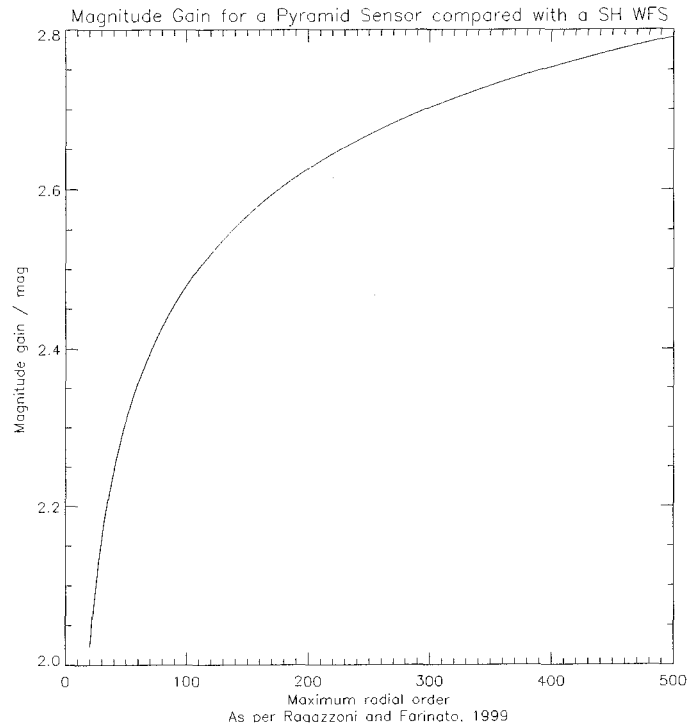


Figure 2.11: **Magnitude Gain, Ragazzoni and Farinato, 1999:** This plot shows the magnitude gain calculated using the method of Ragazzoni and Farinato, 1999. The x-axis is maximum radial order and is taken to be  $\frac{D}{r_0}$ . Thus,  $\frac{D}{r_0} = 500$  represents a telescope of diameter 100 m with  $r_0 = 20\text{cm}$  in the visible and  $\frac{D}{r_0} = 20$  represents a 4 m telescope. The magnitude gain is 2.8 magnitude for the 100 m case and 2.0 magnitudes for the 4 m case.

These results were expanded upon by simulations of the Multiple Mirror Telescope (MMT) AO system using a PS (Esposito et al., 2000b; Esposito and Riccardi, 2001). The authors here note that the magnitude gain of 3 is realized only in the limit of no tilt modulation and no residual wavefront variance, i.e., a diffraction limited image is formed on the apex of the pyramid. Furthermore, for the no modulation case, the gain is drastically reduced or non-existent if the variance of the corrected wavefront exceeds  $1.5 \text{ rad}^2$ . When the wavefront is partially corrected, in the case of the MMT simulations it has a wavefront variance between 2 and  $5 \text{ rad}^2$ , modulation allows a 1.5 to 2.0 magnitude gain to be achieved.

### C. Vérinaud, 2004

The next important calculation of the magnitude gain of the PS accompanies the 1d analytic model of the PS based on the diffraction theory of Linfoot (Vérinaud, 2004). The magnitude gain calculation has also been reproduced from the equations given in the author's paper. The results are shown in figure 2.12.

The model includes the effect of modulation and exhibits the same trend as the calculations of Esposito and Riccardi, 2001. That is to say that the maximum magnitude gain is realized at zero modulation, and decreases with increasing modulation. The two curves represent apertures of 10 m and 100 m telescopes, with the larger magnitude gains occurring with the larger telescope. The size of the magnitude gain has been reduced compared to previous estimates, the reason being that this model of the pyramid sensor includes the spatial filtering of the subapertures (Vérinaud, 2004).

### R. Conan, 2004

The following section describes the estimation of the magnitude gain within the framework of the two dimensional diffraction-based model of the PS developed by R. Conan. It is calculated using equation 2.33. The variance due to sensor noise is calculated

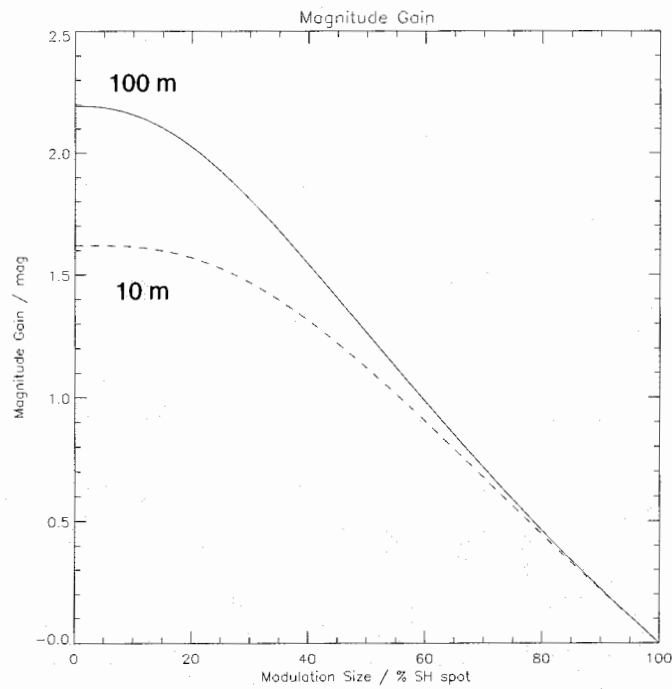


Figure 2.12: **Magnitude Gain, C. Vérinaud, 2004:** Here the magnitude gain is shown plotted against modulation angle expressed in units of the SH WFS spot size. It shows that the two sensors become equivalent when the modulation angle reaches the size of the SH WFS spot. The solid curve corresponds to a 100 m and the dashed curve to a 4 m aperture. The 100 m telescope has a maximum magnitude gain of 2.2 and the 10 m, 1.6 magnitudes.

from the power spectrum of the noise using the following integral

$$\sigma_\phi^2 = \int_{f_0}^{f_c} \int_{f_0}^{f_c} d^2\mathbf{f} \tilde{\mathcal{R}}^2(\mathbf{f}) \sigma_n^2 \quad (2.34)$$

where  $\tilde{\mathcal{R}}$  is the Fourier transform of the reconstructor and  $\sigma_n^2$  is the noise variance of the sensor. The upper limit of the integral is the Nyquist frequency of the DM,  $f_c = \frac{1}{2d}$ . The lower limit represents the lowest spatial frequency which is passed by the telescope,  $f_0 = \frac{1}{D}$ .

The noise variance is constant with spatial frequency (white noise), and therefore the ratio inside the logarithm in equation 2.33 simplifies. Using equation 2.34, equation 2.33 can be re-written

$$\Delta m = -2.5 \log \left( \frac{\sigma_{n-PS}^2}{\sigma_{n-SH}^2} \right) - 2.5 \log \left( \frac{\int_{f_0}^{f_c} \int_{f_0}^{f_c} \tilde{\mathcal{R}}_{PS}^2(\mathbf{f}) d^2\mathbf{f}}{\int_{f_0}^{f_c} \int_{f_0}^{f_c} \tilde{\mathcal{R}}_{SH}^2(\mathbf{f}) d^2\mathbf{f}} \right). \quad (2.35)$$

The first term depends on the noise model for each sensor, and the second depends on the reconstructors alone. If we assume that both sensors have the same characteristics, i.e., signal to noise ratio, subaperture size and read-out noise, the first term reduces to a constant. This constant is not universally agreed upon, but the effect on the magnitude gain is a constant offset. The shape of the magnitude gain as a function of aperture size is determined by the second term.

Figure 2.13 shows the magnitude gain calculated using R. Conan's 2d reconstructors. The curves are similar in shape to those of Ragazzoni and Farinato, 1999. The different curves represent different ratios of  $\sigma_{n-PS}^2$  to  $\sigma_{n-SH}^2$ . The top curve shows the magnitude gain for the variances from V erinaud, 2004. The magnitude gain is 3 for a 100 m primary and 2.4 for a 10 m telescope. The difference is due to the fact that the 1d results were extended to 2d assuming azimuthal symmetry of the reconstructor, which is not actually the case. The true 2d reconstructor has a four fold symmetry (reflection about the Cartesian axes). The noise expression given by R. Conan leads to a very small magnitude gain of 0.3 for a 100 m telescope. Taking the ratio of the two noise variances to be one gives the dashed curve and a magnitude gain of 0.6 at 100 m. Including the reduction in signal due to light scattered by

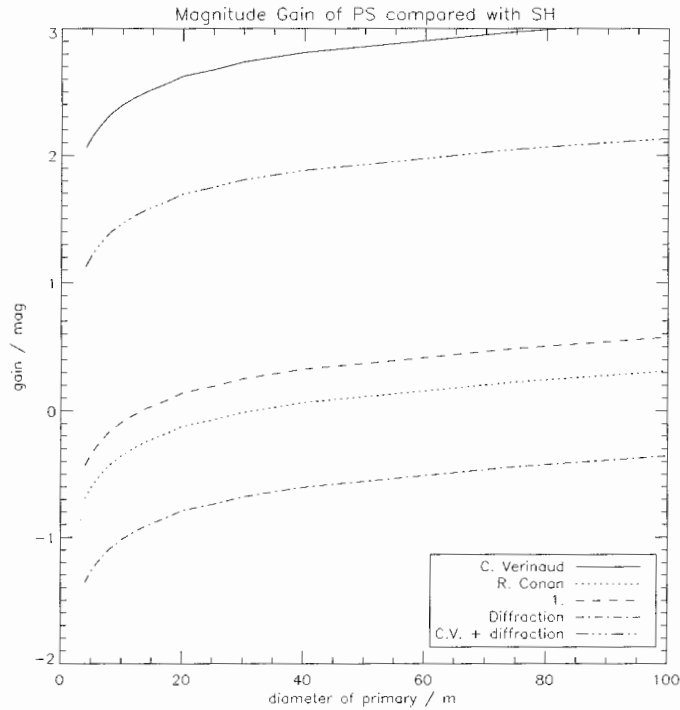


Figure 2.13: **Magnitude Gain, Calculated using R. Conan 2d Model:** These curves show the magnitude gain plotted for different values of the ratio of the PS to SH WFS noise variance. The curves all have the same shape, the effect of the ratio is a constant offset. The solid curve shows the result of using the noise expression given in Vérinaud, 2004. The dotted curve shows the result using the noise expressions of R. Conan (Conan, 2004). The dashed curve is calculated for a ratio of one, meaning that the first term in equation 2.35 is zero. The dash-dotted curve shows the result maintaining the ratio at one, but including the effect of the light scattered by diffraction for the PS, which is discussed in section 2.3.3. The dash-triple dot curve shows this effect added into the calculation using the equations of Vérinaud, 2004. Effectively the light scattered by diffraction reduces the magnitude gain by 1 magnitude.

diffraction (see section 2.3.3) makes the magnitude gain negative at 100 m, while adding it to the results of V erinaud, 2004 gives a magnitude gain of 2.1 at 100 m and 1.4 at 10 m.

Figure 2.14 shows the functional form of the reconstructor for the SH WFS and the PS. The original intuition of Ragazzoni and Farinato, 1999 is partially confirmed by this plot. The PS has suppressed noise propagation at low spatial frequency. The 2d model for the SH reconstructor diverges at zero spatial frequency. This is the reason that the magnitude gain increases with the diameter of the telescope. As  $f_0$  goes to zero, more of this part of the power spectrum is included in the variance. However, the plot also shows that the SH reconstructor propagates less noise than the PS at higher spatial frequency. This is the reason for the steep slope of the curve in figure 2.13 at small aperture size.

The magnitude gain of the PS remains uncertain. It is dependent on both the noise model of the sensor and the reconstructor. The 2d reconstructors calculated by R. Conan are rigorous theoretical results, and are valid in the regime (infinite telescope, for small aberrations with no modulation) where the largest magnitude gain is expected. The SH reconstructor could be improved upon at the low spatial frequency limit to avoid the singularity, but this would serve to reduce the magnitude gain. There is much greater uncertainty in the expressions for the noise variance of the sensor and effort is better spent on calculating these than in reformulating reconstructors. This is the topic of section 2.4.

### 2.3.3 Unification of R. Conan's Work with CAOS techniques

CAOS is a complete system for modeling AO systems (Carbillet et al., 2001; Carbillet et al., 2005). It is divided into modules, one of which is the PS and the scientific code for this module has largely been developed by C. V erinaud. The numerical code performs exactly the same tasks as are carried out in the analytic derivations, i.e., the re-imaged pupils on the detector are calculated from the Fourier transform of the masked Fourier transform of the input electric field phasor. The only improvement

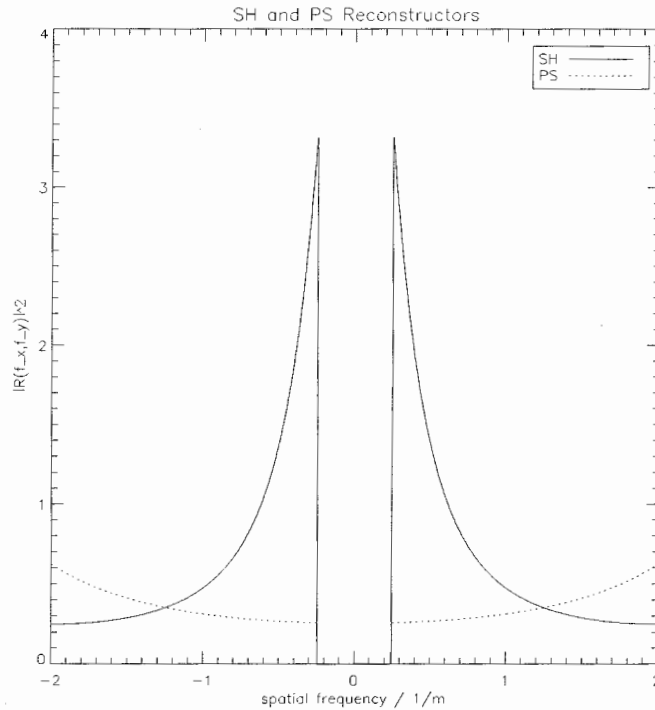


Figure 2.14: **Functional Form of the Reconstructors:** This plot shows the profile of the Fourier transform of the reconstructors for both the SH WFS and the PS. The PS clearly has suppressed noise propagation at low spatial frequency. In fact the SH WFS reconstructor becomes unbounded at zero spatial frequency in the analytic model. This underlies the observation that the magnitude gain increases with aperture size. As the aperture size increases, more of region near the origin is included in the integral in the second term of equation 2.35 meaning that the SH term in the denominator becomes larger and the term increases.

that has been added to the CAOS PYR module is to replace the IDL FFT's with the `mathft.pro` routine from PAOLA which computes the Fourier transforms according to the mathematical definition. In this way the intensity in the image plane and the detector plane is conserved. The following derivation shows that the mask used in the CAOS 'phase mask' method and the mask used by R. Conan in developing the 2d diffraction theory of the PS are in fact the same function.

The transmittance function used by CAOS is written

$$T(\tilde{\mathbf{x}}) = \exp(im(\tilde{\mathbf{x}})) \quad (2.36)$$

with the focal plane mask function,  $m(\tilde{\mathbf{x}})$ , given by

$$m(\tilde{\mathbf{x}}) = \sum_{j=1}^4 2\pi k T_j(\tilde{\mathbf{x}}) P_j(\tilde{\mathbf{x}}) \quad (2.37)$$

The functions  $T_j(\tilde{\mathbf{x}})$  are products of two Heaviside step functions, isolating each of the four facets of the pyramid as in equation 2.27. The functions  $P_j(\tilde{\mathbf{x}})$  define the planes of the facets with the parameter  $k$  giving the slope and  $P_1(\tilde{x}, \tilde{y}) = \tilde{x} + \tilde{y}$

$$\begin{aligned} T_1(\tilde{x}, \tilde{y}) P_1(\tilde{x}, \tilde{y}) &= H(\tilde{x}) H(\tilde{y}) (\tilde{x} + \tilde{y}) \\ T_2(\tilde{x}, \tilde{y}) P_2(\tilde{x}, \tilde{y}) &= T_1(-\tilde{x}, \tilde{y}) P_1(-\tilde{x}, \tilde{y}) \\ T_3(\tilde{x}, \tilde{y}) P_3(\tilde{x}, \tilde{y}) &= T_1(-\tilde{x}, -\tilde{y}) P_1(-\tilde{x}, -\tilde{y}) \\ T_4(\tilde{x}, \tilde{y}) P_4(\tilde{x}, \tilde{y}) &= T_1(\tilde{x}, -\tilde{y}) P_1(\tilde{x}, -\tilde{y}) \end{aligned} \quad (2.38)$$

The Fourier transform of the transmittance function is needed to calculate the signals measured in the pupil plane by the PS.

$$\begin{aligned} \mathcal{F}\{T(\tilde{\mathbf{x}})\} &= \mathcal{F}\{\exp(im(\tilde{\mathbf{x}}))\} \\ &= \mathcal{F}\{\exp(i2\pi k \sum_{j=1}^4 T_j(\tilde{\mathbf{x}}) P_j(\tilde{\mathbf{x}}))\} \\ &= \mathcal{F}\{\prod_{j=1}^4 \exp(i2\pi k T_j(\tilde{\mathbf{x}}) P_j(\tilde{\mathbf{x}}))\} \end{aligned} \quad (2.39)$$

Making use of the Convolution theorem, we have

$$\begin{aligned} \mathcal{F}\{T(\tilde{x}, \tilde{y})\} &= \mathcal{F}\{\exp(i2\pi kT_4(\tilde{\mathbf{x}})P_4(\tilde{\mathbf{x}}))\} \otimes \mathcal{F}\{\exp(i2\pi kT_3(\tilde{\mathbf{x}})P_3(\tilde{\mathbf{x}}))\} \\ &\otimes \mathcal{F}\{\exp(i2\pi kT_2(\tilde{\mathbf{x}})P_2(\tilde{\mathbf{x}}))\} \otimes \mathcal{F}\{\exp(i2\pi kT_1(\tilde{\mathbf{x}})P_1(\tilde{\mathbf{x}}))\}. \end{aligned} \quad (2.40)$$

Using the definition of the Fourier transform for the  $j = 1$  term the integral is

$$\mathcal{F}\{\exp[i2\pi kT_1(\tilde{\mathbf{x}})P_1(\tilde{\mathbf{x}})]\} = \int_{-\infty}^{\infty} \int_{-\infty}^{\infty} \exp(-2\pi i \mathbf{x} \cdot \tilde{\mathbf{x}}) \exp(i2\pi kH(\tilde{x})H(\tilde{y})(\tilde{x} + \tilde{y})) d^2 \tilde{\mathbf{x}} \quad (2.41)$$

and we proceed by eliminating the Heaviside step functions from the exponent by rewriting the integrals.

$$\begin{aligned} \mathcal{F}\{\exp[i2\pi kT_1(\tilde{\mathbf{x}})P_1(\tilde{\mathbf{x}})]\} &= \int_{-\infty}^{\infty} \int_{-\infty}^0 \exp(-2\pi i \mathbf{x} \cdot \tilde{\mathbf{x}}) d\tilde{x} d\tilde{y} \\ &+ \int_{-\infty}^0 \int_0^{\infty} \exp(-2\pi i \mathbf{x} \cdot \tilde{\mathbf{x}}) d\tilde{x} d\tilde{y} \\ &+ \int_0^{\infty} \int_0^{\infty} \exp(-2\pi i \mathbf{x} \cdot \tilde{\mathbf{x}}) \exp(i2\pi k(\tilde{x} + \tilde{y})) d\tilde{x} d\tilde{y} \\ &= \int_{-\infty}^{\infty} \int_{-\infty}^{\infty} H(-\tilde{x}) \exp(-2\pi i \mathbf{x} \cdot \tilde{\mathbf{x}}) d^2 \tilde{\mathbf{x}} \\ &+ \int_{-\infty}^{\infty} \int_{-\infty}^{\infty} H(\tilde{x})H(-\tilde{y}) \exp(-2\pi i \mathbf{x} \cdot \tilde{\mathbf{x}}) d^2 \tilde{\mathbf{x}} \\ &+ \int_{-\infty}^{\infty} \int_{-\infty}^{\infty} H(\tilde{x})H(\tilde{y}) \exp[i2\pi k(\tilde{x} + \tilde{y})] \exp(-2\pi i \mathbf{x} \cdot \tilde{\mathbf{x}}) d^2 \tilde{\mathbf{x}} \\ &= \mathcal{F}\{H(-\tilde{x})\} \\ &+ \mathcal{F}\{H(\tilde{x})H(-\tilde{y})\} \\ &+ \mathcal{F}\{H(\tilde{x})H(\tilde{y}) \exp(i2\pi k(\tilde{x} + \tilde{y}))\} \end{aligned} \quad (2.42)$$

Using the Similarity theorem and equation 2.38 the Fourier transforms of each of the

terms in the product can be written

$$\begin{aligned}
\mathcal{F}\{exp[i2\pi kT_1(\tilde{\mathbf{x}})P_1(\tilde{\mathbf{x}})]\} &= \mathcal{F}\{H(-\tilde{x}) + H(\tilde{x})H(-\tilde{y}) + T_1(\tilde{\mathbf{x}}) \exp[i2\pi kP_1(\tilde{\mathbf{x}})]\} \\
\mathcal{F}\{exp[i2\pi kT_2(\tilde{\mathbf{x}})P_2(\tilde{\mathbf{x}})]\} &= \mathcal{F}\{H(\tilde{x}) + H(-\tilde{x})H(-\tilde{y}) + T_2(\tilde{\mathbf{x}}) \exp[i2\pi kP_2(\tilde{\mathbf{x}})]\} \\
\mathcal{F}\{exp[i2\pi kT_3(\tilde{\mathbf{x}})P_3(\tilde{\mathbf{x}})]\} &= \mathcal{F}\{H(\tilde{x}) + H(-\tilde{x})H(\tilde{y}) + T_3(\tilde{\mathbf{x}}) \exp[i2\pi kP_3(\tilde{\mathbf{x}})]\} \\
\mathcal{F}\{exp[i2\pi kT_4(\tilde{\mathbf{x}})P_4(\tilde{\mathbf{x}})]\} &= \mathcal{F}\{H(-\tilde{x}) + H(\tilde{x})H(\tilde{y}) + T_4(\tilde{\mathbf{x}}) \exp[i2\pi kP_4(\tilde{\mathbf{x}})]\}
\end{aligned} \tag{2.43}$$

Undoing the convolution in equation 2.40

$$\begin{aligned}
\mathcal{F}\{T(\tilde{\mathbf{x}})\} &= \mathcal{F}\{(H(-\tilde{x}) + H(\tilde{x})H(-\tilde{y}) + T_1(\tilde{\mathbf{x}}) \exp(i2\pi kP_1(\tilde{\mathbf{x}}))) \cdot \\
&\quad (H(\tilde{x}) + H(-\tilde{x})H(-\tilde{y}) + T_2(\tilde{\mathbf{x}}) \exp(i2\pi kP_2(\tilde{\mathbf{x}}))) \cdot \\
&\quad (H(\tilde{x}) + H(-\tilde{x})H(\tilde{y}) + T_3(\tilde{\mathbf{x}}) \exp(i2\pi kP_3(\tilde{\mathbf{x}}))) \cdot \\
&\quad (H(-\tilde{x}) + H(\tilde{x})H(\tilde{y}) + T_4(\tilde{\mathbf{x}}) \exp(i2\pi kP_4(\tilde{\mathbf{x}})))\}
\end{aligned} \tag{2.44}$$

Carrying out the product leaves

$$\mathcal{F}\{T(\tilde{\mathbf{x}})\} = \mathcal{F}\left\{\sum_{j=1}^4 (T_j \exp(i2\pi kP_j(\tilde{\mathbf{x}})))\right\} \tag{2.45}$$

which is the pyramid transmittance function used in R. Conan's calculations.

Despite the fact that in this approach rewriting the integral in equation 2.42 and evaluating the product in equation 2.44 uses only the values of the Heaviside step function (0 or 1) on either side of the origin both equation 2.36, the CAOS transmittance function, and equation 2.45, the sum transmittance function, give 1 when evaluated at (0,0). Hence the CAOS routines and the analytical calculations should give comparable results. The effects of a roof and the pupil separation on the detector have been studied using the modified CAOS routines mentioned above.

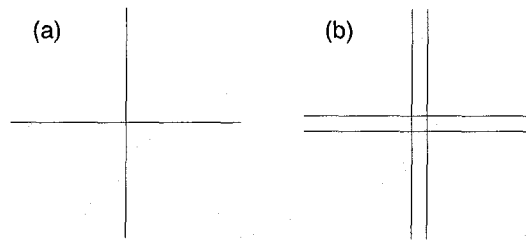
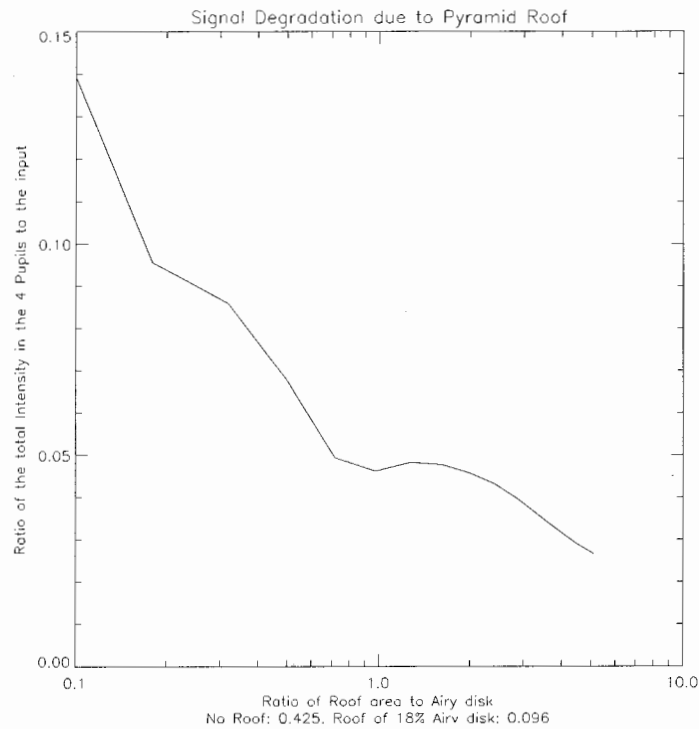


Figure 2.15: **Schematic of the pyramid roof:** A schematic of the pyramid apex with no roof is shown in (a). Part (b) shows the apex with a roof. The square represents the flattened apex corresponding to the roof and the gaps between each of the facets represent turned edges of the same width as the roof.

### Roof Effects

The purpose of the calculation described in this section is to use the CAOS PS routines to elucidate the effects of the roof on the signal. The roof refers to a flat face at the apex of the pyramid and is a consequence of fabrication. This will be discussed in section 4.1. The calculations have been performed with a flat incoming wavefront, meaning that a diffraction limited image is formed on the apex of the pyramid. The pyramid is represented as a phase mask and it is straightforward to modify the perfect apex to one that has a roof. Figure 2.15 shows schematically the apex of the pyramid. Part (a) shows a perfect pyramid with no roof and part (b) shows the configuration with the roof. The square in the centre represents the roof and the gaps between the facets represent turned edges of the same width as the roof. The calculation has the following steps: the image on the apex of the pyramid is calculated via a Fourier transform of the pupil and multiplied by the phase mask (see equation 2.37), the image in the detector plane (the re-imaged pupils) is calculated via another Fourier transform, the irrelevant portion of the image is masked out keeping only the light which lands within the re-imaged pupils (as this region is used to calculate the signals), and the throughput (efficiency) is calculated as the ratio of the incident intensity to that landing inside the pupils on the CCD. This was repeated for roof sizes ranging from 0 to 150% of the area of the Airy disk, i.e.  $\pi \frac{\lambda^2}{D^2}$ .

Figure 2.16 shows the results of the calculation. The signal degradation is quite



**Figure 2.16: Signal Degradation due to Pyramid Roof:** This plot shows the decrease in the amount of intensity in the four re-imaged pupils as a function of increasing roof size. With no roof the ratio between the incoming intensity and the intensity in the re-imaged pupils is 0.425 and with a roof with an area of 18% the area of the Airy disk the ratio drops to 0.096. The number of photons contributing to the useful signal is dramatically impacted by the presence of a roof.

dramatic for even a small roof. With no roof, the throughput is 42.5%. This may seem odd but it is a fundamental property of using this type of WFS and was first pointed out by Zernike in 1934 (Linfoot, 1946). However, even for a small roof of size equal to 18% of the Airy disk the throughput drops by a factor of four to 9.6%. Thus, the roof plays a critical role in determining the signal to noise ratio of the sensor by limiting the number of photons providing useful measurements.

It should be noted that this calculation, despite being in the diffraction limited regime, represents a lower limit on the performance. The maximum magnitude gain is realized when the image on the apex of the pyramid is diffraction limited; however, the amount of light scattered by the pyramid and the roof becomes greatest in this limit. This means that as the image quality approaches the diffraction limit, the sensor propagates less noise (as can be seen from the reconstructor) but at the same time scatters more light. The increase in scattered light increases the effect of photon noise and reduces the SNR. This drop in SNR mediates the noise suppression of the PS and decreases the expected magnitude gain by  $\approx 1$  magnitude for a perfect pyramid.

On the left, figure 2.17 shows the appearance of the image in the detector plane. The scattered light is quite evident. The circle in the centre of the image originates from light that passes through the roof. The other light is scattered by the sharp edges. In this idealized calculation, the roof is perfectly flat, in practice this will not be the case and the appearance of the scattered light is much less obviously structured. The right hand side shows the pupils after the masking has been applied. The mask is one inside the geometrical shadow of the four re-imaged pupils and zero outside. It isolates the relevant part of the image from which the sensor signals are calculated.

### Separation of the Re-imaged Pupils

A similar calculation has been carried out, again using the modified CAOS routines, to examine the effects of the pupil separation on the amount of light in the pupils. Changing the pupil separation is equivalent to changing the apex angle of the prism, as will be discussed in section 4.1. This time the calculation outlined above was done for edge-to-edge separations varying from 0 to 3 times the diameter of the re-

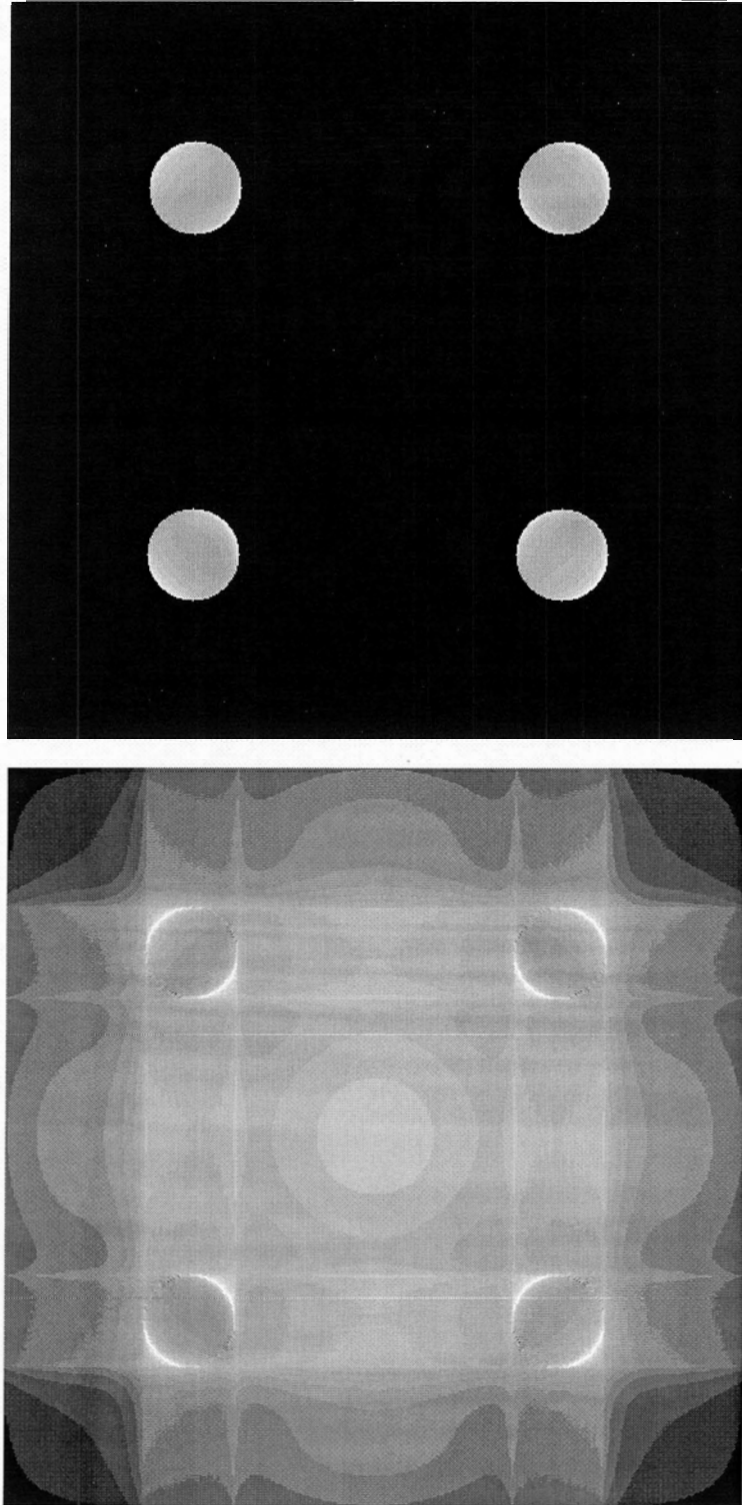


Figure 2.17: **Re-imaged pupils in the presence of a roof:** The left hand image shows the intensity distribution in the detector plane of a PS with a roof. The roof size is 32% of the Airy disk. The right hand image shows the pupils after the mask has been applied. The intensity scale has been compressed by exponentiating to a  $1/8^{th}$  power.

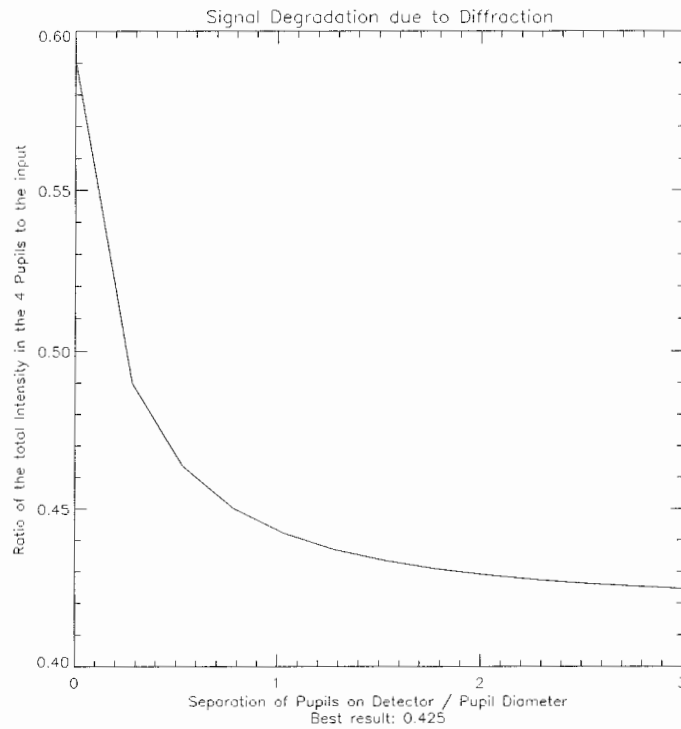


Figure 2.18: **Effect of Pupil Separation:** This plot shows the effect of diffracted light in the PS. If the pupils are too close together on the detector then there will be light scattered by diffraction landing in the re-imaged pupils producing a spurious signal.

imaged pupils. The purpose of this calculation was to examine the effect of scattered light landing inside the re-imaged pupils. The pupil separation primarily affects the position of the re-imaged pupils on the detector, not the distribution of light around the re-imaged. Hence, the effect here is a spurious signal due to excess scattered light landing inside the re-imaged pupils.

Figure 2.18 shows the results of the calculation of the ratio of the total intensity landing in the re-imaged pupil to that of the input beam. The asymptotic value of the this ratio is approximately 42.5% which occurs at 3 times the pupil diameter. This means that to avoid light scattering into the re-imaged pupils they should be placed at the corners of the detector at at least this separation.

This result contradicts what is stated in Riccardi et al., 1998 about data packing and the positions of the pupils on the CCD. They state that the best use of the CCD is to have the edges of the re-imaged pupils touching. This corresponds to an equality in equation 4.2 on page 68. It is true that this condition gives the smallest detector area; however, with the pupils in this position,  $\sim 17\%$  of the light landing in the pupils is scattered light and is contributing spuriously to the signal. It is important to realize again that this effect is worst in the diffraction-limited case, i.e., if the sensor was meant to function far from the diffraction limit it would not be necessary to separate the pupils to such a great extent. Interestingly, the pupils in MAD are separated by 2.14 diameters (Ragazzoni et al., 2001).

Figure 2.19 shows the images information as figure 2.17, but in this case the pyramid does not have a roof, and the re-imaged pupils are separated by 0.53 times their diameter, edge-to-edge. On the left, the image in the detector plane is shown and the scattered light can be seen joining the re-imaged pupils. This intensity continues into the re-imaged pupils and leads to the spurious signal. The right hand image shows the detector plane after the mask has been applied. The mask is the same as the one used for figure 2.17, i.e., it is equal to one inside the geometrical shadow of the re-imaged pupils and zero elsewhere. Light scattered into the area defined by the mask contributes to the spurious signal.

### Reflective Pyramid

CAOS calculations have also been performed for a reflective pyramid. A reflective pyramid works in a similar manner to a refractive pyramid. Each facet of the reflective pyramid isolates and reflects the corresponding portion of the image plane, instead of refracting it. One re-imaged pupil can be formed from the beam reflected from each facet. It has been suggested as an alternative to refractive pyramids because it may be possible to make a very sharp apex, and thereby overcome the limits associated with optical polishing. J. Pazder of HIA has suggested a reflective pyramid could be made out of a cleaved crystal.

In terms of modeling the reflective pyramid using the modified CAOS routines a

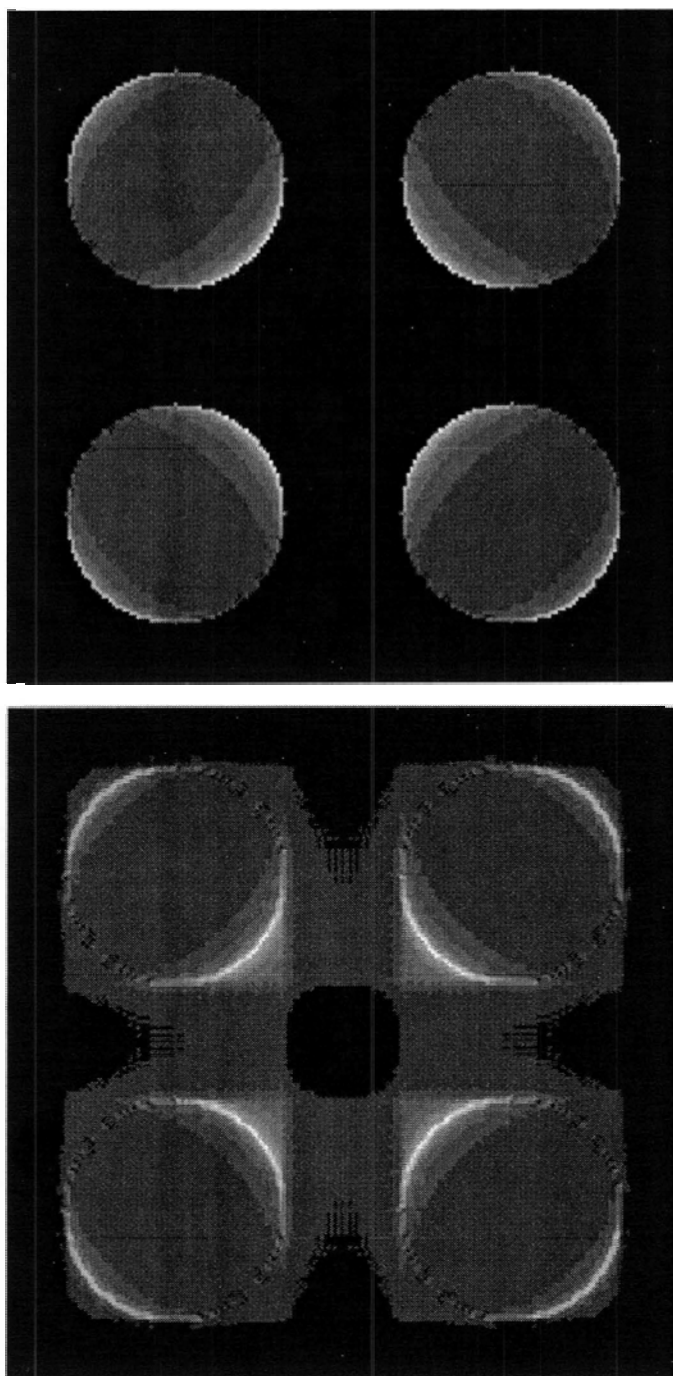


Figure 2.19: **Cross-talk between the Re-imaged Pupils:** This plot shows the same images as figure 2.17 for a PS with no roof. The pupils are separated by 0.53 times their own diameter. The scattered light can be seen joining the pupils together.

new phase mask must be used. The reflective pyramid is the same as the refractive pyramid except that the beams are isolated from each other. Thus, each quadrant of the phase mask used for the refractive pyramid was used individually. In this way the re-imaged pupils could be formed from the isolated beams. The results are similar for this case. The throughput of the diffraction limited case with no roof was 0.423 at a pupil separation of 3 pupil diameters. The reflective pyramid seems to be less sensitive to the presence of the roof as the throughput is 0.18 with a roof size of 18% the area of the Airy disk compared to 9.6% for the previous calculation. However, analytically, using the theory presented above, the two configurations should be the same, and this may indicate that the improvement seen in the behaviour of the reflective pyramid is an artifact of the calculation.

These calculations are relevant to the noise properties of the sensor in the diffraction limited regime. In this case, if we assume widely separated pupils the number of photons contributing to the signal should be reduced by a factor of 0.425. With this taken into account the magnitude gain of the PS is reduced by roughly 1 magnitude.

## 2.4 Signal Variance and Sensor Noise

The noise properties of the SH WFS are described by expressions of the form

$$\sigma_{\phi-SH}^2 = d^2 \left( \frac{2\pi}{\lambda_{corr}} \right)^2 \left( \frac{\theta_B}{SNR} \right)^2 \quad (2.46)$$

where  $d$  is the subaperture size,  $\lambda_{corr}$  is the central wavelength of the corrected band,  $\theta_B$  is the so-called ‘blurring angle’ and SNR is the signal to noise ratio (Fontanella, 1985; Rousset, 1999).

This formula is derived starting with the change in the phase over one subaperture which is given by

$$\frac{\Delta\phi}{d} = \frac{2\pi}{\lambda} \frac{\delta}{F} \quad (2.47)$$

where  $\delta$  is the linear displacement of the SH spot and  $F$  is the focal length of the SH

lenslet (Fontanella, 1985). The ratio  $\frac{d}{F}$  is the slope and the signal of the SH WFS, so generalizing the expression for any gradient sensor gives

$$\frac{\Delta\phi}{d} = \frac{2\pi}{\lambda} S \quad (2.48)$$

where  $S$  is the WFS signal. Thus, the task becomes to calculate the variance of  $\Delta\phi$  in terms of the variance of the signal, namely

$$\sigma_{\Delta\phi}^2 = d^2 \left( \frac{2\pi}{\lambda} \right)^2 \sigma_S^2 \quad (2.49)$$

with the final assumption that  $\sigma_\phi^2 \approx \sigma_{\Delta\phi}^2$ , which is a good approximation for high spatial frequency aberrations because in this limit the phase and its derivative will have similar spatial frequency content.

The signal variance calculation for the SH WFS is straightforward and is outlined carefully in Fontanella, 1985.

The signal variance calculation for the PS is much more involved and the details of the derivation are given in Appendix A. The result is

$$\sigma_S^2 = \frac{6}{SNR^2} \sigma_{\phi_{in}}^2 \quad (2.50)$$

where  $\sigma_{\phi_{in}}^2$  is the variance of the input wavefront. This equation has some interesting properties. It shows that the sensor noise, which is proportional to  $\sigma_S^2$ , decreases when the variance of the input phase decreases. This is the anticipated property of the PS, less noise as the quality of the wavefront improves, i.e. in closed loop.

Substituting  $\sigma_S^2$  back into equation 2.49 gives

$$\sigma_{\phi-PS}^2 = d^2 \left( \frac{2\pi}{\lambda} \right)^2 \left( \frac{6}{SNR^2} \right) \sigma_{\phi_{in}}^2 \quad (2.51)$$

and the  $\Delta$  has been dropped. To get an upper limit on the magnitude gain, the input phase variance of the fitting error can be used as the input phase variance, i.e.,

$\sigma_{fit}^2 = 0.0863(r_0 f_c)^{5/3}$ . This approximation is equivalent to a perfect AO system.

$$\sigma_{\phi-PS}^2 = d^2 \left( \frac{2\pi}{\lambda} \right)^2 \left( \frac{6}{SNR^2} \right) 0.0863 (r_0 f_c)^{-\frac{5}{3}} \quad (2.52)$$

If it is then assumed that the subaperture size is matched to the Fried parameter, the equation reduces to

$$\sigma_{\phi}^2 \approx d^2 \left( \frac{2\pi}{\lambda} \right)^2 \left( \frac{2}{SNR^2} \right). \quad (2.53)$$

Equation 2.53 resembles its counterpart for the SH WFS, equation 2.46; however, it lacks a factor to set the angular scale, i.e., the factor of  $\theta_B^2$ . This is due to the fact that despite the efforts to calculate the signals using diffraction theory the equation is valid in the geometrical limit where the knife-edge test effectively sensitive to infinitesimal phase errors. If modulation is included there will be a factor of  $\alpha^2$  where  $\alpha$  is the modulation angle. Thus, equation 2.53 becomes

$$\sigma_{\phi-PS}^2 = d^2 \left( \frac{2\pi}{\lambda} \right)^2 \left( \frac{\alpha}{SNR} \right)^2 \quad (2.54)$$

and calculating the ratio with equation 2.46

$$\frac{\sigma_{\phi PS}^2}{\sigma_{\phi SH}^2} = \left( \frac{\alpha}{\theta_B} \right)^2. \quad (2.55)$$

In any case, the model is not sophisticated enough to give a rigorous calculation of the signal variance at this stage because of the infinite aperture approximation used in calculating the signals. C. V erinaud's calculation uses the appropriate reconstructors for modulation/no-modulation regimes, but the noise variance used in both regimes is still based on the geometrical signals. Treating the non-linear behaviour of the knife-edge test properly requires including the effects of the finite aperture of the telescope (Malacara, 1978).

## 2.5 An Alternative to the pyramid

An alternative to the PS has been suggested by C. V erinaud and we carried out some initial studies. The pyramid of the PS is nothing more than a spatial filter in the focal plane. A spatial filter modifies the complex amplitude in either the image or the pupil plane to produce some desired effect on the light (Goodman, 1996). It is a central concept in optical processing and Fourier optics. In this case the spatial filter is the pyramid and it is represented by 2d Heaviside functions and the phase masks representing the facets of the prism, as shown in the preceding sections. See equation 2.45. The desired effect is to produce four beams from which the slope of the wavefront can be extracted. There is no fundamental reason why this type of focal plane spatial filter must be used. In fact, there may be practical reasons for choosing a different spatial filter.

The type of wavefront sensor envisioned by V erinaud is called the amplitude modulated PS. The idea here is to exchange the Heaviside function for a piecewise linear function that gradually changes from fully transmissive to zero transmission. The hypothesis is that the gradual change will provide a static modulating effect, the magnitude of which will be inversely proportional to the transition gradient. The name ‘amplitude modulated’ comes from the fact that it is the amplitude of the incoming light that is changed to linearize the sensor, not the phase, as is the case with tip/tilt modulation.

This is not an entirely new concept, and work has been done in the past to study this idea (Sprague and Thompson, 1972; Horwitz, 1978; Horwitz, 1994). The theoretical underpinning of using a gradient filter in the focal plane simply comes from the well known result that differentiation is multiplication in the Fourier domain:

$$\mathcal{F}[f'(x)](k) = 2\pi ik\mathcal{F}[f(x)](k) \quad (2.56)$$

where  $f(x)$  and  $F(k)$  are Fourier transform pairs. The slope of the gradient simply scales the intensity which is equivalent to trading sensitivity for dynamic range. However, the optical methods presented in Sprague and Thompson, 1972 are better

suited to large phase differences (several wavelengths) and it might be possible to adapt these techniques for open loop measurements. It has also been pointed out that because the amplitude is the quantity modified by the filter and intensity is the measured quantity, a square root filter is more appropriate for tailoring a linear response between intensity and slope. This is due to the fact that the intensity is related the square of the amplitude (Horwitz, 1978).

In addition, to these spatial filters more exotic spatial filtering can be used in novel WFS's. A wavefront sensing scheme where a lenslet array like those used to subdivide the pupil plane in the SH WFS can be used to sub-divide the image plane to create a Pyramid-like WFS (Clare and Lane, 2005). This setup also exhibits enhanced performance over the SH WFS.

### 2.5.1 Amplitude Modulated PS: Simulation

A similar simulation to the ones mentioned in the preceding section was used to test this hypothesis. Instead of changing the properties of the sensor, the tilt of the incoming wavefront was varied. This is the same process as was used to calibrate the 1d PS which is the subject of chapter 4.

Figure 2.20 shows the result of the calculation. Tilt is varied along the x-axis and the mean signal (calculated with equation 2.31) is shown on the y-axis. The different curves are for different widths of the transition region which is inversely proportional to the slope, and hence is hypothesized to be proportional to the magnitude of the modulation. The solid line shows the PS with no modulation. The effect is clear: the linear regime for the tilt response becomes wider for an increasing size of the transition region. Changing the transmission function in this way does produce an effect like that of modulation.<sup>2</sup>

---

<sup>2</sup>It has been pointed out by C. V erinaud that for higher order modes it is more appropriate to measure the variance of the signal. This is because for high order Zernike modes the variance of wavefront derivative should increase in proportion to that of the wavefront.

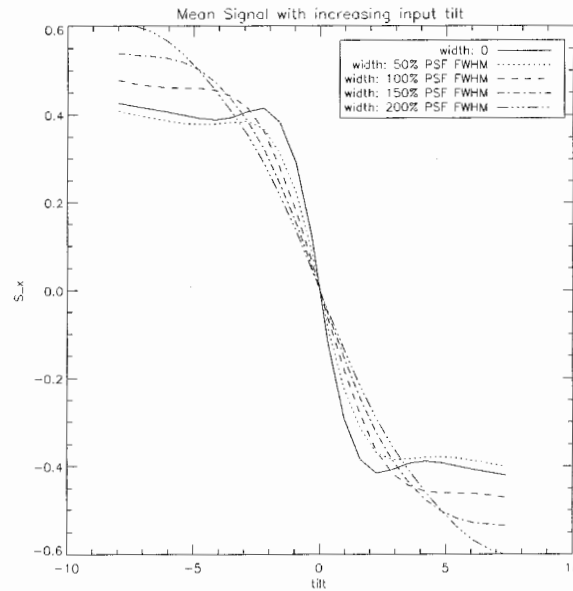


Figure 2.20: **Amplitude Modulated PS Response to Tilt:** This plot shows the amplitude modulated PS's response to varying tilt of the incoming wavefront. The mean signal in the x direction, calculated using equation 2.31, is given as a function of tilt for various widths of the transition region. As the width increase the curves, the slope of the curve decreases, indicating that this arrangement produces a linear sensor with a sensitivity inversely proportional to the width of the transition region.

### 2.5.2 Analytic Signal Equations

The same process as described above in section 2.3 has been applied to the case of the amplitude modulated PS. The illumination in the pupil plane after the transmission mask is given by

$$U_p^\pm(x, y) = E(x, y) \otimes \mathcal{F} [M^\pm(\tilde{x}, \tilde{y})] (x, y) \quad (2.57)$$

where  $M$  is the function defining the transmission mask.  $M$  is defined as

$$M^+(\tilde{x}, \tilde{y}) = \begin{cases} 1 & , \tilde{x} < -w \\ \frac{1}{2} (\sin(\frac{\pi\tilde{x}}{2w}) + 1) & , -w < \tilde{x} < w \\ 0 & , \tilde{x} > w \end{cases} \quad (2.58)$$

where  $w$  is the half width of the transition region. The sine function was chosen for the transition instead of the ramp mentioned above due to the ease with which its Fourier transform can be computed. It is a good approximation to a line on  $[-\pi/2, \pi/2]$ .

Skipping the intervening steps and moving right to the result,  $U_p^\pm(x, y)$  is

$$\begin{aligned} U_p^\pm(x, y) &= \frac{1}{2}E(x, y) \mp \frac{i}{2\pi}E(x, y) \otimes \frac{e^{(\mp 2\pi iwx)}}{x} \\ &\pm iwE(x, y) \otimes \text{sinc}\left(2\pi w\left(x + \frac{1}{4w}\right)\right) \\ &\mp iwE(x, y) \otimes \text{sinc}\left(2\pi w\left(x - \frac{1}{4w}\right)\right) \\ &+ wE(x, y) \otimes \text{sinc}(2\pi wx). \end{aligned} \quad (2.59)$$

This result displays characteristics that might be expected. First, for  $w \rightarrow 0$  it reduces exactly to equation 2.17. Secondly, the first term taken alone is equivalent to the equation used to describe the knife-edge test with the knife edge placed off the optical axis by  $\pm w$ . (Linfoot, 1946) This is exactly the origin of the term in this equation, as the transmission mask must be considered as three separate functions to accomplish the Fourier transform, one of which is  $H(\tilde{x} - w)$  on the first region of  $M^+$ . Using  $U_p^{pm}$ , the signals of this sensor can be calculated using equation 2.23.

## 2.6 Generalization of the PS technique to focal plane masks and the Zernike Phase contrast method

The Foucault knife-edge test is perhaps the most well known of a class of optical tests known collectively as Schlieren tests. As discussed above, it uses a knife edge placed at the focus to cast shadows on the pupil. Using a geometric understanding of light, the observer interprets these shadows based on where rays are intersecting the optical axis near the focus. Although this is very intuitive, it is not the only way to accomplish more or less the same task. The wire test uses a thin wire placed near focus, and produces images which are very similar in appearance to Foucault graphs (they resemble the derivative) (Platzeck and Gaviola, 1939; Malacara, 1978). Other tests employing focal plane masks are the Ronchi grating (an amplitude grating) and a modified Foucault test (a Heaviside step function in phase, not transmission) called the Wolter test. These two, as well as the Zernike phase contrast method have all been given at least a cursory analytic treatment (Barakat, 1969).

One of the more dramatic examples of this generalization is a WFS proposed for Solar Adaptive Optics (von der Lühe, 1988). This WFS uses a very specific focal plane mask based on an image of the sun covering 7500 km<sup>2</sup>. The mask is generated by shifting the image by some number of pixels,  $\Delta$ , and subtracting it from itself. The author goes through a derivation similar to that of C. Vérinaud, 2004 and arrives at an equation for the re-imaged pupil of the same form as the PS with the parameter  $\Delta$  playing the same role as the modulation angle.

Perhaps the most elegant solution of this problem was put forth by Zernike himself (Zernike, 1934). In formulating his method of phase contrast, he points out that the light corresponding to a small phase modulation of the wavefront and the light corresponding to the mean of this wavefront are out of phase with each other by 90°. This can easily be seen by looking at the expansion of the electric field phasor for small phase aberrations and constant amplitude (see equation 2.22). The first term represents the light from the mean surface of the wavefront and the second, the

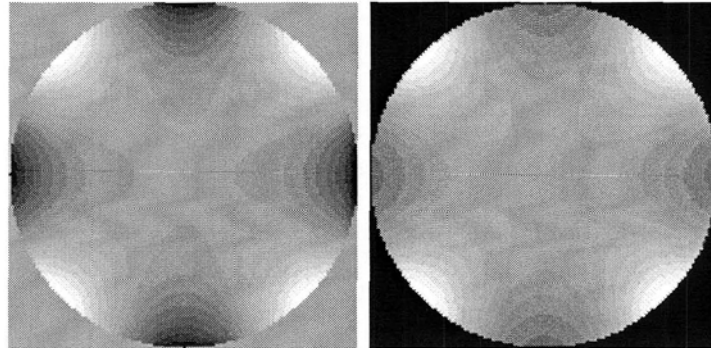


Figure 2.21: **Zernike Phase Contrast WFS Simulation:** The left hand image shows the input wavefront and the right hand image shows the intensity in the detector plane. The resemblance is remarkable and shows the power of the Zernike Phase contrast method in directly imaging the phase.

perturbations on top of this, the factor of  $i$  gives rise to the phase shift of  $90^\circ$ . Thus if the light forming the core of the image is made to pass through a  $1/4$  wave plate then the two components will again be in phase and the observer will see the surface of the phase error directly. This rather stunning idea is the basis of the phase contrast microscope and Zernike's Nobel Prize (1953).

This idea is also employed to build a WFS for AO (Carhart et al., 2000; Vorontsov et al., 2000; Bloemhof and Westphal, 2002; Bloemhof and Wallace, 2003). The CAOS routines for simulating the PS can be adapted to simulate a Zernike phase contrast WFS by changing the mask from the phase mask representing the pyramid to one with a  $\frac{1}{4}$  wave plate in the centre of size  $\sim \frac{\lambda}{D}$  (the diffraction limit of the telescope).

Figure 2.21 shows the input and result of such a calculation. The left hand side is the input wavefront, Zernike mode 26. The right hand side is the image on the WFS CCD. The intensity is proportional to the input phase, and this demonstration shows the potential of such a WFS to directly image the phase.

## Chapter 3

# Guide Star Counts and Interfacing PAOLA with Catalogues

### 3.1 Searching the USNO catalogue

As mentioned previously, PAOLA stands for “Performance of Adaptive Optics Systems for Large (or Little) Apertures”. It has been developed by L. Jolissaint at HIA and employs the principles outlined in section 2.1.1 to calculate the properties of the image plane for the atmosphere, telescope, and AO system. The IDL code is publicly available and its routines are well described in the user manual (Jolissaint, 2003). PAOLA has been used to study the performance of Wide Field Adaptive Optics, one of the potential AO modes considered in the VLOT study and in the TMT project (Stoesz et al., 2004a; Jolissaint et al., 2004b).

Thanks to a synergy between publicly available IDL routines and PAOLA, it is a relatively straightforward task to use the web socket procedures found in the IDL Astronomy User’s Library (astrolib) to allow guide star searches around interesting astronomical targets by interfacing PAOLA with star catalogues. Figure 3.1 shows the flow of information. Using the input atmosphere, i.e.,  $C_n^2$  and wind profile above

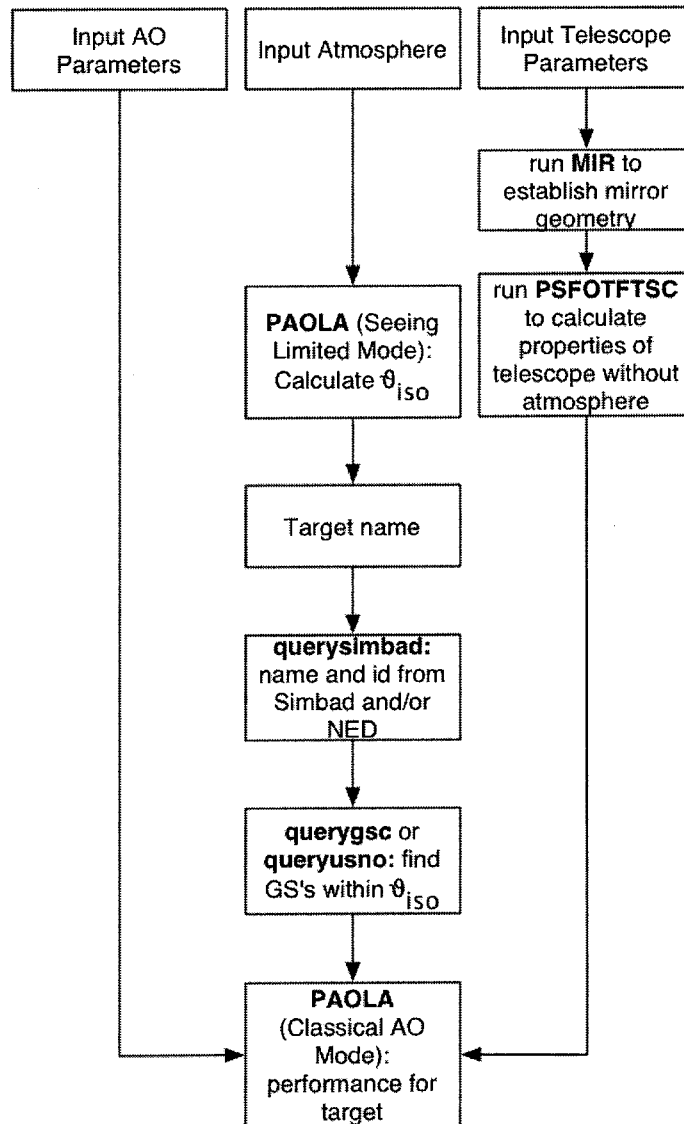


Figure 3.1: Flow chart of PAOLA catalogue interface.

the observatory, the isoplanatic angle,  $\vartheta_{iso}$  is calculated.<sup>1</sup> The `astrolib` routines `querysimbad`, `querygsc`, and/or `queryusno` are used to search for potential guide stars within the isoplanatic patch surrounding the target. If one is found, the parameters of the AO system and telescope can be used to run PAOLA in classical AO mode to determine the performance of the system (Strehl ratio, encircled energy, FWHM, etc) for a specific target.

This type of search was carried out using an atmosphere profile from Mauna Kea (Ziad, 2002). All 2096 galaxies in the Virgo Cluster Catalogue (VCC) were considered as potential targets (Binggeli et al., 1985). The VCC was obtained in digital format from the maintainers of the GOLDMine web database (Gavazzi et al., 2003). The isoplanatic patch for this particular atmospheric model has radius of 15.5'' in K band. Of all of the galaxies, 1149 had at least one star within this angular separation, using the USNO A-2.0 catalogue.

PAOLA was run for a series of different star magnitudes to determine the limiting magnitude of the SH WFS for a telescope with a TMT sized aperture, ~30 m. Figure 3.2 shows the result. A limiting magnitude of 15.5 was chosen to restrict the search. Of the 1149 potential galaxies only 687 had stars which were bright enough. The search was performed again for limiting magnitudes of 16.5, 17.5, and 18.5 to represent the number of accessible galaxies with a PS of magnitude gain  $\Delta m = 1, 2,$  and 3 magnitudes. The resulting numbers of accessible galaxies are summarized in table 3.1. For a TMT sized aperture with a PS at a magnitude gain of 3, 91% of the potential galaxies are accessible for study with classical AO and this corresponds to 49% of the VCC compared to 33% for the SH WFS.

## 3.2 Simulation Results

Simulations were carried out using PAOLA to calculate the Strehl Ratio (SR) for each galaxy with an available GS at each magnitude gain assuming that the PS behaves

---

<sup>1</sup>The  $C_n^2$  profile gives the strength of the turbulent layers as a function of height above the observatory site.

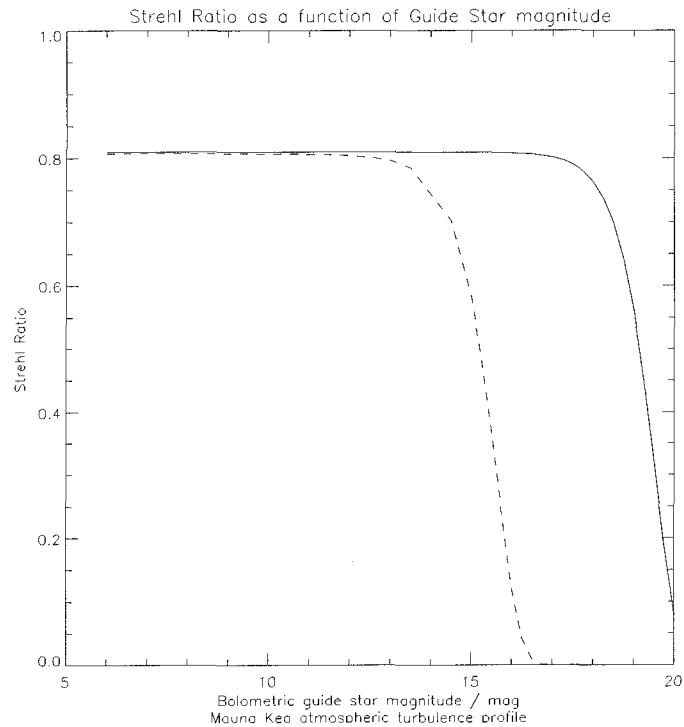


Figure 3.2: **Limiting Magnitude for a SH WFS on a 30 m Telescope:** The plot shows the Strehl ratio on-axis plotted against the magnitude of the GS for the Mauna Kea atmospheric profile. The calculation was performed for L-band ( $\lambda = 3.78\mu\text{m}$ ) and the seeing angle is  $0.7''$  and  $r_0$  is 0.144 m at 500 nm and 1.64 m at L-band. The dashed line is the curve for a SH WFS and the solid curve is the PS with a magnitude gain of 4. The limiting magnitude of 15.5 was chosen from point at which Strehl for the AO system using the SH WFS drops to  $\sim 0.25$ . The AO system has 36 actuators across the 30 m primary.

Table 3.1: **Number of Accessible Galaxies at Different Limiting Magnitudes:** This table shows the results of searching the USNO catalogue for galaxies with GS's in the fourth column and the results of the SR's (L-band) calculated using PAOLA for those galaxies.

sensor	$m_{lim}$	$\Delta m$	$N_{gal}$	$N_{gal}$ (SR > 0.1)
SH WFS	15.5	-	687	567
PS	16.5	1	758	659
PS	17.5	2	871	727
PS	18.5	3	1035	821

like a SH but with the corresponding magnitude gain. The number of galaxies with L-band SR greater than 0.1 is reported in the last column of table 3.1. A SR of 0.1 was chosen arbitrarily, but it serves to exclude those galaxies where the AO system fails to provide a useful level of correction. For the SH case the number of galaxies drops to 567, and 821 for the PS with a magnitude gain of 3. In terms of the total number of targets in the VCC the SH WFS provides useful correction on 27% while the PS with a magnitude gain of 3 covers 39%.

A magnitude gain of 3 represents the most optimistic results from section 2.3.1. A magnitude gain of one or two are perhaps more realistic. With a magnitude gain of 2 the PS provides a SR > 0.1 on 35% of the VCC and with a magnitude gain of 1 the number drops to 31%, compared to the 27% achieved by the SH WFS.

Figure 3.3 shows a histogram of the K-band SR for all of the simulations for the VCC galaxies. It shows the other important effect of the magnitude gain: increasing the number of galaxies at high Strehl ratio. This is due to the fact that a GS that was at the limit of the SH WFS, 15.5 mag, delivers the performance of a 12.5 magnitude GS when used with a PS. Thus, the PS moves galaxies that are in the lower Strehl bins in the SH WFS case into higher Strehl bins and brings galaxies that were not accessible into the lower Strehl bins.

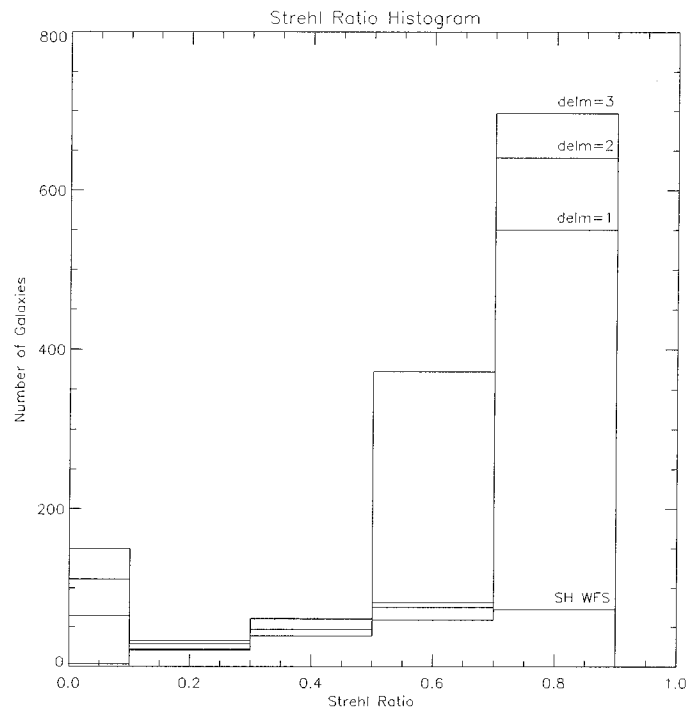


Figure 3.3: **Strehl Ratio Histogram for VCC Galaxies:** This plot shows a histogram of the Strehl Ratios (K-band) calculated using PAOLA. Notice that the number of galaxies in the highest Strehl bin grows dramatically with increasing magnitude gain.

Table 3.2: **Bahcall and Soneira Star Densities:** This table shows the star densities estimated from plot 4(c) in Bahcall and Soneira, 1980. The third column shows the number of stars per isoplanatic patch associated with atmospheric profile used above. The sky coverage is much lower than that calculated by searching the USNO catalogue.

$m_{lim}$ (mag)	$N_{m \leq m_{lim}}$ (stars/deg <sup>2</sup> )	$N_{m \leq m_{lim}}$ (stars/patch)	$N_{gals}$
15.5	180	0.011	23
16.5	390	0.023	48
17.5	650	0.038	80
18.5	1000	0.058	122

### 3.3 Caveats to the Guide Star Search

The usual model of the distribution of stars in the Galaxy used to estimate the sky coverage is Bahcall and Soneira, 1980. From the results in that work the density of stars on the sky at a galactic latitude of  $90^\circ$  can be used to estimate the number of guide stars available for VCC galaxies which lies between a galactic latitude of  $62.8^\circ$  and  $82.6^\circ$  (Gavazzi et al., 2003). Table 3.2 summarizes the results of the Bahcall and Soneira model. The third column shows the number of guide stars per isoplanatic patch used in the USNO search. The sky coverage is much lower and does not agree with the USNO catalogue. The reason for this has to do with two main issues with the catalogue: it is incomplete around bright objects and registers some galaxies themselves as sources (Gwyn, 2005). These effects represent a practical limit to automated guide star searches using the USNO catalogue. However, according to the Bahcall and Soneira model there is still a factor of  $\sim 6$  improvement in sky coverage at high galactic latitude for a PS with a magnitude gain of 3.

## Chapter 4

# Laboratory work with 1d Pyramid Wavefront Sensor

This chapter contains a description of all of the experiments carried out with the PS prototype in the UVIC AO lab. The first part of the experimentation was devoted to studying the utility of a light diffusing element in performing linear measurements of the wavefront tilt over a large dynamic range (Ragazzoni et al., 2002b). The diffuser does indeed linearize the sensor, given certain caveats, and hence this experiment yields a linear calibration curve between the incoming tilt and the PS signals. With this piece of information, it was possible to measure an arbitrary aberration. However, the experimental setup presented some unique complications which made the measurements of the arbitrary static aberration, introduced into the beam using a CD cover, difficult to analyze.

The final stage of the experimentation involved measuring wavefronts generated by the Hot-Air Turbulence Generator (turbulator). This device is another piece of AO hardware under development at the UVIC AO lab (Keskin, 2003). Data was collected with both a reference SH WFS (the mini-Wavescope) and the PS with the intention that a comparison of the temporal and spatial properties of the turbulence measured with both sensors would give confidence that the PS is working properly. These experiments elucidated some previously unseen complications with the turbu-

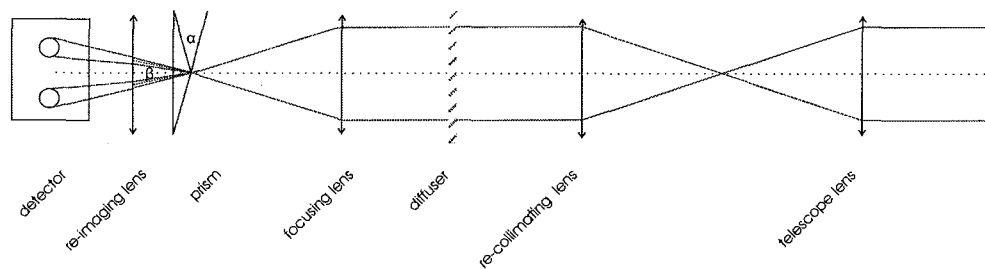


Figure 4.1: **Schematic Diagram of the PS with a diffuser:** The layout of the PS implemented with a diffuser is shown. In this case the first lens represents the telescope. The beam is re-collimated and passes through the diffuser. It is then refocused onto the prism, and the pupils are re-imaged on the detector by another lens. The angle  $\alpha$  is the vertex angle of the prism and the angle  $\beta$  is the angle at which the beams diverge after the prism.

lator and allowed the experimentation with the PS to feed back into the turbulator development. These issues will be discussed in section 4.6

## 4.1 Design and Layout

### 4.1.1 Component Considerations

Figure 4.1 shows a schematic diagram of the PS. It consists of 6 major components: fore-optics which re-collimate and resize the beam coming from the telescope focal plane, a system to modulate the beam (a diffuser in this case), a lens to refocus the beam, a spatial filter (the pyramid or prism), pupil re-imaging optics, and the detector. The main considerations for the design of a PS are clearly outlined in previous work (Riccardi et al., 1998). The system presented in Riccardi et al. used a tip tilt mirror to provide modulation, but the basic layout of a PS employing static modulation is given in Ragazzoni et. al., 2002. The following discussion will be focused on the particulars of the equipment used to build the PS for the UVIC lab.

The apex angle of the pyramid is a primary consideration for the optical design of the PS. The light which is focused at the apex of the pyramid is split into four beams (two for a prism). These beams diverge at an angle  $\beta$  which is related to the apex angle  $\alpha$  (see figure 4.1) by

$$\beta = (n - 1)\alpha \quad (4.1)$$

where  $n$  is the index of refraction of the glass used in the pyramid (1 has been used for the index of air) and the small angle approximation of Snell's Law has been used (Riccardi et al., 1998). Since the beams themselves are also diverging with an F-number,  $F$ ,  $\alpha$  must obey

$$\alpha \geq \frac{\sqrt{2}}{F(n - 1)} \quad (4.2)$$

to avoid overlap of the beams. For most systems, this indicates that the best choice is to have a pyramid which is nearly flat, that is  $\alpha \sim$  a few degrees because the input F-number is in the range of  $20 \rightarrow 30$ . For the 1d PS the angle is set by the prism which has  $\alpha = 20^\circ$ . Thus, the divergence of the beam is quite large meaning smaller F-numbers can be used.

Other physical properties of the pyramid which impact the design are the roof and edge quality. The spatial filtering provided by the pyramid is dependent on the quality of the surface near the apex. The presence of a roof (a flat region at the apex) and/or turned (rounded) edges are unavoidable if optical polishing is used to produce the pyramids because the grinding of the fourth edge cannot be stopped at the precise moment when its facet intersects the other three. (Ragazzoni et al., 2000b)

For a single PS working in a classical AO system, the roof impacts the capacity of the pyramid to provide the necessary spatial filtering if the size of the roof becomes a significant fraction of the PSF formed on the apex of the prism. Early estimates based on the diffraction limited size of the PSF core of the TNG (F/32) gave acceptable roof sizes of  $\sim 5 \mu\text{m}$ , with roof sizes of 9-13 $\mu\text{m}$  actually achieved in fabricated prisms (Ragazzoni et al., 2000b). Interestingly the constraint on the angle becomes even more stringent when multiple pyramids are used to optically co-add the light of multiple guide stars in a layer oriented wavefront sensor because not only is the

roof required to be small, but each pyramid must have the same apex angle to a very tight tolerance,  $1.382^\circ \pm 0.005^\circ$  (Ragazzoni et al., 2001). Alternate methods to optical grinding become highly desirable. One technique that has been researched involves producing the pyramids by using Deep X-ray lithography at a synchrotron (Perennes et al., 2001; Perennes et al., 2003). The idea in this case was to mass produce the pyramids, measure the angles and use the ones with the most consistent angles. However, the size of the batch of pyramids required to get enough (10) with the right angles was too high for this to be feasible (Ragazzoni, 2004). It has also been suggested that pyramids could be mass produced using high electron beam sensitivity (HEBS) glass (Kirk et al., 2004). Another solution to this problem that was presented in the literature is a double sided achromatic pyramid. The doubled sided pyramid has two prisms back-to-back. Each prism has an apex angle which is larger than the standard prism, but in this case it is the difference of the angles which provides the net deflection comparable to the standard prisms. (Diolaiti et al., 2003) However, it is still possible to meet the tight specifications by optical polishing (Lombini et al., 2004).

Although the fabrication of the pyramids is an interesting problem, it is not a concern for the 1d PS because it employs a prism. Turned edges become a greater problem when the apex angle is small, which is not the case for the prism either. Furthermore, the diffuser enlarges the PSF core on the prism apex making the performance of the system resilient to the presence of a roof.

Another consideration is the size of the detector. This parameter sets the magnification of the re-focusing lens and the pupil re-imaging lens. With the apex angle of the pyramid in mind, the positions of the pupil images on the detector must be chosen, and the size scale here determines the ratio of the focal lengths of the re-focusing lens and the pupil re-imaging lens. For the 1d PS case the thickness of the pyramid also becomes a factor, as it can limit the range of focal lengths that can be used for the re-imaging lens. The combination of the large apex angle of the prism, the thickness of the prism (12 mm), and the small size (2.1x2.1 mm) of the CCD, lead to a compromise in the pupil re-imaging for the 1d PS. The detector is off-set from the optical axis so that it captures one of the two re-imaged pupils, not both. This

is acceptable, though not ideal, for a 1d device because the re-imaged pupils contain the same information, as can be seen from equation 2.17.

### 4.1.2 Zemax Layout

The Zemax ray tracing program was used to design the PS for the UVIC AO lab. Keeping in mind the considerations mentioned in the last section, the design proceeded by finding the appropriate lenses and optimal spacing to re-image the diffuser plane onto the CCD detector through the prism. The final layout used to design the component mountings is shown in figure 4.2. The diffuser plane is shown on the far left of the image. Rays were launched from the diffuser at various positions along the section through which the beam passes. At each position, rays of field angles of  $0^\circ$ ,  $0.05^\circ$ ,  $0.1^\circ$ ,  $0.15^\circ$ ,  $0.2^\circ$ , and  $0.25^\circ$  were used. The field angles were used to account for the spreading of the beam by the  $0.5^\circ$  diffuser. These rays were propagated through the focusing lens, the prism and the re-imaging lens to land on the detector. The diffuser and the detector must be conjugated, meaning that all rays launched from each position must intersect at the detector plane. Imagining the system without the prism, the conjugate plane must be at a distance of the sum of twice the focal length of the focusing and re-imaging lenses from the diffuser. This requires some fine tuning.

The rays of different field angles do not intersect in one plane, but create a blur spot. Furthermore, the circle of least confusion, i.e., the circle encompassing the blur spot that has the smallest diameter, is at different positions along the optical axis as one moves from the top to the bottom of the re-imaged pupil shown in figure 4.2. The blur can be made roughly uniform by choosing a plane between that of the circle of least confusion for the top of the diffuser and that of the bottom of the diffuser.

Interestingly the blur spot is used to estimate the size of the subapertures used in a PS (Ragazzoni et al., 2001). The subapertures divide up the re-imaged pupil into discrete points at which the slope is measured. The rule of thumb is that the subaperture should be 10 times larger than the blur introduced by the optics. This

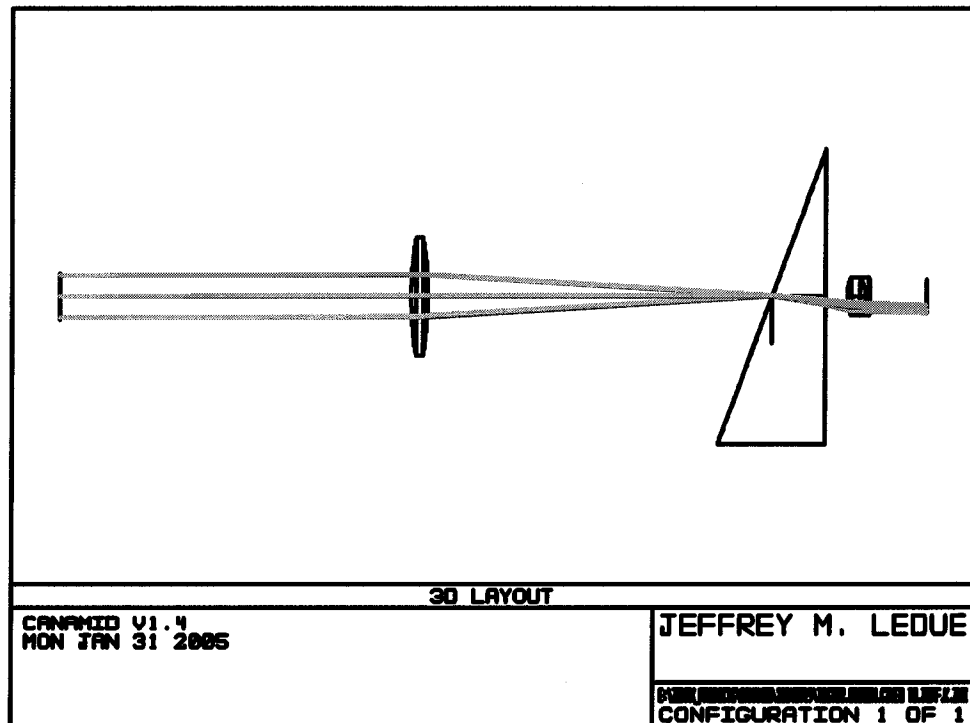


Figure 4.2: **Zemax Layout of 1d PS:** The layout of the 1d PS is shown in this figure. The diffuser plane is on the far right. Rays launched from this plane first pass through the re-focusing lens (achromat with  $f=75$  mm and  $\phi=25$  mm). The prism follows this lens, and it has been modeled as a wedge. The vertical line within the prism is simply an opaque surface programmed into the Zemax model to prevent rays from passing through the wedge below the optical axis. Immediately following the prism is the pupil re-imaging lens (achromat with  $f=16$  mm and  $\phi=8$  mm). Following this is the plane of the detector.

is not a rigorous result of a calculation or a simulation, the factor of 10 is chosen to minimize the contribution of the re-imaging in the error budget in case of MAD while at the same time not making the repeatability condition on the apex angle impossible to meet. For the UVIC 1d PS, the blur introduced is approximately 0.5 to 0.8 pixels on the DALSA CCD. This means that to satisfy the rule of thumb the subapertures for the PS should be 5x5 pixels and greater in size. However, part of the blurring here is due to the large field angles necessary to accommodate the diffuser, and hence smaller subapertures can be used. However, the diffuser has properties of its own which make larger subapertures desirable, which will be discussed later. It should be noted that the number of subapertures provides the fundamental limit on the number of modes the PS can measure. The number of sensed modes cannot exceed the number of subapertures without extrapolation.

Figure 4.3 shows the appearance of re-imaged pupil on a 2.1x2.1 mm, 128x128 pixel CCD calculated using Zemax. As mentioned above, due to the large apex angle of the prism a compromise was made and the detector was placed with its centre 1.5 mm offset from the optical axis allowing only one of the re-imaged pupils to be captured.

The mountings for the 1d PS were designed by J. Kennedy. The prism was mounted onto a Newport M460 A tri-axis linear stage, to allow positioning of the prism in the focus spot with the stages' micrometer screws. The re-imaging lens was also mounted on a stage to allow its position along the optical axis to be adjusted. The entire CCD and re-imaging lens assembly was mounted on another stage to allow positioning perpendicular to the optical axis. this arrangement gave ample flexibility and precision to align the system.

Figure 4.4 shows an image captured with the DALSA CCD of the re-imaged pupil. Note the Rayleigh ring which is absent from figure 4.3 because Zemax performs geometrical ray tracing. The series of images in figure 4.4 demonstrates the 1d sensitivity of the 1d PS. The bar in the images is an allen key which has been inserted into the beam at the stop. It has a bright edge due to the PS's sensitivity to a phase step, producing a Rayleigh ring-like feature. In the first image the allen key is aligned with the prism apex. and the long edges appear bright but the short end which has gradient perpendicular to the knife edge is not detected. In the next image the allen

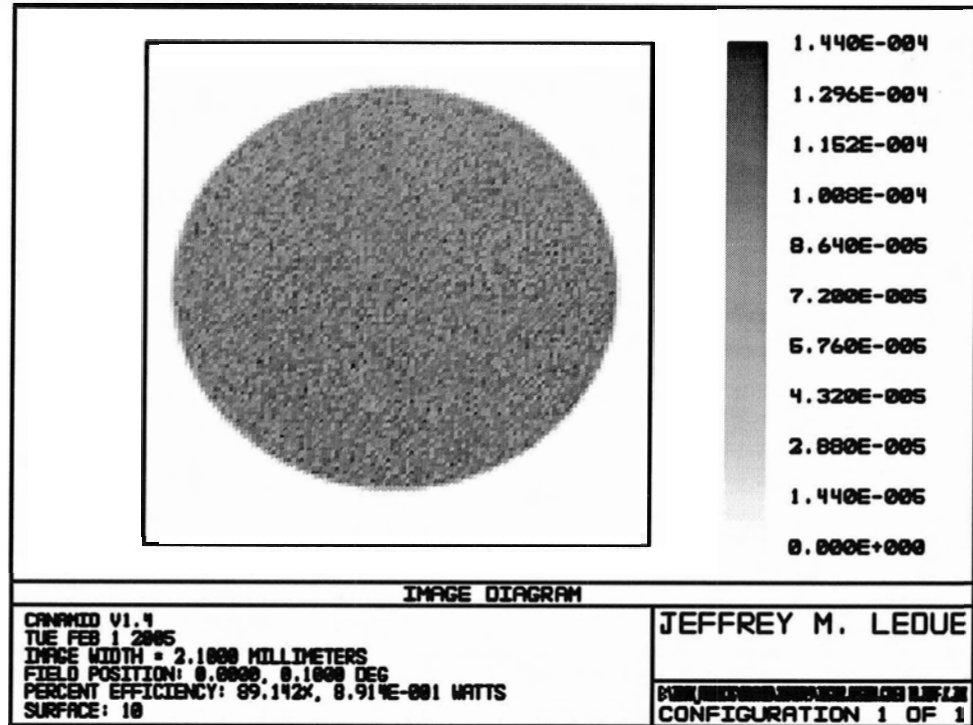


Figure 4.3: **Zemax Calculation of the Re-imaged pupil:** This figure shows the re-imaged pupil on the PS detector calculated using Zemax. The detector size is 2.1x2.1 mm with 128x128 pixels, matched to the parameters of the DALSA CCD. The input beam diameter is 9 mm. The elliptic shape of the pupil can be discerned. The aspect ratio ( $y/x$ ) is 0.93. This was measured in the real images to be 0.94. This astigmatic effect is caused by the large apex angle of the prism. The spotted appearance of the figure does not suggest that the diffuser is present. The intensity fluctuations here are a result of the rays launched by Zemax to do the calculation, and, as such, represent minute variations compared with those discussed in section 4.2.4.

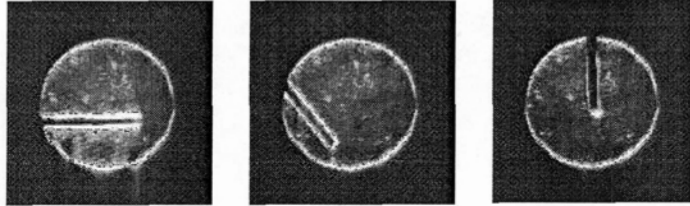


Figure 4.4: **Demonstration of 1d Sensitivity:** An allen key placed at the stop viewed on the DALSA CCD. The orientation of the allen key is rotated from  $0^\circ$  to  $45^\circ$  to  $90^\circ$ . Edges that have a component aligned with the prism cause a phase step in the perpendicular direction which results in the bright outline. Thus, the end of the key is absent in the far left panel, while the sides are absent in the far right panel. In the middle the orientation is such that all edges have a component along the direction defined by the prism and the whole key is outlined.

key has been rotated by  $45^\circ$ . All of the edges of the key are visible because their gradients all have a non-zero  $y$  component. In the final image the key is oriented at an angle of  $90^\circ$  to the first position, and the short edge is visible and the long edges are not.

## 4.2 Calibration

### 4.2.1 Principle

The principle of the calibration of the PS is straightforward. A tilt is introduced into the beam by a fold mirror. It is measured with the reference SH WFS and the image on the PS camera is recorded. Despite the fact that only one of the two re-imaged pupils is recorded by the CCD camera the total intensity must be linearly related to the input tilt if the diffuser does in fact provide a modulation effect.

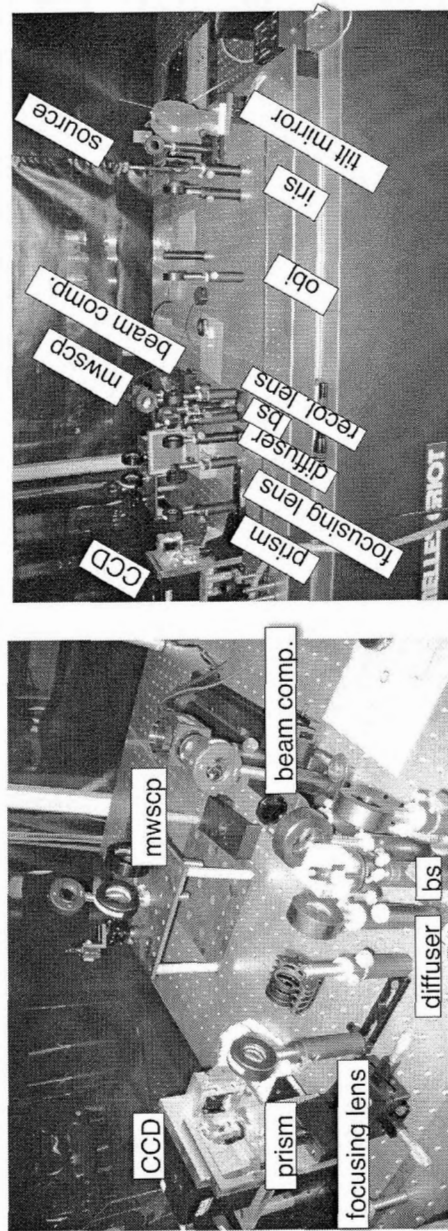


Figure 4.5: **Calibration Setup:** This photograph shows the bench setup used in the calibration of the 1d PS. The mirror in the foreground of the right hand photograph was used to introduce a tilt into the beam which was measured by the mini-Wavescope. The intensity on the PS camera was recorded and used to derive a calibration curve. The left hand photograph shows a close up of the two arms of the setup.

Table 4.1: **Description of Equipment Used:** The table gives a brief description of the equipment used in the lab setup.

Item	Description
Source	Seastar Optics AC-9400 Power Unit Seastar Optics LD-2310 laser diode driver Toshiba TOLD9215 laser diode Gould 2x1 fiber coupler
Collimating lens	EO $\phi=25$ mm, $f = 300$ mm achromat linear stage
Fold mirror	Melles Griot, $\frac{\lambda}{20}$ , $\phi=100$ mm mountings by J. Kennedy
Iris	EO: NT37-919 30 mm adjustable aperture
Objective lens	EO $\phi=25$ mm, $f=175$ mm achromat
Re-collimating lens	EO $\phi=25$ mm, $f=75$ mm achromat
Beamsplitter	cube
Beam compressor	Melles-Griot $\phi=25$ mm, $f=100$ mm EO $\phi=25$ mm, $f=50$ mm achromat
mini-Wavescope	SH WFS (AOA) 26x26 subapertures 0.5 cm beam
PS	prism mounted on Newport M460 A Series linear stage
CCD	DALSA CA-D1-0128A BitFlow Roadrunner Framegrabber Vision 1 Power Supply P4 3GHz control computer

### 4.2.2 Laboratory Setup and Data Collection

The bench setup used to calibrate the 1d PS is shown in figure 4.5 and details of the equipment used are listed in table 4.1. The fiber light source was collimated by an achromat mounted on a linear stage. The collimation was checked using a shear plate. The beam was then reflected from the fold mirror visible in the foreground of the photo. The mounting of the mirror was equipped with set screws that allowed it to be tilted. The beam was then passed through the iris, the stop of the system, and through the objective lens which simulated the primary of the telescope. It was re-collimated by another achromat and sent through a cube beam splitter. One arm of the beam then proceeded through a pair of lenses to the reference SH WFS, the mini-Wavescope. The other arm of the beam proceeds to the PS. It is re-focused onto the apex of the prism which splits the light into two beams. The pupils are re-imaged by another lens located behind the prism ( $\phi = 8 \text{ mm}$ ,  $f = 16 \text{ mm}$  achromat) and one of the pupils lands on the CCD. The DALSA CCD is used in the SH WFS employed on the AO system in the UVIC AO lab. It has been tested by B. Wallace and found to perform to spec (Wallace, 2005). The DALSA used for the 1d PS experiment performed similarly except that the mean bias level was about 2 digital units greater than the mean value stated in the spec.

The PS data for the calibration consists of frames collected from the DALSA CCD by a program written by A. Hilton running under QNX. The `focusfinder` application displays the CCD image and allows the user to save the frame. This program was used in the initial attempts of the calibration experiment. Subsequently, a version of `Snap5000` (discussed later in section 4.4.2) called `Snap30` was created to save 30 consecutive frames from the camera. The purpose was to allow 30 frames to be saved of the same tilt measurement to allow the measurement errors to be estimated from the standard deviation of the sample.

The mini-Wavescope is a commercially available SH WFS produced by Adaptive Optics Associates. Its software requires the user to create a test before recording data. For the calibration of the PS, the test `ps.cal` was created, the important feature of which is a text display of the coefficients of Zernike expansion of the wavefront.

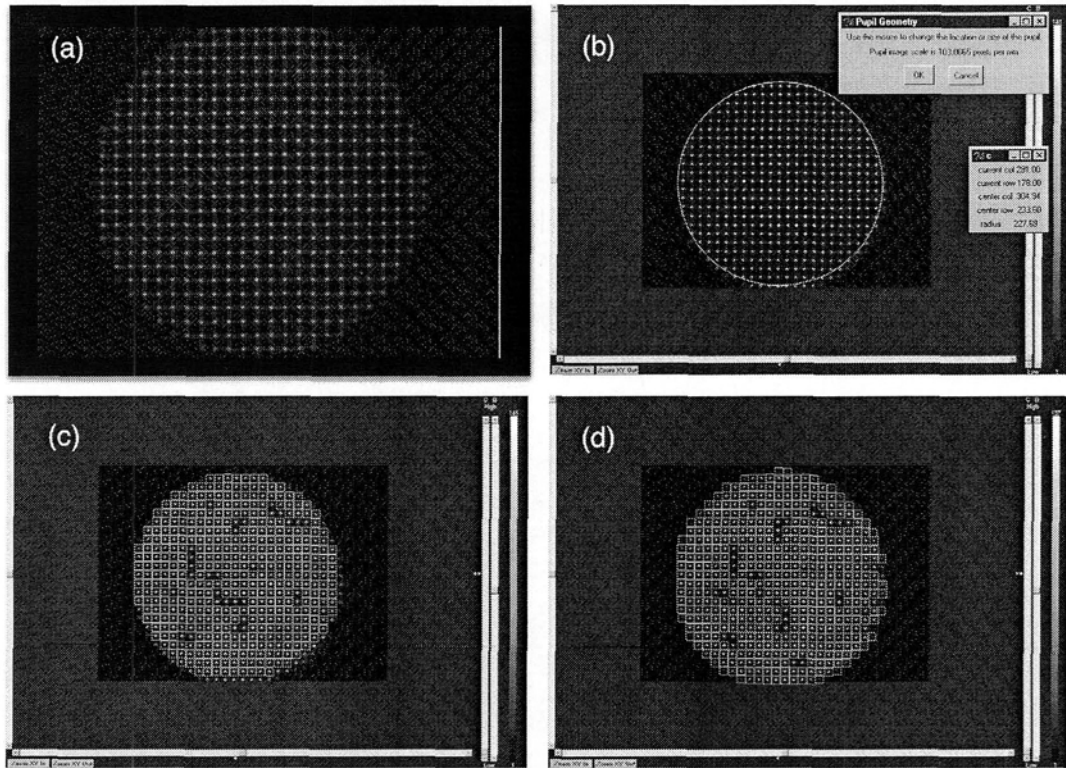


Figure 4.6: **Mini-Wavescope Calibration Procedure:** The mini-wavescope's software has a built in routine which leads the user through the calibration procedure. Panel (a) shows the a screenshot from the first step in which the user is shown a live display of the image on the mini-wavescope's Pulnix TM-7 CCD camera and is asked to verify the intensity of the spot pattern. The TM-7 is equipped with a hand activated trigger to change the exposure time of the camera to avoid saturation. Panel (b) shows the display where the user is asked to select the pupil. This is used in the reconstruction of the wavefront and calculation of Zernike polynomials. Panel (c) shows the reference subapertures and (d) shows the test subapertures. The mini-Wavescope always allows the user to have a reference and a test configuration. For the experiments that follow, the reference and the test are always the same. The only difference is that the two sets of subapertures may not always include exactly the same active ones. This is due to the way in which the mini-Wavescope's software selects the valid subapertures. It has no real practical implications for this work other than to cause unnecessary confusion.

The procedure developed to collect the calibration data consists of a number of steps. The diffuser was removed from the PS to allow the diffraction limited image (of the pupil) to be viewed in real time using the `focusfinder` application. The tilt of the beam and height of the prism were adjusted until the Rayleigh ring pattern was clearly centred in the image on the CCD. At this point the diffuser could be put back into the system. Next, the mini-Wavescope was calibrated. This is a multi-step process outlined in figure 4.6. With the system in this configuration the mini-Wavescope reads a negligible Zernike coefficient of y-tilt. The test is then run in live display mode and the set screw on the fold mirror is turned *very* slowly until a desired maximum tilt (positive or negative tilt) is reached. Thirty individual mini-Wavescope runs are saved using one frame only, again to estimate errors, and another run saving the average of thirty frames was collected. `Snap30` is run to collect the PS frames. The set screw is then turned back slightly and measurements are again taken.<sup>1</sup> Note that 30 individual measurements for the mini-Wavescope were taken only at the two extremes of the tilt range covered as well as one point near zero in the interest of saving time. It is important to move the mirror only in one direction during the course of the data collection due to backlash in the set screw.

### 4.2.3 Data Analysis and Results

The data was analyzed using the IDL software package from RSI. Each frame from the PS was read in and bias subtracted. The pupil was masked out and the intensity was integrated over the masked area. For each of the tilt measurement the average of the 30 intensities as well as its variance was recorded. To get the calibration curve, a linear fit was performed to the intensity vs tilt data. This allowed the intensity level corresponding to zero tilt to be estimated. This value was then subtracted from each of the intensity measurements and the resulting differences were divided by the same value to give the fractional change in intensity as reported on the y axis of the calibration curves below.

---

<sup>1</sup>The resolution of the measurements of tilt using this setup are limited by one's ability to turn the set screw miniscule amounts. A 2" mirror mounted on a tip-tilt stage with micrometer screws could be used to improve the resolution.

Table 4.2: **Calibration Slope, 1° Diffuser:** This table gives the value of the slope of the calibration curve calculated for a circular subaperture placed at four positions within the pupil. The subaperture has a diameter of 6 pixels, while the pupil has a diameter of 101 pixels.

coordinates	slope
$(x_c = 30, y_c = 60)$	$0.72 \pm 0.04$
$(x_c = 80, y_c = 60)$	$1.23 \pm 0.03$
$(x_c = 80, y_c = 30)$	$0.80 \pm 0.09$
$(x_c = 30, y_c = 30)$	$0.69 \pm 0.03$

### 0.5° Diffuser

The global calibration curve for the PS using the 0.5° diffuser is shown in figure 4.7. The slope, i.e. calibration constant, is  $1.62 \pm 0.03 \text{ mrad}^{-1}$ . The slope is not constant over the area of the diffuser. Figure 4.8 shows a histogram of the calibration constant calculated for each of the  $\sim 400$  active subapertures of the mini-Wavescope used in the measurement of a static aberration. The sensitivity of the PS shows quite a skewed distribution. While the mean and median values are close to the global slope (i.e., the calibration constant given by the slope of the line in figure 4.7), the distribution is peaked at  $\sim 1 \text{ mrad}^{-1}$ . This means that a minority but significant number of subapertures  $\sim \frac{1}{4}$  will overestimate the slope by  $\sim 50\%$ .

### 1.0° Diffuser

The global calibration curve for the PS using the 1° diffuser is shown in figure 4.9. The slope for the 1.0° diffuser is  $0.89 \pm 0.01 \text{ millirad}^{-1}$ . This is approximately half the value for the 0.5° diffuser and this would be expected because the image formed on the apex of the PS would be about twice as large and this would result in a drop in sensitivity of roughly the same amount.

To verify that the same non-uniform sensitivity was present in the 1.0° diffuser, four circular subapertures were placed at different coordinates within the DALSA frame

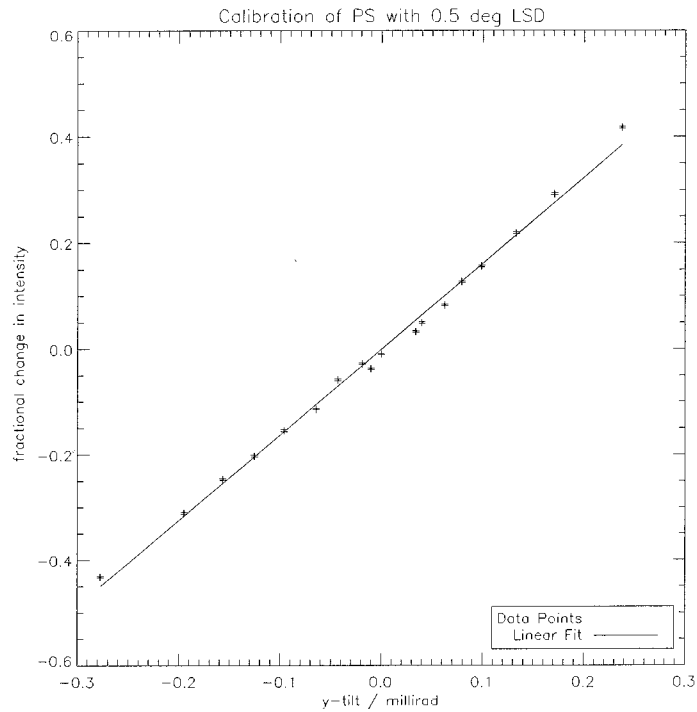
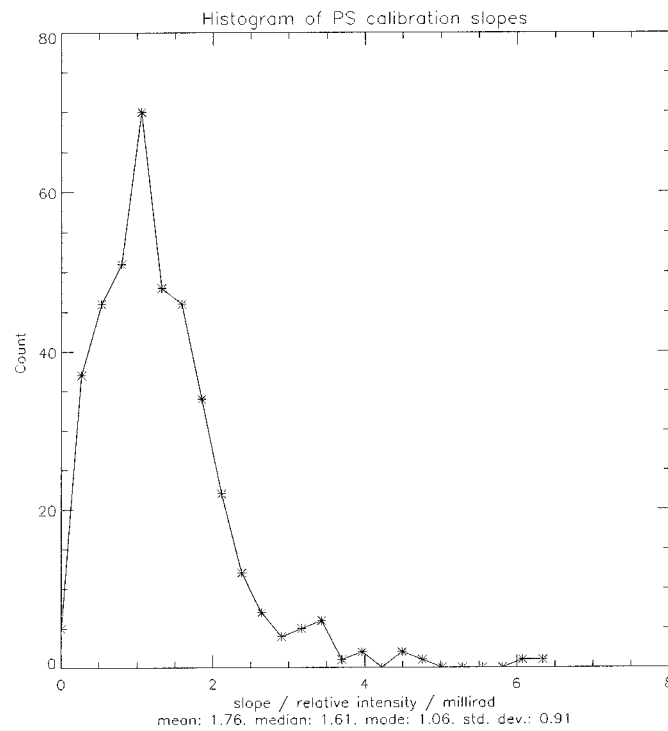


Figure 4.7: **Calibration Curve for 0.5° Diffuser:** The plot shows the relative change in intensity observed on the DALSA CCD, as a function of the tilt measured by the mini-Wavescope. The slope is  $1.62 \pm 0.03 \text{ mrad}^{-1}$ . The mini-Wavescope has an absolute error specification of better than  $0.006 \text{ mrad}^{-1}$  and a relative error specification of better than  $0.003 \text{ mrad}^{-1}$ . The largest standard deviation of the tilt measurements for the mini-Wavescope was  $0.0001 \text{ mrad}^{-1}$ . The largest standard deviation of the intensity in the re-imaged pupils at each tilt value is 0.2%. Errors have been plotted but are too small to clearly see.



**Figure 4.8: Histogram of the Calibration Constant for the  $0.5^\circ$  Diffuser:** This plot shows the distribution of the PS calibration constants using the  $0.5^\circ$  diffuser. The mean of the individual calibration constants is  $1.765 \pm 0.007 \text{ mrad}^{-1}$  while the median is  $1.61 \text{ mrad}^{-1}$ . The mode is  $1.05 \text{ mrad}^{-1}$ . The points in the lowest sensitivity bin are illuminated, as can be seen from figure 4.11, but do not change much with tilt.

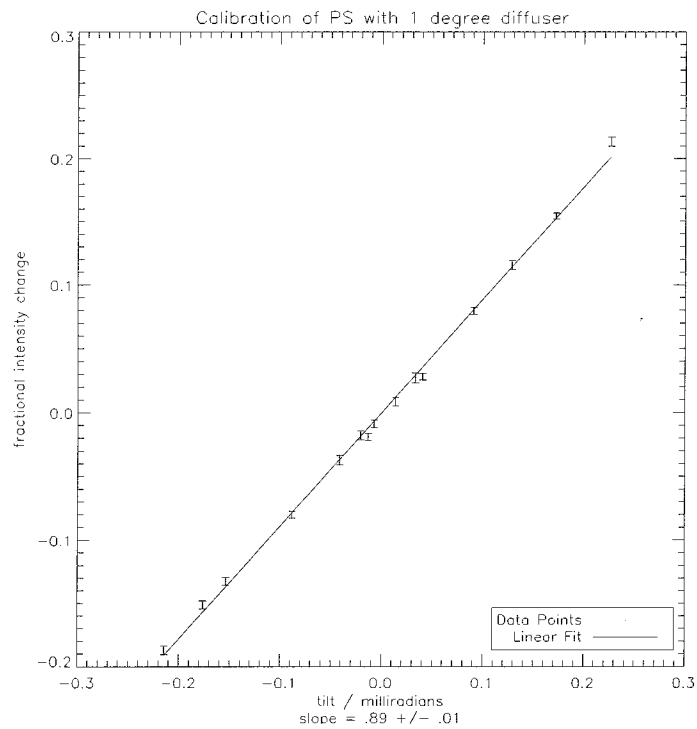


Figure 4.9: **Calibration Curve for 1.0° Diffuser:** This plot shows the same information as figure 4.7 for the 1° diffuser. The slope in this case is  $0.89 \pm 0.01 \text{ mrad}^{-1}$ . As with figure 4.7, the error bars are plotted but are difficult to discern. The largest standard deviation of a particular tilt measurement with the mini-Wavescope was  $0.0009 \text{ mrad}^{-1}$  and 0.4% for the PS intensities.

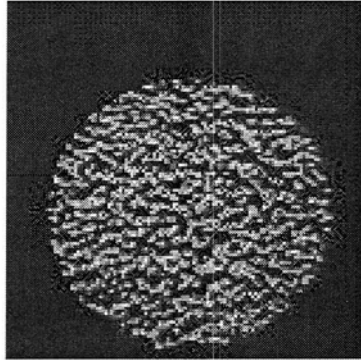


Figure 4.10: **PS Pupil image from the PS CCD with the 0.5° diffuser:** This image of the re-imaged pupil shows the grainy appearance of the surface of the diffuser.

and the calibration curve was recalculated. The results are summarized in table 4.2. The data in this table is meant to show only that the sensitivity of the 1.0° diffuser varies as well. No further analysis of the 1.0° diffuser was performed as it was not used for any of the experiments with the turbulence generator.

#### 4.2.4 Caveats to Modulation using a Holographic Diffuser

##### Non-Uniformity

The non-uniformity of the calibration constant of the PS using the diffuser is made clear by figure 4.8 and table 4.2. This effect is linked to the way in which the diffuser and the PS work. Figure 4.10 shows an image of the pupil recorded on the PS CCD. It shows the characteristic grainy appearance of the diffuser. The diffuser operates by diffracting the light passing through it in such a manner that an image formed after it is blurred by a Gaussian. The FWHM of this Gaussian is given in degrees by the diffusing angle of the diffuser (0.5° and 1.0° for the two tested here). To produce the desired optical effect on a beam of diameter,  $D$ , the diffuser must affect all spatial frequencies from a large value (smallest features distinguished in the image) down to spatial frequencies of order  $\frac{1}{D}$ . The diffuser will have its intended effect on the whole

beam, but considering only the light coming from a pencil of rays that represents one subaperture, then the effect of the diffuser might be a little more or less than the average on this smaller beam. Thus, the sensitivity will vary from location to location as the pattern on the diffuser is random.

### Brightness Variation

Figure 4.10 shows the re-imaged pupil on the DALSA CCD. The brightness varies from point to point across the beam. This is again a consequence of the fact that the diffuser operates by diffraction. To cause diffraction, the diffuser must have features which are on the scale of the wavelength of the incident light just as a diffraction grating does. These are etchings in the polycarbonate substrate of the diffuser. The diffuser causes the pencil of rays that pass through it to fan out, and, as such, acts like a self-luminous object. However, as part of the pyramid sensor, the diffuser is optically conjugated to the detector, and an image of its surface will be seen on the CCD. Thus, in this configuration, the brightness variations are unavoidable. These variations do not pose a problem for the calibration, as with the first effect, but with the use of the CCD. Ideally the entire dynamic range of the CCD could be used for measuring the wavefront slope, but with the DALSA CCD most of the dynamic range was used to accommodate the diffuser.

One possible work-around for this effect is to use a diffuser with a larger angle. The grainy pattern enabling the diffuser to cause diffraction is much less noticeable for higher diffusing angles. This is a result of the fact that at low diffusion angles the surface features needed to cause diffraction are larger simply because less of an effect is required. However, this is not really a preferred avenue for measuring turbulence as the aberrations are small and any increase in angle will cause a loss in sensitivity. The  $0.5^\circ$  diffuser is already a compromise in this regard as it was the smallest diffusion angle available at the time, and already large compared to the effect of the turbulence.

Another idea for mediating this effect of the diffuser was to have the diffuser out of focus. That is to say move it out of the plane conjugate to the stop and detector. When a tip-tilt mirror is used to provide modulation for the PS, it must be placed in

a plane conjugate to the stop and detector so that it does not cause a displacement of the beam perpendicular to the optical axis. The diffuser, on the other hand, causes no such displacement of the beam no matter where it is placed or which particular area of the diffuser's surface is used. However, since the diffuser acts like a self-luminous object, if moved from a plane conjugate to the detector, it will appear out of focus on the detector. The point to point variations in brightness are smoothed out, but the sharp edges of the pupil are gone and the image appears to have a roughly Gaussian profile which is peaked in the centre of the pupil and fades toward the edges. Thus, this approach is not a viable solution because the subapertures are blurred together in the re-imaged pupil.

It was also believed that the main effect of the diffuser was a defocus, and as such it could be approximated as a negative lens. Thus, by repositioning of the refocusing lens the spot size on the apex of the prism could be reduced, making the use of a high angle diffuser practical. While it is indeed the case that the re-positioning of the optics has the desired effect it was observed to be too small to be of use.

Figure 4.11 demonstrates that the two effects are not linked. It shows the sensitivity of a PS subaperture plotted against its integrated intensity in pixel levels. There is no clear correlation between the two effects, other than the outliers at the high sensitivity end are all low intensity.

### 4.3 Measurement of a Static Aberration

This section describes the first experiment done to make a measurement of an arbitrary aberration with the PS. The experiment was referred to as 'the CD Cover experiment' because the cover of a CD case was placed in the beam after the tilt mirror, in the filter holder visible in front of the iris in figure 4.6. The wavefront was altered across the beam by the varying thickness and/or density of the plastic of the CD cover giving an arbitrary static aberration.

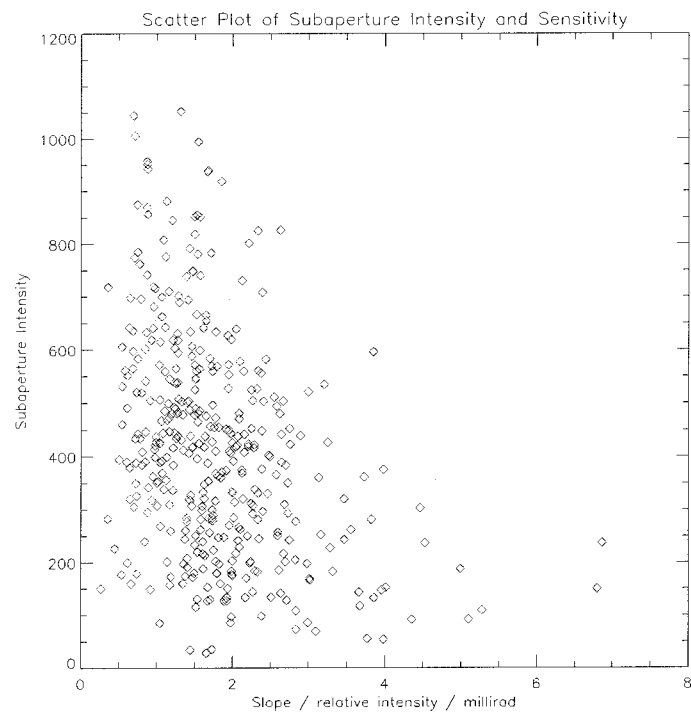


Figure 4.11: **Scatter plot of sensitivity and intensity:** This plot shows the intensity integrated over a subaperture against the corresponding calibration constant. There is no obvious correlation between the two parameters.

Table 4.3: Zernike Coefficients of CD Cover Aberration:

mode	coefficient ( $\mu\text{m}$ )
x-tilt	-0.52
y-tilt	-1.31
focus	-0.04
0° Astig.	0.36
45° Astig.	0.28
x-coma	0.00
y-coma	0.22
spherical	-0.02

### 4.3.1 Principle, Setup, Data Collection and Analysis

This experiment is, in essence, no more difficult than making one tilt measurement for the calibration process. With the CD cover aberrating the beam the data was collected using Snap30 and the mini-Wavescope in the same manner as each tilt value in the calibration. The average values of the coefficients of the first few Zernike modes are given in table 4.3

The data analysis for this experiment involved many steps beyond those of the calibration process. It was chosen to carry out a point by point comparison of the mini-Wavescope and the PS measurements of the CD Cover aberrated wavefront. This means comparing the local tilt measured at each subaperture over the pupil in the mini-Wavescope to the corresponding position in the PS pupil. The full transformation (rotation, translation, and scaling) from the coordinates used by the mini-Wavescope to the DALSA CCD was required.

The specific transformation is quite uninformative because it depends on the details of the lab setup, however the data taken to characterize it will be described. The centre of the coordinate systems for both sensors were set at the middle of the pupil by stopping down the iris to its smallest possible size, recording the images with the Pulnix (mini-Wavescope CCD) and DALSA CCD's. The rotation angle between the mini-Wavescope lenslets and the PS CCD was measured by blocking the iris

with a piece of paper on a slant and recording the images on both CCD's. The scaling was worked out by measuring the size of the pupil on both cameras. An extra complication was introduced into this process as the mini-Wavescope software does not permit raw frames to be saved. Images from the mini-Wavescope camera were acquired by running the `LiveDisplay` program used by the mini-Wavescope and capturing the images in a screenshot using another program called `SnagIt32`. The additional complication of another transformation was introduced because the format of the Pulnix CCD is 752x582 while `SnagIt32` saved the images at 640x480.

With the transformation worked out, the mini-Wavescope subapertures map to the PS pupil and the intensity observed on the PS camera could be integrated over each subaperture and converted to a tilt using the calibration results.

The next step is unique to this experiment and this particular implementation of the PS. With a 2d pyramid sensor, totaling the intensity in all four pupils gives a measure of the total intensity. Totaling the intensity in pairs of adjacent pupils and comparing to that of the opposite pupils gives a measure of the tilt. For the 1d PS, with only one pupil recorded, an overall decrease of the light intensity is interpreted as a tilt. This becomes an issue where the overall light intensity is attenuated, as is the case with the CD cover. However, this is not a uniform attenuation and it must be corrected subaperture by subaperture. Images were recorded using the Pulnix CCD/`SnagIt32` with and without the CD cover and the transformations mentioned above were used to map the attenuation factor to the appropriate area of the pupil on the PS.

The last addition to the analysis of the data for this experiment was to use the calibration curve calculated for each subaperture to account for the non-uniform sensitivity of the PS. This is the effect that is discussed in section 4.2.4.

### 4.3.2 Results

Figure 4.12 shows the tilts measured by both the mini-Wavescope (right) and PS (left). There is no striking correspondence between the two, although some of the

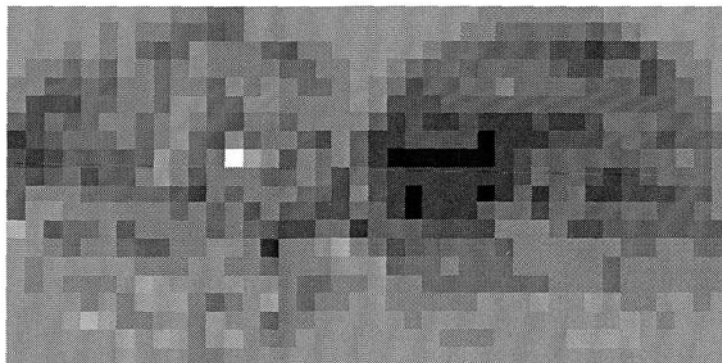


Figure 4.12: Wavefront tilt measured with PS and mini-Wavescope.

gross features of the tilts do agree.

Figure 4.13 shows the comparison quantitatively. If the mini-Wavescope and PS were measuring the same value for the local tilt at each position in the pupil, then a plot of the tilts measured with one against the other would have a slope of one and pass through the origin. There is quite a lot of scatter in the data, but despite that the slope of the bisecting line is 0.91, indicating that on average a larger PS measurement is indicative of a larger mini-Wavescope measurement. The y-intercept of the line is 0.070. This indicates that there is a static off-set between the two sensors and one possible cause for this is that the attempt to calibrate out the attenuation caused by the CD cover was unsuccessful.

Figure 4.14 shows the measurements plotted subaperture by subaperture. It is clear that the PS systematically overestimates the local tilt. Propagation of error calculations have been performed for the local PS tilt taking into account the error in the correction factor for the attenuation of the intensity by the CD cover, the PS intensity measurements of the aberration, the PS measurements at zero tilt, and the error in the calibration constants. The error in the intensity measurements is negligible. For the majority of subapertures the largest source of error is the correction factor. The

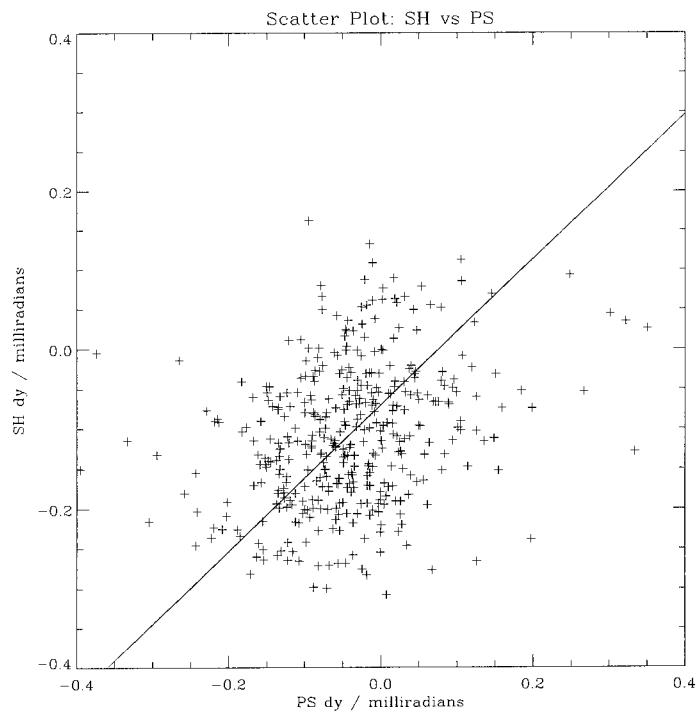


Figure 4.13: **Scatter Plot of Tilt Measurements:** This plot shows the local tilt measurements for the PS (with the  $0.5^\circ$  diffuser) plotted against the corresponding measurement made by the mini-Wavescope. Ideally the data should lie near a straight line with a slope of one. The line shown is has a slope of 0.91 and an intercept of 0.07.

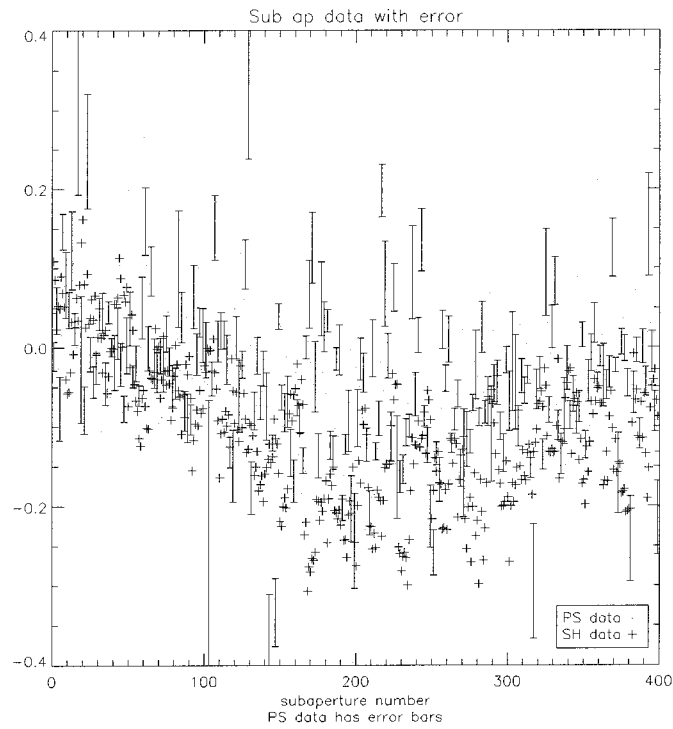


Figure 4.14: **Tilt Measurements, subaperture by subaperture:** The tilt measurements made with both sensors are shown plotted against subaperture number. Error bars are included at every second point on the PS measurements. Again the  $0.5^\circ$  diffuser has been used.

correction factor was calculated using

$$c_j = \frac{\sum_{S_j} \Delta x^2 I_{CD}}{\sum_{S_j} \Delta x^2 I_0} \quad (4.3)$$

where  $I_{CD}$  is the intensity measured with the CD cover in the beam path and  $I_0$  is the intensity measured without the CD cover. The integrals are carried out over the area of subaperture  $j$ . The uncertainty in  $c_j$  was estimated using its standard deviation over the subaperture. The second largest source of error was the error in the calibration constants, but this was for a small minority of subapertures.

An alternate method for calibrating the attenuation is needed. The first improvement would be to use measurements made with the PS CCD and not the Pulnix. This would eliminate the possibility of non-common path errors. The beam could be passed through one side of the prism enabling the full pupil to be seen, and images could then be captured with and without the CD cover. The attenuation could be accounted for directly on the PS images, and this would avoid using any of the transformation from CCD to CCD facilitating the calculation and eliminating another source of potential error.

This raises the point of the transformation as sources of error. It was assumed that the contribution of the measured transformation to the error would be negligible. This effect was not studied and it is possible that they contribute significantly to the error in the local tilts, but unlikely.

Another potential source of error that was directly taken into account in the propagation of error was the effect of the subaperture size. As mentioned above the size of the subaperture on the PS is limited by the blur introduced by its optics. For this experiment many of the mini-Wavescope subapertures mapped to 4x4 or 5x5 pixel regions on the PS CCD. This is at the limit of the rule of thumb for subaperture size, and is the likely source of error.

Although it may have improved the results of the CD Cover experiment, the alternate approach to the attenuation factor was not attempted due to time considerations. It requires that the diffuser be removed from the setup, and hence new calibration

measurements would be required before another set of data on the static aberration could be collected. Measuring turbulence was given a higher priority. At this point, the data could be re-analyzed in a similar manner to that of the following section, via a Zernike decomposition, for comparison with the Zernike coefficients calculated by the mini-Wavescope.

## 4.4 Dynamic Characterization of the PS

In general, it would not be considered feasible or ideal to characterize a new type, or prototype of a wavefront sensor with actual turbulence. The more intuitive approach in calibrating any new instrument is to use a set of standards of known properties and measure the response to the standards. In the case of wavefront sensors this is in fact what is done. The PYRAMIR project being developed at MPIA has incorporated an OKO DM into the bench setup to allow the prototype pyramid sensor to see and measure Zernike modes (Costa et al., 2003a; Costa et al., 2004a). An OKO DM was also used in this way in previous studies of the PS in the laboratory (Esposito et al., 2000a). This type of calibration is exactly what is done each time a new interaction matrix is generated for an AO system using modal control.

However, what we have in the lab is a source of turbulent wavefronts, and although we cannot use the turbulator to select specific wavefront shape, the wavefronts produced by the turbulator must obey the laws associated with atmospheric turbulence. Hence, the wavefronts produced in the turbulator will show temporal and spatial behaviour which is consistent with the Kolmogorov, or a modified Kolmogorov, model (Tatarskii, 1971). Using measurements of the turbulent wavefront with two wavefront sensors, the PS and a reference wavefront sensor (the mini-Wavescope) the spatial (Fried parameter, inner and outer scale) and temporal (high and low frequency slope and knee frequency) parameters of the turbulence are measured and compared between the two sensors. The key assumption being that if the two wavefront sensors are measuring the same statistical properties of the turbulence then we can be assured that the individual measurements of each wavefront yield nearly the same information.

#### 4.4.1 Principle of characterization of real turbulence

The interpretation of the results of the measurements of the wavefronts generated by the turbulator relies heavily on the Zernike representation of the power spectrum of the incoming turbulent phase (Noll, 1976). To motivate the changes made to Noll's results in order to include the effects of the inner and outer scale, it is interesting to look at the various versions of the spatial power spectrum of the turbulent phase.

The basic power spectrum of the turbulence distorted phase is the Kolmogorov Spectrum which, as a function of magnitude of the spatial frequency vector,  $f$ , is given by

$$W_K(f) = \frac{0.023}{r_0^{5/3}} f^{-11/3}. \quad (4.4)$$

It can be modified to include two other important physical properties of the turbulence: those of the inner and outer scale. The inner and outer scale bound the inertial range of the turbulent flow (ie. the size scales over which the viscosity of the fluid is negligible and no energy is dissipated). The Kolmogorov Spectrum is a model of a turbulent flow which has an infinite inertial range, i.e.,  $L_0 \rightarrow \infty$  and  $l_0 \rightarrow 0$ . The outer scale parametrizes the largest size scales over which the turbulence is correlated and the inner scale parametrizes the size of the eddies in the fluid at which the kinetic energy of the flow is converted to heat. A finite outer scale and an inner scale that is greater than zero causes the power spectrum at low and high spatial frequency to be damped compared to the Kolmogorov spectrum. The outer scale is of interest because of its relevance to the design of AO systems for ELT's, the apertures of which are approximately equal to or greater than the outer scale (typically 20-30 m) because it decreases the amount of low order, high stroke aberration the AO system must correct (Conan et al., 2002). In the laboratory the inner scale will play an important role because it will be on the same size scale as the beam, typically 2-12 mm, and serves as a fundamental limit to the amount of high spatial frequency aberration in the laboratory simulations of real AO systems (Jolissaint, 2000).

The damping effects of the inner and outer scale can be added to the power spectrum of the turbulent phase *ad hoc*, effectively transforming the theoretical result, the

Kolmogorov Spectrum, into an empirical fitting function. The von Karman Spectrum is one such function and includes only the effect of the outer scale. It is given by

$$W_{vK}(f) = \frac{0.023}{r_0^{5/3}} \left( f^2 + \frac{1}{L_0^2} \right)^{-11/6}. \quad (4.5)$$

The effect of the inner scale can simply be added to the von Karman Spectrum as a Gaussian damping factor giving a damped von Karman Spectrum

$$W_{d-vK}(f) = \frac{0.023}{r_0^{5/3}} \left( f^2 + \frac{1}{L_0^2} \right)^{-11/6} \exp(-(l_0 f)^2). \quad (4.6)$$

The more sophisticated Hill-Andrews model, which is given by

$$W_{HA} = \frac{0.023}{r_0^{5/3}} \left( f^2 + \frac{1}{L_0^2} \right)^{-11/6} (1 + 3.43 f l_0 + 0.538 (f l_0)^{7/6}) \exp(-3.625 (f l_0)^2) \quad (4.7)$$

contains both the Gaussian damping factor and a polynomial factor to better mimic the the effect of the inner scale (Andrews, L. C., 1992; Innocenti, C. and Consortini, A., 2004). The bottom line is that the damping effects are inserted into the Kolmogorov Spectrum, and, for the inner scale, it is simply a factor (of a particular functional form) which attenuates the high spatial frequency regime of a power spectrum which already takes into account the outer scale.

The representation of the Kolmogorov model in terms of Zernike coefficients is a well known result (Noll, 1976). It rests on the Zernike-Kolmogorov Covariance Matrix shown in Table 4.4. Each element in the matrix is calculated directly from the definition of covariance

$$\langle a_j^* a_{j'} \rangle = \int \int d^2 \mathbf{f} d^2 \mathbf{f}' Q_j^*(\mathbf{f}) W_K(f) \delta(\mathbf{f} - \mathbf{f}') Q_{j'}(\mathbf{f}) \quad (4.8)$$

where the  $Q$ 's represent the Fourier transforms of the Zernike polynomials and the  $a$ 's refer to the coefficients of a Zernike expansion of the incoming turbulent phase,  $\phi$ , such as

$$\phi(\mathbf{r}) = \sum_j a_j Z_j(\mathbf{r}). \quad (4.9)$$



This formalism for calculating the matrix elements is given in Noll, 1976. The terms on the diagonal of the covariance matrix are the variances of the coefficients of the Zernike expansion of the turbulent phase. The effects of outer scale damping on the entire Zernike–Kolmogorov Covariance Matrix have been rigorously calculated (Winker, 1991). The effect of the inner scale on the variance of the Zernike coefficients can be included in an analogous manner to the damped von Karmann and the Hill–Andrews model above. This is accomplished by multiplying each diagonal element of the covariance matrix by two attenuation factors, one for the outer and one for the inner scale. So the variance of the  $j^{\text{th}}$  coefficient of the Zernike expansion, including the effects of the inner and outer scale, become

$$\left\langle \left| a_j^{L_0, l_0} \right|^2 \right\rangle = c_{\text{atten}}(L_0; j) c_{\text{atten}}(l_0; j) \langle |a_j|^2 \rangle \quad (4.10)$$

L. Jolissaint has developed an IDL function called `attos.pro` as part of the OPERA tool-pack which generates the coefficients  $c_{\text{atten}}(L_0; j)$  according to the calculation of Winker, 1991 (Jolissaint et al., 2004c). Another IDL program `attis.pro` has been written to calculate the coefficients  $c_{\text{atten}}(l_0; j)$ . The calculation leading to this is outlined next.

A Zernike polynomial is associated with a full spectrum of spatial frequencies which are given by the Fourier transforms,  $Q_j$  used in equation 4.8. To approximate the typical spatial frequency associated with a particular Zernike mode of radial order,  $n$ , the ‘cut-off’ frequency of  $Q_j$  can be used. Under this approximation, the spatial frequency for a radial order,  $n$ , is

$$f(n) = \frac{0.23(n+1)}{D} \quad (4.11)$$

where  $D$  is the diameter of the aperture. (Conan, 1980) Taking the Gaussian damping factor and polynomial term from equation 4.7

$$g_{\text{damp}}(f) = (1 + 3.43fl_0 + 0.538(fl_0)^{7/6}) \exp(-3.625(fl_0)^2), \quad (4.12)$$

and inserting equation 4.11 we obtain the inner scale attenuation factor for a partic-

ular Zernike order  $j$ . It is given by

$$c_{atten}(l_0) = g_{damp}(0.23(n(j) + 1)/D). \quad (4.13)$$

Thus, a complete fitting tool is available to provide the important physical parameters of the turbulence,  $r_0$ ,  $L_0$ , and  $l_0$ , if the coefficients of the Zernike expansion of the turbulent wavefront can be measured for a statistically significant sample of wavefronts from the turbulator.

Using the above results the data from the mini-Wavescope can be analyzed. The mini-Wavescope software is capable of returning up to 42 Zernike coefficients for each individual wavefront measurement. Its accompanying software package uses the measured slopes in the x and y directions to reconstruct the wavefront. It should be noted that the Zernike coefficients which are returned are ordered according to the convention used by Zygo, which differs from that of Noll. This means that there are incomplete radial orders, which will become obvious in the plots to follow.

The PS reduction is quite different, and the results of Noll, modified to include the effects of  $l_0$  and  $L_0$ , require further manipulation before they can be used to analyze the PS data. Using a prism, the PS is sensitive to only the wavefront slope in the direction perpendicular to the apex of the prism (the y direction). This presents two avenues for comparison with the theory presented above. One could reconstruct the wavefront using only y slopes, calculate variances of the expansion coefficients, and compare directly. Alternatively, the Zernike coefficients of an expansion of the y *slope* of the phase could be calculated. It is possible to calculate their counterparts from the theoretical Noll variances for comparison. The second option will be discussed first. The conversion of the variances of the Zernike expansion of the phase to those of the slope of the phase relies on the fact that the Zernike polynomials constitute a basis set and, as such, it is possible to express any arbitrary function, including the gradient of each Zernike polynomial, as a linear combination of Zernike polynomials. Thus, if the wavefront is given by equation 4.9 above, then the slope of the wavefront



is given by

$$\nabla\phi = \sum_{j'} \left( \sum_j a_j \gamma_{jj'} \right) Z_{j'} \quad (4.14)$$

where  $\gamma_{jj'}$  are the coefficients of the Zernike expansion of the derivative of the  $j^{\text{th}}$  Zernike. The matrix  $\gamma$  is called the Zernike Derivative Matrix and it is given in Noll, 1976. It is presented here as table 4.5.<sup>2</sup> Upon proceeding to calculate the variance of the derivative coefficients in terms of the wavefront coefficients and the  $\gamma_{jj'}$ , it becomes obvious that off diagonal terms of the covariance matrix are required. In principle this is not a problem because each element of the covariance matrix can be calculated and attenuated by outer scale damping according to the method presented in Winker, 1991. The inner scale is a different matter, as to the author's knowledge, a rigorous calculation of its attenuation of the entire Zernike–Kolmogorov Covariance Matrix has never been attempted. However, the off diagonal terms are usually smaller than the diagonal terms and we will assume that they can be neglected. With this assumption the variance of the coefficient of the Zernike expansion of the wavefront derivative becomes

$$\langle |a_{j'}^d|^2 \rangle = \sum_{jj'} \langle |a_j|^2 \rangle \gamma_{jj'}^2. \quad (4.15)$$

This can also be written in terms of a matrix multiplication

$$\mathbf{A}^d(L_0, l_0) = \gamma^2 \mathbf{A}(L_0, l_0) \quad (4.16)$$

where  $\mathbf{A}^d$  is the column vector of variances of derivative coefficients and  $\mathbf{A}$  is the column vector of wavefront variances. The matrices involved are not square as the derivative series will always be restricted to fewer terms than the original wavefront. Assuming that the wavefront series has  $j$  terms in total and contains all terms of radial order  $n$ , the derivative series will contain  $j - (n + 1)$  terms.

With the additional matrix multiplication to convert from wavefront to derivative, variances of the Zernike coefficients of expansion of the wavefront derivative can be

<sup>2</sup>Attempting to program the rules Noll states in his 1976 paper in order to generate table 4.5 will not be successful. The matrix presented is correct, however, the rules as stated are not. The condition in rule b must be changed such that the matrix element is zero unless  $m$  is odd and  $j'$  is even or  $m$  is even and  $j$  is odd. Of course the matrix elements are all zero for  $n > n'$ .

generated from the diagonal of the Zernike–Kolmogorov covariance matrix allowing the PS data to yield the parameters of the turbulence *without actually reconstructing any wavefronts*.

The other option mentioned above has also been attempted with some success. It is typical in AO systems to reconstruct the wavefront from the wavefront sensor signals using a Singular Value Decomposition (SVD) (Tyson, 1998). The SVD is required because the problem is over-determined:  $n$  commands to the DM's actuators must be calculated from  $2n$  slopes ( $x$  and  $y$ ) measured by the wavefront sensor. The SVD is equivalent to the least-squares solution for the wavefront given the information at hand. In the case of the 1d PS, the  $y$  slope at each of  $n$  subapertures is measured. This can be used to generate a Zernike series for the wavefront derivative with up to  $n$  terms. SVD can be used to calculate the pseudo inverse of  $\gamma$  which relates a Zernike expansion to its derivative. When the pseudo inverse of  $\gamma$  is applied to the slope expansion series, a series representing the the least squares solution for the wavefront is generated. This series can be used to calculate variances to compare with the models above without the need for equation 4.16. However, as mentioned above, the slope series will always have less terms than the corresponding wavefront series and so the problem is not over-determined, but under-determined. Thus the series coefficients for the wavefront must be extrapolated and this has the potential to impact the calculated variances in a systematic way. The method outlined first does not suffer from this particular complication. Additionally, SVD can be used to solve equation 4.16 for  $\mathbf{A}(L_0, l_0)$

#### 4.4.2 Laboratory Setup and Data Collection

The actual bench setup is shown in figure 4.15 and a schematic is shown in figure 4.16 for clarity. To include the turbulator in the bench setup, the optical layout was modified from that used for calibration. The fold mirror used to tilt the beam was removed and the fiber source was repositioned at the opposite end of the large optics table from the DALSA CCD camera used for the PS. The turbulator was placed between the collimating lens of the fiber source and the iris, which remains the stop

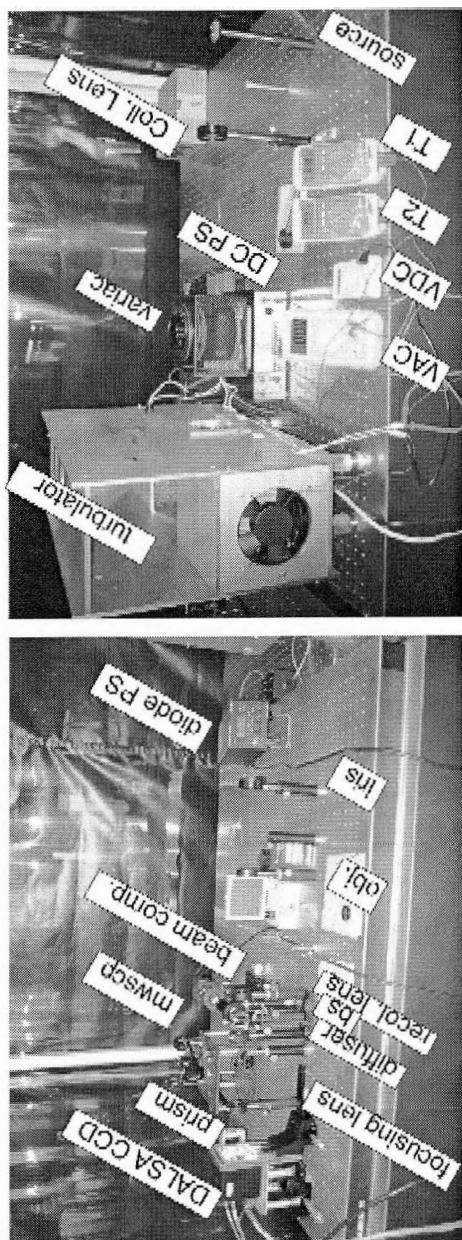


Figure 4.15: **Photograph of Bench Setup:** The optical bench setup is shown in these two photographs taken side-by-side from inside the optics tent in the UVIC AO lab. On the far right labeled 'source' is the (one) output of the pigtailed laser fiber. Moving left across the image there is the collimating lens and the turbulence generator itself, shown in the vertical orientation used in the collection of data set 2. (See Table B.2 below.) The variac used to power the heater in the hot-air channel of the turbulence generator as well as the variable 12V DC power supply used to power both of the turbulator's fans are in the background. In the foreground are the DMM's responsible for measuring fan speed (VDC), variac setting (VAC), and the hot (T1) and cool (T2) air temperatures. In the next image, the iris, objective lens, re-collimating lens, and beam-splitter (bs) are shown. After the beam-splitter one arm of the beam goes to the PS (passes through the diffuser and is then re-focused onto the prism), and the other arm of the beam is re-sized by the beam-compressing optics and sent to the reference wavefront sensor, the mini-Wavescope (mwscp).

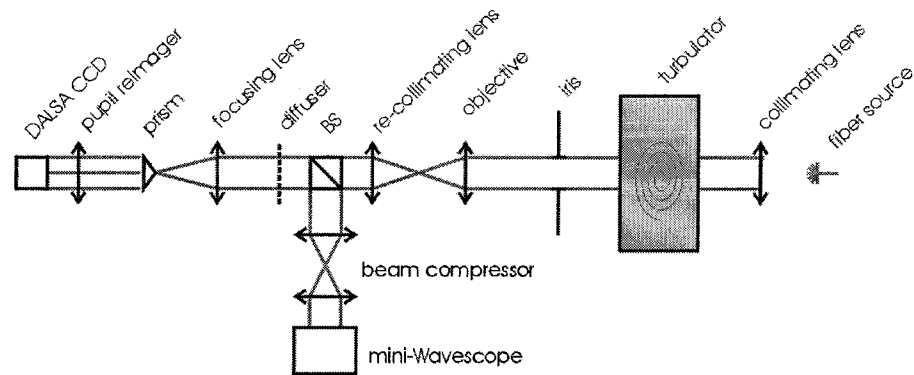


Figure 4.16: **Schematic of Bench Setup:** This diagram shows schematically the bench setup in figure 4.15. The pupil re-imaging lens in the PS, which is not visible in the photograph, is shown after the prism.

of the system. The exact placement of the turbulator between the lens and the iris as well as the conjugation of both WFS's to the plane of the stop is not crucial for this experiment because statistical properties of the turbulence are measured. If the two WFS's are not conjugated to the same plane, at any given frame they will measure a different phase as the light propagates from the conjugate plane of the mini-Wavescope's lenslet array to the conjugate plane of the CCD detector of the PS. However, the variance of the coefficient of the Zernike expansion will be the same for a large number of frames as this is independent of where the wavefront is measured.

The measurements using the PS were again made using software developed at the UVIC AO lab by A. Hilton and B. Wallace. The program, called Snap5000, runs under QNX and acquires and saves 5000 consecutive frames from the DALSA CCD as fast as possible. The average speed of acquisition is consistently 522 Hz. Most of the frames are acquired at 500 Hz and a minority at 667 Hz. This is due to the timing of the requests to the BitFlow Roadrunner framegrabber. In the data

analysis the average frame rate has been used in generating the temporal power spectra, as was previously done in calculating the temporal properties of the turbulence (Keskin et al., 2003).

The mini-Wavescope measurements had to be made in sets of 150 or 200 frames due to the limited RAM and disk space of the mini-Wavescope's control computer. As mentioned above the miniWavescope's software package, which is written on top of the tcl/tk scripting language, requires the user to create a test. For this experiment a test called `turb_zern` was created the sole function of which was to calculate and save the Zernike coefficients of a set of frames. To save the wavefront derivative and Zernike coefficient data in an ASCII file that was easily portable from Windows to IDL running under Red Hat Linux, a tcl script using the atomic functions of the mini-Wavescope software package was written. The possibility of user written scripts to manipulate data is one of the strengths of the mini-Wavescope and makes it a very powerful laboratory tool.

Summarizing, the data collection process consisted of the following steps: (1) a set of frames was collected at the full frame rate of the miniWavescope's Pulnix TM-7 CCD camera ( $\sim 5$  s), (2) the miniWavescope computer calculated and saved the Zernike coefficients of each frame ( $\sim 5$  min), and (3) the tcl script was run to convert the data to files for import into IDL. This process was repeated 8 to 10 times depending on the size of the set of frames, so the collection of the miniWavescope data for each set of parameters of the turbulator required  $\sim 1$  hour. This extended time period for data collection (compared to the  $\sim 10$  s required for the PS) has implications for the data analysis and interpretation of the temporal power spectra measured with the mini-Wavescope. This will be discussed in the following section.

There are data from two sets of experiments which will be referred to as data set 1 and 2. The details of data set 1 are given in table B.1. This data set was collected with the turbulator in its horizontal position, as it has been used in the past (Keskin et al., 2003). Data set 2, detailed in table B.2, was collected with the turbulator in a vertical configuration, as shown in figure 4.15. Having the turbulator in the vertical orientation allows the beam to pass through its shortest dimension. Although the temporal and spatial properties of the turbulence measured with both

sensors will be the focus of the discussion to follow, the comparison of the two orientations of the turbulator will be discussed in section 4.6.

### 4.4.3 Data Analysis and Results

#### Temporal Characterization

The temporal properties of wavefronts produced by hot-air turbulence generators have been studied previously (Jolissaint, 2000; Keskin et al., 2003). The expected behaviour for one layer of turbulence following a Kolmogorov spectrum is a temporal power spectrum of the tilt mode that has a slope of  $-\frac{2}{3}$  at low temporal frequency and a slope of  $-\frac{11}{3}$  at high temporal frequency. The frequency at which the two regimes meet will be referred to as the ‘knee’ frequency. The knee frequency is a useful gauge of the effective wind speed of the turbulence as these quantities are related by

$$f_{knee} \approx 0.3 \frac{v_{eff}}{D} \quad (4.17)$$

where  $D$  is the diameter of the entrance pupil. The wind speed is denoted as effective to emphasize the fact that there is not only one layer of turbulent air inside the turbulence generator, but rather a continuum of layers mixing with varying velocities. Thus, the transition between the low temporal frequency and high temporal frequency regimes will never be sharp but will be a gradual turnover from a relatively shallow to a steeper slope.

To calculate the temporal power spectrum of the tilt, a time series of tilt measurements is needed. For the PS this is accomplished in the same manner as the tilt measurements for the calibration procedure described above. Using an IDL procedure the frames collected from the CCD are read in, a bias frame is subtracted from each one, and the intensity is integrated over the pupil image. The intensity at the home position (ie. turbulator turned off) is subtracted and the resulting difference is then divided by the home position intensity to get the fractional change in intensity. The fractional change is then converted to a tilt using the calibration constant

for the  $0.5^\circ$  diffuser from section 4.2.3. The task of generating the time series is already accomplished for the miniWavescope because the coefficient of the tilt mode is recorded.

It should be noted that the local tilts over each subaperture of the SH WFS *cannot* be used to get a temporal power spectrum that can be compared with the PS data. This may seem like an attractive idea because the mini-Wavescope has a large number ( $\sim 300$ ) of active subapertures, and there seems to be potential to reduce the measurement noise by calculating a power spectrum for each subaperture and then averaging. The reason is that the size of the aperture is not the same. Just as with the aliasing of high spatial frequency aberrations onto lower spatial frequencies below the cut-off frequency of the aperture, there is a low spatial frequency cut-off below which all spatial frequencies are seen as contributing to the global tilt term. Thus, the coefficient of tilt for the entire aperture must be used as this low spatial frequency cut-off is related to the aperture size (Vérinaud, 2004) <sup>3</sup>

$$f_c \approx \frac{0.7}{D}. \quad (4.18)$$

With the time series of tilts obtained for both sensors there are two ways to proceed to calculate the temporal power spectra. The spectra can be calculated directly by taking the Fourier Transform of the time series,

$$W_{tilt} = |\mathcal{F}[a_2(t)]|^2 \quad (4.19)$$

and then the results may be binned in frequency to reduce the noise. This is the avenue taken in previous work (Keskin et al., 2003). However, due to the smaller data sets in this experiment, 10000 samples in Keskin, 2003 compared with 150 for the mini-Wavescope data, this method gives unsatisfying results. The alternate procedure is to calculate the power spectra by first calculating the autocorrelation,

---

<sup>3</sup>This is an issue that must also be dealt with when calculating the wavefront error variances due to different sources in analytical models of AO systems like PAOLA. In section 2.3.1  $\frac{1}{D}$  has been used to account for this.

$R$ , of the time series of tilts and then taking its Fourier transform to obtain,

$$W_{tilt} = \mathcal{F}[R_{a_2}] \quad (4.20)$$

as the power spectrum and auto-correlation are Fourier transform pairs (Wiener-Khinchin theorem) (Bracewell, 1978). The auto-correlation is effectively the convolution of the time series with itself

$$R_{a_2} = \int_{-\infty}^{\infty} a_2(t)a_2(t + \tau)d\tau \quad (4.21)$$

and as a result this process has the benefit of smoothing the data before taking the Fourier transform which significantly reduces the scatter of the resulting power spectra. The drawback is that details in the temporal power spectrum will be smoothed and this may make the knee frequency more difficult to identify. However, since we are interested in measuring the high and low frequency slope to compare with the  $-\frac{2}{3}$  and  $-\frac{11}{3}$  laws mentioned above it is acceptable to sacrifice the details in favour of the gross behaviour. Figure 4.17 shows an example of the same power spectrum calculated with both equation 4.19 and equation 4.20, and it is clear from the plot that the scatter in the data points is appreciably reduced using the second method.

Furthermore, as mentioned previously, the data collected with the mini-Wavescope was obtained in sets of 150-200 frames. This leads to two approaches for the data analysis: each set is appended to the previous one to generate a longer time series, or the auto-correlation (or a power spectrum) is calculated from each set and the results averaged. The first procedure relies on the assumption that given a certain set of parameters, ie. variac setting and fan speed, the turbulator produces the same conditions inside the box over time. While this is likely the case (to first order), the temporal power spectra for the mini-Wavescope have been generated via an average.

Temporal power spectra were calculated for each of the runs in both data sets. A piecewise linear function was fit to the natural logarithm of the data. This fit to the data was calculated using an IDL script running the ‘MPFIT’  $\chi^2$  minimization routine. MPFIT is a set of IDL routines based on public domain code (Markwardt,

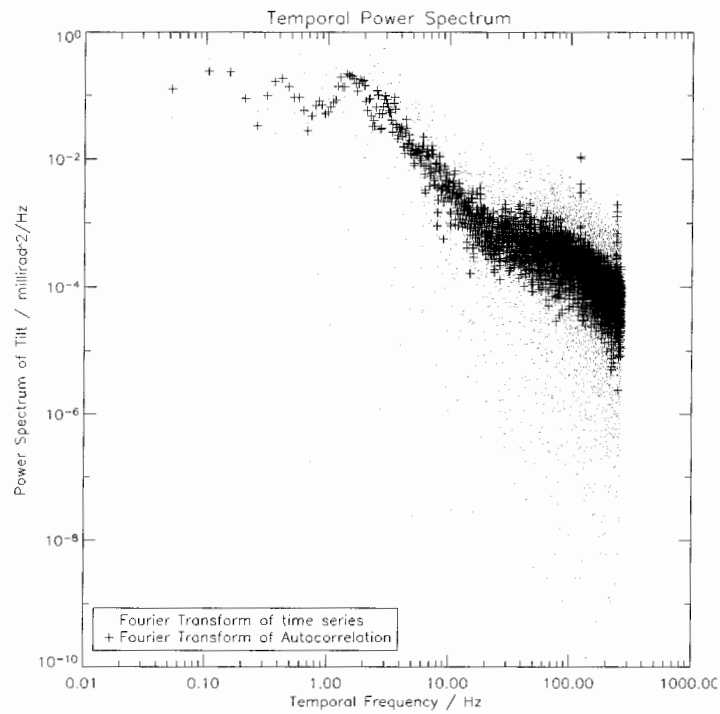


Figure 4.17: **Direct Fourier Transform vs Auto-Correlation:** This plot compares the temporal power spectra calculated using the two methods outlined in the text. The auto-correlation calculation clearly reduces the scatter in the data points.

Table 4.6: **Temporal Power Spectrum:** This table summarizes the results of the temporal power spectrum calculation for the run  $\Delta T = 140$  from data set 1 collected with the mini-Wavescope. The first row of parameters are the high and low frequency slopes and the knee frequency of the fit shown in 4.18 and represent the average temporal power spectrum at this temperature difference and fan speed. The rest of the data in the table are the same parameters for each individual subset of the data. The variability of the parameters from one subset to the next, a difference of  $\sim 5$  min can be attributed to the statistical nature of turbulence, or changing conditions within the turbulator.

Data Set 1 mini-Wavescope run: $\Delta T = 140$							
Average							
$f_{knee}$ (Hz)	error (Hz)	low-frequency slope	error	high-frequency slope	error	$\chi^2$	$\delta_y$
6	2	-0.9	0.3	-2.5	0.8	3.1	0.1
Individual runs							
7	2	-0.9	0.3	-2.9	0.9	24.3	0.4
11	2	-1.1	0.2	-7	4	31.9	0.4
4	4	-1.1	0.5	-1.7	0.4	21.5	0.3
4	3	-0.9	0.4	-1.7	0.5	51.3	0.5
4	1	-0.5	0.4	-2.3	0.5	43.8	0.5
5	2	-0.5	0.3	-2.3	0.7	34.7	0.4
9	2	-1.2	0.2	-4	2	35.6	0.4
8	3	-1.2	0.3	-3	1	44.6	0.5
7	2	-1.2	0.3	-4	1	15.3	0.3
3	1	-0.2	0.6	-2.0	0.4	38.9	0.5

2004). The fits to the PS data were restricted to a frequency domain of 0 to 15 Hz for comparison with the mini-Wavescope. As a check on the stability of the conditions inside the turbulator fits were also carried out on each set of mini-Wavescope data. Table 4.6 shows an example of this calculation.

Figure 4.18 shows the temporal power spectra from run  $\Delta T = 140$  in data set 1 calculated using the data from both the mini-Wavescope and the PS. The low frequency slope in figure 4.18 is  $-0.9 \pm 0.3$  for the mini-Wavescope and  $-0.8 \pm 0.2$  for the PS while the high frequency slope is  $-2.5 \pm 0.8$  for the mini-Wavescope and  $-2.8 \pm 0.4$  for the PS spectrum. Both slopes agree within one sigma. The low frequency slopes agree with the expected  $-\frac{2}{3}$ ; however, the high frequency slopes are systematically greater than expected. The knee frequency also agrees within one sigma:  $6 \pm 2$  Hz for the mini-Wavescope and  $5 \pm 1$  Hz. Interestingly, this value is lower than that reported in Keskin et. al., 2003 and is a more suitable value for simulating atmospheric turbulence over an 8 m telescope aperture.

Figure 4.19 shows the same comparison for data set 2. In this case the low-frequency slope is  $-0.5 \pm 0.3$  and  $-0.4 \pm 0.2$  for the mini-Wavescope and PS respectively. The high frequency slope for the mini-Wavescope is  $-2.8 \pm 0.4$  and  $-2.3 \pm 0.1$  for the PS. Again both slopes agree to one sigma and the high frequency slope is systematically less than the expected  $-\frac{11}{3}$ . For this data set the knee frequencies do not agree at  $\Delta T = 140$ :  $4 \pm 1$  Hz for the mini-Wavescope and  $2.2 \pm 0.4$  Hz for the PS.

Table C.2 shows the parameters of the temporal power spectra calculated for data set 1 and 2 from the mini-Wavescope data. Table C.3 shows the temporal power spectra parameters for data set 1 and 2 using the PS data. For data set 1, all of the calculated parameters agree to one sigma except for the low frequency slope of  $\Delta T = 40$ . For data set 2, the agreement between the two WFS's is not as good. The knee frequencies do not match for  $\frac{2}{3}$  of the temperature differences, and  $\frac{1}{3}$  of the slopes do not agree. The fit failed for temperature differences  $\Delta T = 5$  and  $\Delta T = 15$ . An interesting anomaly is  $\Delta T = 80$ . None of its temporal parameters agree between the two sensors, yet of all of the measurements it has the only high-frequency slope consistent with  $-\frac{11}{3}$ . The discrepancies between the two wavefront sensors must be accounted for in the different conditions between the two data sets and the differing

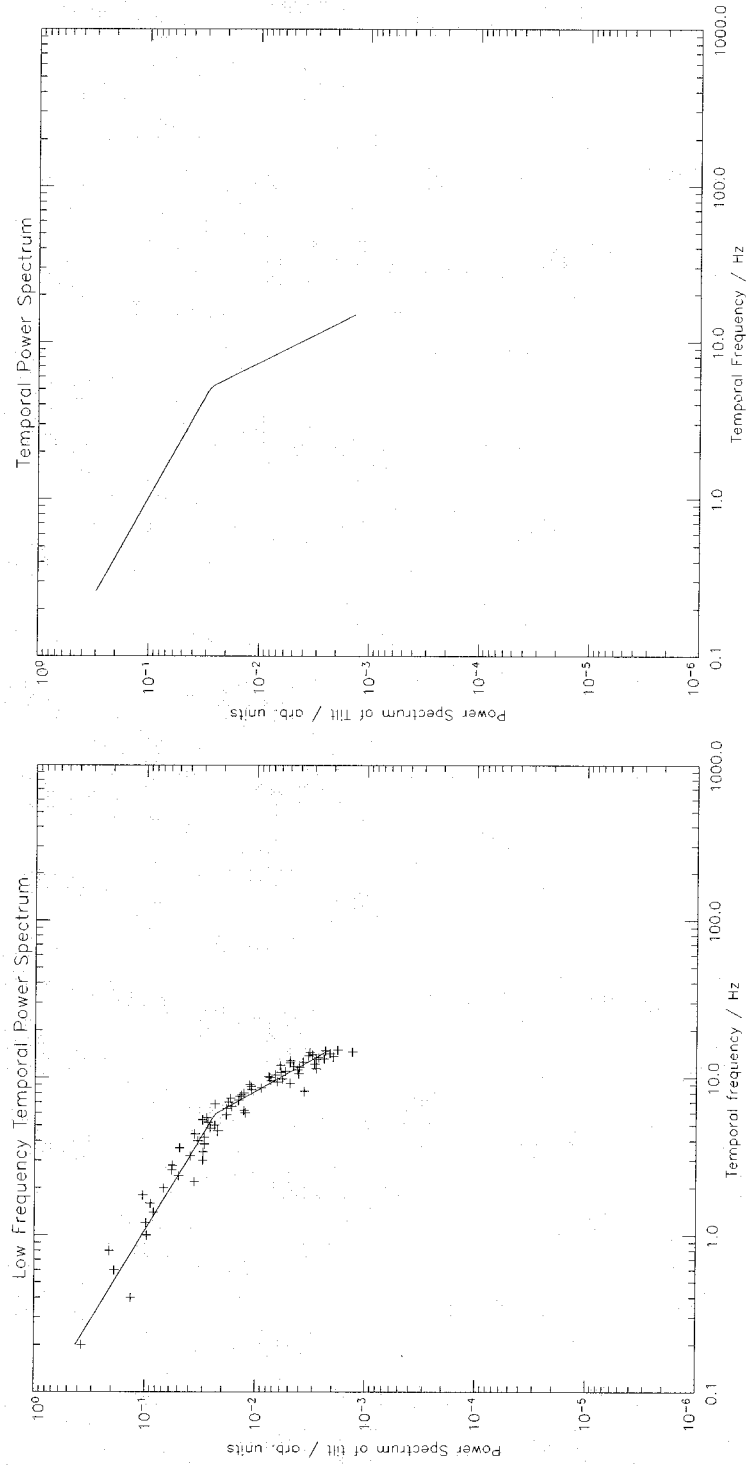


Figure 4.18: **Temporal Power Spectrum,  $\Delta T = 140$ , Data Set 1:** This plots show the temporal power spectra calculated from the mini-Wavescope data (left) and the PS data (right). The high and low frequency slope and the knee frequency for the mini-Wavescope are  $-2.5 \pm 0.8$ ,  $-0.9 \pm 0.3$ , and  $6 \pm 2$  Hz respectively. The same parameters for the PS are  $-2.8 \pm 0.4$ ,  $-0.8 \pm 0.2$ , and  $5 \pm 1$  Hz.

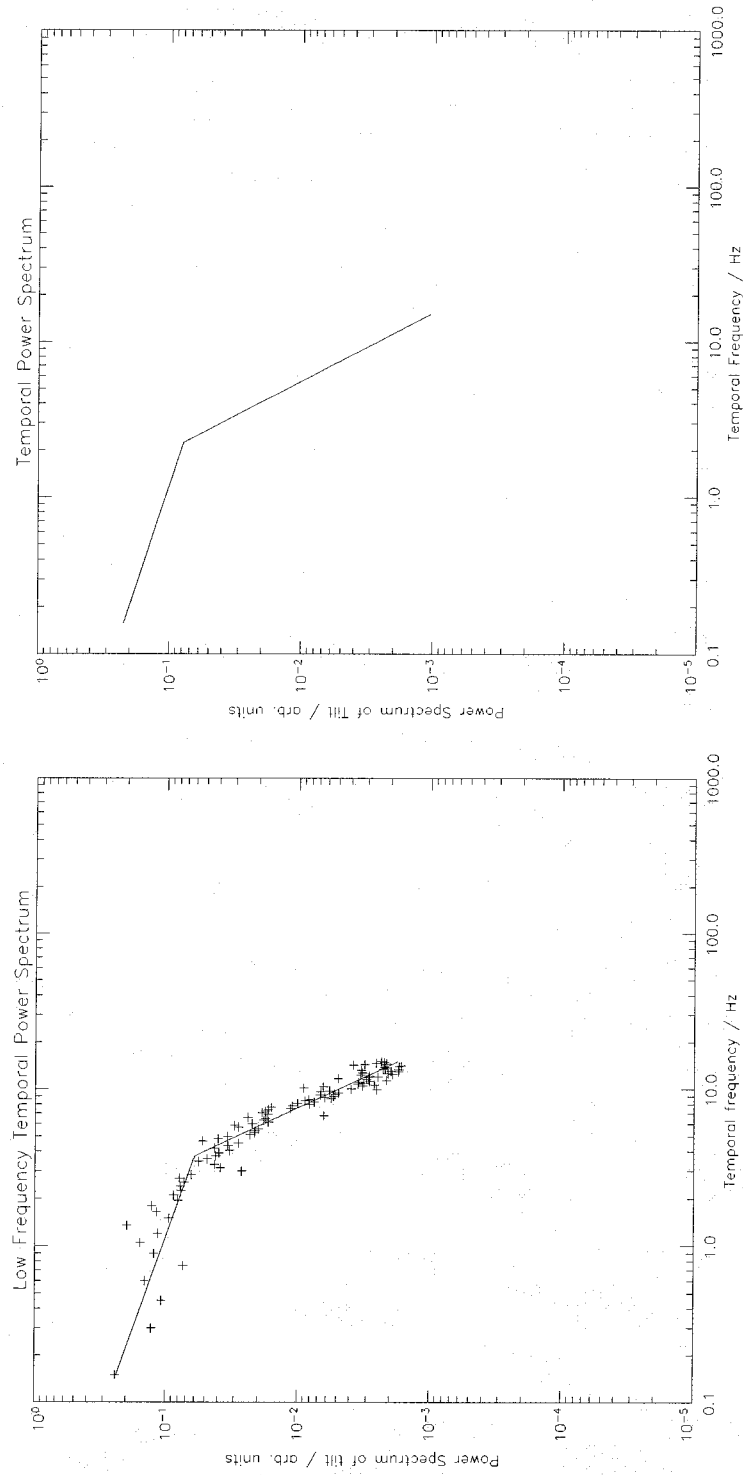


Figure 4.19: **Temporal Power Spectrum,  $\Delta T = 140$ , Data Set 2:** These plots show the same information as figure 4.18, but for data set 2. The high and low frequency slopes and knee frequency for the mini-Wavescope and PS respectively are:  $-2.8 \pm 0.4$ ,  $-0.5 \pm 0.3$ , and  $4 \pm 1$  Hz; and  $-2.3 \pm 0.1$ ,  $-0.4 \pm 0.2$ , and  $2.2 \pm 0.4$  Hz.

time scales of the two types of measurements. The only intentional change was the orientation of the turbulator. This may have had an effect on the time required for the turbulence inside the box to reach a steady state. In this case the average turbulence generated over a long period of time ( $\sim 1$  hr) measured by the mini-Wavescope, may differ from the turbulence measured by the PS ( $\sim 10$  s).

### Spatial Characterization

These experiments comprise the first direct measurements of the spatial properties of the turbulence produced by the turbulator. Previously the parameters characterizing the spatial properties of the turbulence have been extracted from a time series of tilt measurements using an Angle-of-Arrival Variance analysis (Keskin et al., 2003). As described above in section 4.4.1, the method used here relies on measuring Zernike expansions of the wavefront or its derivative and hence requires wavefront sensors capable of spatially resolving the wavefront over many subapertures (the total number of which depends on the desired number of Zernike coefficients).

The number of terms in the Zernike series for the data collected with the mini-Wavescope is limited by the software to 42, and for data set 1, only 20 coefficients were recorded. On the other hand, for the PS data a series may be generated with the number of coefficients equal to the number of subapertures. Each pixel of the PS CCD can, in principle, be used as a subaperture. There are many reasons why this is not a practical choice, the most important for this work being that the subapertures must correspond to a sufficiently large portion of the area on the diffuser through which the beam passes so that the calibration constant for each subaperture is reasonably close to the global one. See section 4.2.4. It is no more difficult to measure the local calibration constant for the diffuser; however, the restrictive aspect is that the diffuser cannot be moved, or the local calibration constants must be remeasured.

With this in mind, square subaperture grids of  $7 \times 7$  and  $14 \times 14$  were used for the PS data, meaning that a fully illuminated subaperture would contain 144 and 36 pixels respectively for the two configurations. It is important to point out that the subapertures do not have to be mapped between the sensors, as is the case when

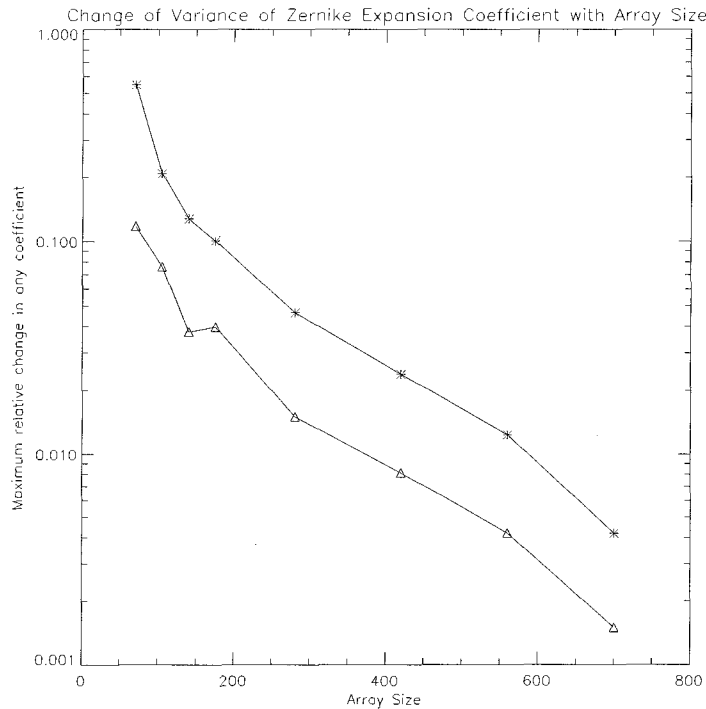


Figure 4.20: **Change in Variance of Zernike Coefficients with Array Size:** The variances of the Zernike coefficients were calculated for various sizes of the matrix representing the particular Zernike polynomial. The matrix size for the projections was chosen such that none of the coefficients changed by more than 1%.

attempting to verify the measurement of a static wavefront from point-to-point. This is due to the fact that we are interested in the statistical properties of the turbulence, ie. variance of coefficients, rather than the coefficients themselves.

With this choice of subaperture the data analysis proceeds in the following manner. The mini-Wavescope data already gives the Zernike coefficients and the only task is to rescale them. The raw PS frames collected with the QNX software mentioned above in section 4.4.2 were processed using an IDL script which read in the frames, performed bias subtraction, averaged over subapertures, converted from digital numbers to tilt/subaperture, and performed the necessary projection onto the required number of Zernike polynomials. The data must be expanded onto a larger matrix than

7x7 or 14x14 before the projection onto Zernikes will provide satisfactory results. By discretizing the Zernike polynomials they lose their orthonormality and hence only give satisfactory results if the effects of discretization are minimized. This effect was quantified by looking at the relative change in the variance calculated as a function of matrix size. Figure 4.20 shows the results. Array sizes were always chosen such that the largest change in the variance of any coefficient was  $\leq 1\%$ .

The Zernike coefficients from the mini-Wavescope were used to calculate the spatial parameters of the turbulence for each run in both data sets by comparing them to the expected results from the diagonal of the covariance matrix. An IDL routine called `Zernike2Seeing.pro` was used to do the fitting. `Zernike2Seeing.pro` does not include a calculation of the inner scale. An example result is shown in figure 4.21. The left hand plot shows the mini-Wavescope data for  $\Delta T = 140$  from data set 1 and the right hand plot is the same temperature difference for data set 2. The calculated fit is visually quite good for the low order Zernikes, and gets progressively worse at higher orders. However, for both data sets for higher order modes the data is strictly below the fit. This is evidence of the inner scale. The  $r_0$  associated with the two plots are  $3.3 \pm 0.9$  mm and  $4.2 \pm 0.5$  mm respectively while the  $L_0$ 's are 434 mm and 150 mm. The difference in  $L_0$  could be linked to the orientation change.

The spatial parameters of the turbulence were calculated from the PS measurements using the Zernike expansion of the slope as outlined above in section 4.4.1. The theoretical coefficients were calculated using equation 4.16 and fit to the data using an IDL procedure running `MPFIT` as for the temporal power spectra. The bottom pair of plots in figure 4.22 show an example of this calculation again for  $\Delta T = 140$ . Since each variance in this plot is a linear combination of the Noll Variances, the poor fit at higher order is not simply the inner scale as before. The inner and outer scale affect different modes to different extents in this case. However, visually the data does follow the shape of the theoretical curve. The  $r_0$  calculated using this method is  $2.7 \pm 0.2$  mm for data set 1 and  $6.6 \pm 0.3$  mm for data set 2. The outer scale values are  $70 \pm 10$  mm and  $120 \pm 40$  mm for each set respectively. The inner scale was included in this method using `attis.pro` described above. The values for  $l_0$  were  $5.8 \pm 0.5$  mm and  $3.7 \pm 0.2$  mm.

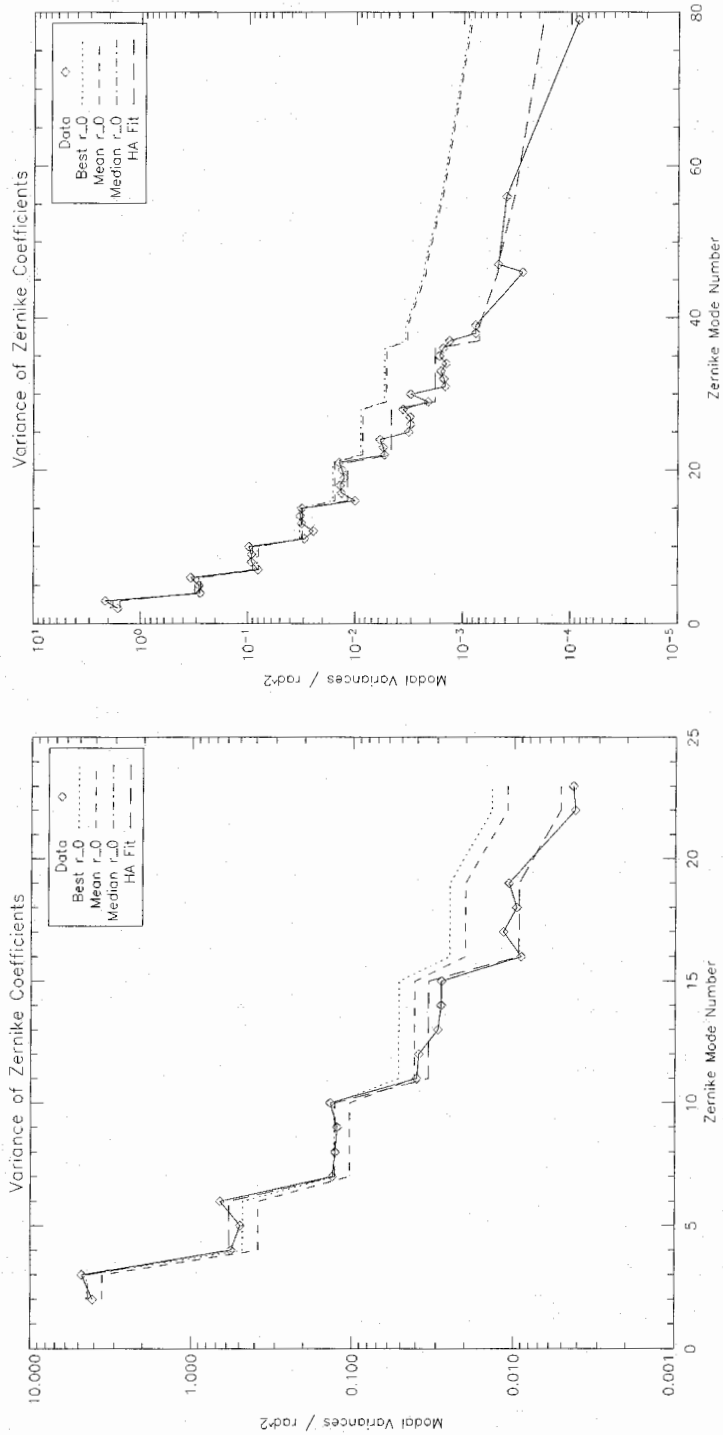


Figure 4.21: **Variations of Zernike Coefficients,  $\Delta T = 140$ :** These plots show the variance of the Zernike coefficients measured with the mini-Wavescope for the same temperature difference in data set 1 (right) and data set 2 (left). For data set 2, 42 Zernike coefficients were output by the mini-Wavescope. Since the ordering was Zygo and not that of Noll, the highest Zernike mode is actually 76. The fits are generated by the two approaches outlined in the text: Zernike2Seeing and using MPFIT to fit the Hill-Andrews model.

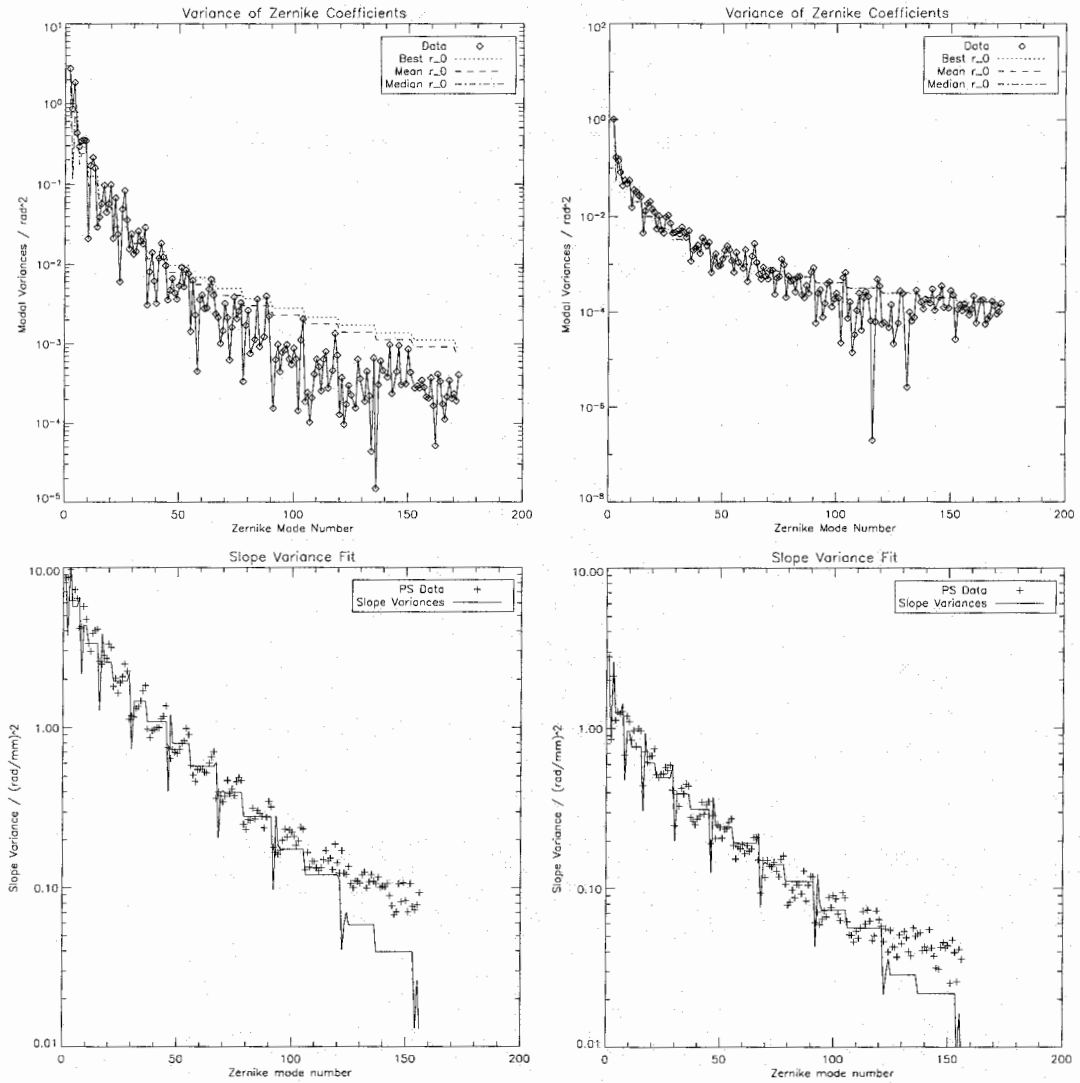


Figure 4.22: **Spatial Characterization Using PS,  $\Delta T = 140$ :** The plots show the fits to the PS data. The right hand side is data set 1 and the left hand side is data set 2. The top plots show the Zernike coefficients calculated by using an SVD to invert equation 4.16. The bottom plots show the slope variance method.

The variances of the coefficients of the Zernike expansion of wavefront were calculated by using an SVD to invert equation 4.16. The `Zernike2Seeing` routine can then be used to calculate the  $r_0$  and  $L_0$  for the PS data. The values given by this method for  $r_0$  are  $2 \pm 1$  mm and  $6 \pm 2$  mm for data sets 1 and 2 respectively. The outer scale values are  $60 \pm 40$  mm and  $130 \pm 70$  mm. These are consistent with the values calculated using the slope method.

Between the WFS's the  $r_0$  values for  $\Delta T = 140$  are largely consistent. Data set 1 agree within the given errors, while for data set 2 the PS gives a larger  $r_0$  than the mini-Wavescope. The PS and mini-Wavescope give consistent values for the outer scale for data set 2; however, the PS gives a much smaller value for data set 1. The values of all of the parameters for each WFS and each method used to analyze the PS data are given in tables in appendix D. The general trends for  $r_0$  as a function of  $\Delta T$  are shown in figure 4.23. For both data sets the results are consistent between the WFS's. However, in both cases the PS systematically underestimates  $r_0$ . This could be due to some residual high order aberration not taken out by the calibration. A candidate for producing this type of effect is the error introduced by the varying sensitivity of the PS due to the diffuser. The plots shown in figure 4.23 are log-log and due to the linearity of the data a function of the form:

$$r_0 = A \cdot \Delta T^b \quad (4.22)$$

was fit to the data. The fitting parameters agree remarkably well between the two data sets indicating that the dependence of  $r_0$  on the temperature difference is not affected by the orientation of the turbulator. One obvious difference between the two data sets is the upturn in  $r_0$  at high  $\Delta T$  in data set 2 shown in the right hand plot of figure 4.23. This effect is seen clearly by both the PS and mini-Wavescope, and was expected from observations made in the lab. This increase in  $r_0$  despite increasing the  $\Delta T$  was the reason for the increased fan speed in the second data set. In the vertical orientation the warm air being blown into the mixing chamber from the hot air channel of the turbulator convects readily out of the mixing chamber. As the temperature of the air increases the effect is worse, and less and less of the hot air mixes with cooler air in the beam path, and as a result  $r_0$  increases.

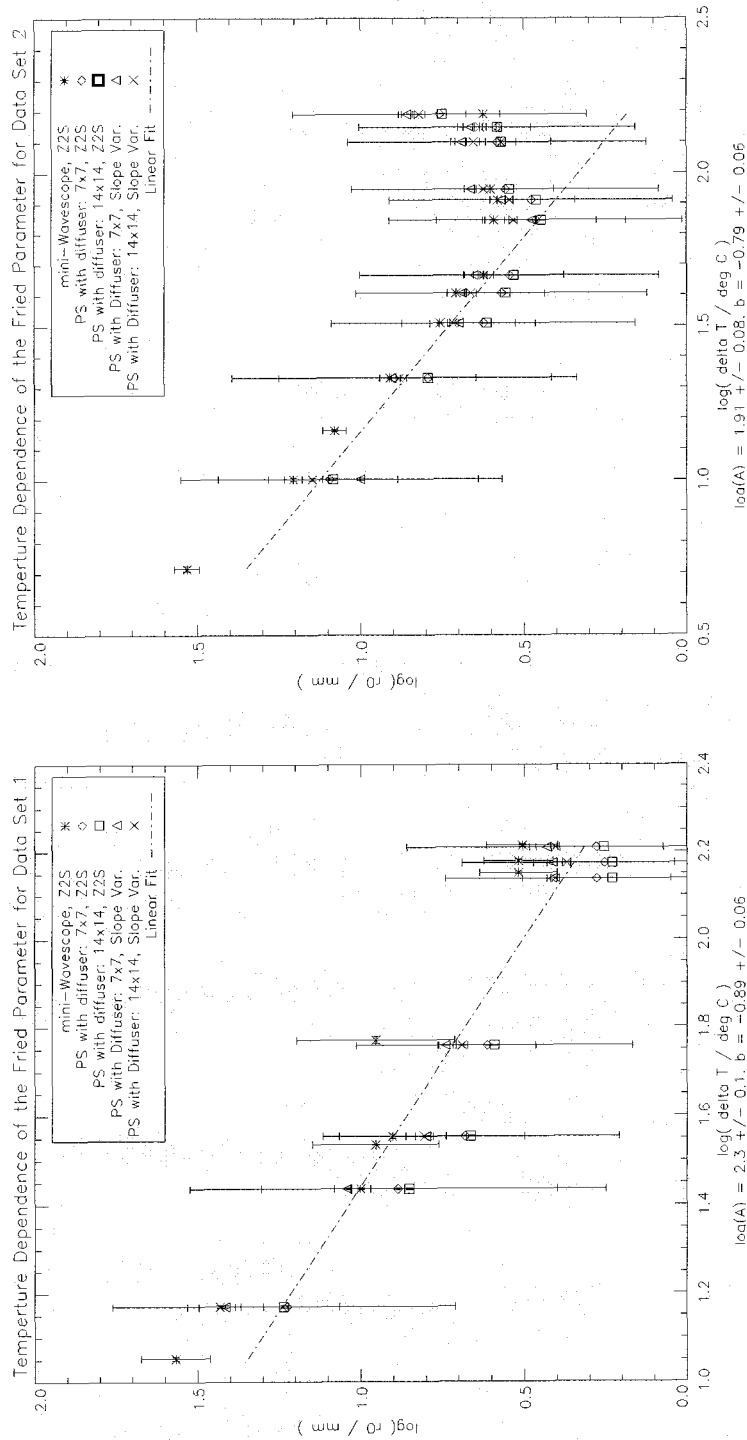


Figure 4.23: **Fried Parameter dependence on  $\Delta T$** : The estimated values of the Fried parameter are shown for data set 1 (left) and data set 2 (right). The values are plotted for both WFS's and for various methods of analyzing the data. The largest error bars are for the 7x7 subaperture configuration of the PS. The trend lines represent a power law fit to the data as described in the text. The parameters of the fit are very similar for the two data sets, indicating that the orientation of the turbulator does not have a serious impact on the behaviour of  $r_0$ .

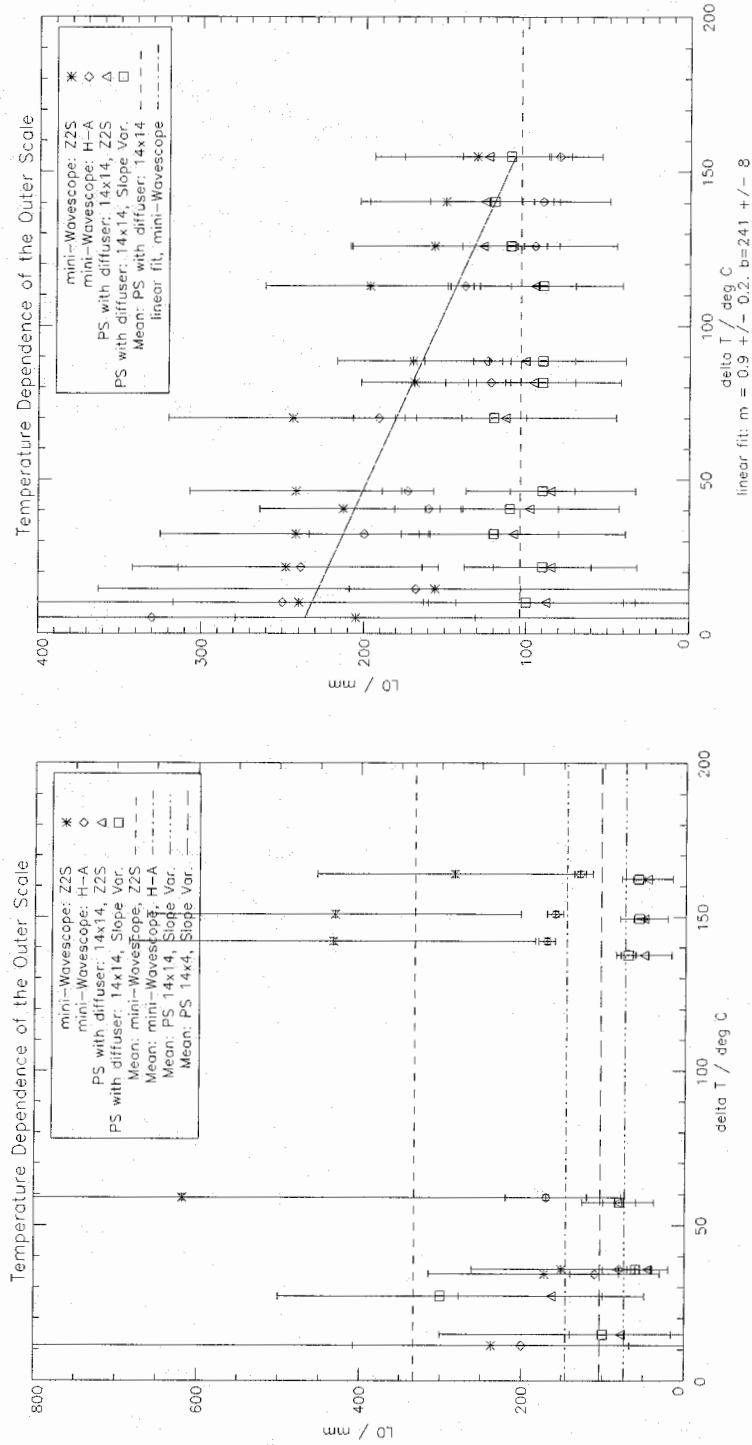


Figure 4.24: **Temperature dependence of the Outer Scale:** The outer scale should be constant with temperature and depend only on the size of the mixing chamber of the turbulator. There are no obvious trends in the values of  $L_0$  for data set 1 (left). The mean values and standard deviations are given in the text. Data set 2 shows a decrease of  $L_0$  with temperature difference in the mini-Wavescope data, and no trend in the PS data.

Figure 4.24 shows the measurements of the outer scale. The results for  $L_0$  do not show as much agreement between the sensors. For data set 1, when analyzed using Zernike2Seeing, the mini-Wavescope data gives outer scales ranging from 172 mm to 618 mm with a mean of 302 mm and a standard deviation of 169 mm. When the Hill-Andrews model is used to fit the data there is less scatter in the best values of  $L_0$ , and in this case the mini-Wavescope gives values between 80 and 200 mm with a mean of 146 mm with a standard deviation of 41 mm. The values of  $L_0$  are systematically smaller when using the Hill-Andrews model compared to the von Karmann case because the attenuation factor for the inner scale actually amplifies the variance at low spatial frequency. The PS in both the 7x7 and the 14x14 configuration, using the slope-variance method or Zernike2Seeing, also gives systematically lower values of  $L_0$ . For mean  $L_0$  for the PS is 74 mm with a standard deviation of 42 mm using Zernike2Seeing and 104 mm and standard deviation 88 mm using the Slope Variance method.

Considering data set 2 the PS also gives systematically lower values of the outer scale:  $100 \pm 10$  mm using either method. The mini-Wavescope data seems to indicate that the outer scale decreases with increasing temperature. This is interesting because it is usually assumed that it depends solely on the size of the mixing chamber. This is most likely another manifestation of the effect of the vertical orientation of the turbulator. The stream of warm air that is convecting out of the turbulator effectively reduces the size of the mixing chamber.

The systematic differences between the PS and mwscp could be related to the static tilts in the turbulator, which are discussed in section 4.6.2. The turbulator introduces a static deflection into the beam. The result of this, for the PS, is that the beam is displaced from the apex of the prism and a larger tilt in the opposing direction is needed to change the intensity on the CCD. The reduced sensitivity lowers the observed variance and leads to an artificially decreased outer scale.

Figure 4.25 shows the measurements of the inner scale. There is again a systematic offset between the two sensors, but the trends are much more evident. The average value for the mini-Wavescope in data set 1 is 11.4 mm with a standard deviation of 1.5 mm while the PS gives 4.4 mm with a standard deviation of 0.3 mm. For data

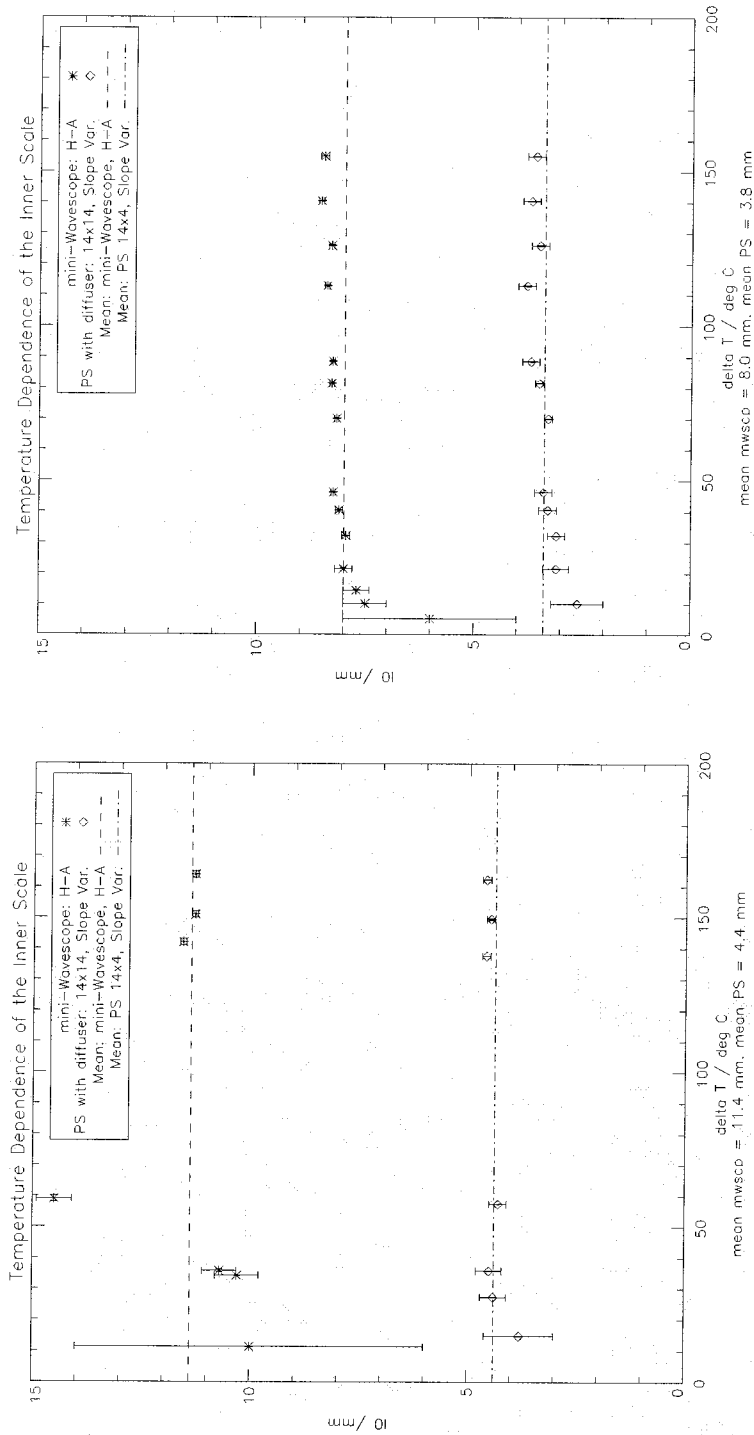


Figure 4.25: **Temperature dependence of the Inner Scale:** The inner scale should also be independent of temperature difference. For data set 1 (left) the mean value estimated from the mini-Wavescope data is 11.4 mm with a standard deviation of 1.5 mm. The PS data gives a value of 4.4 mm with a standard deviation of 0.3 mm. Data set 2 (right) shows a slight trend with temperature and it is the same for both sensors despite a systematic offset. The mini-Wavescope gives a mean value of 8.0 mm with a standard deviation of 0.6 mm, and the PS gives 3.4 mm and a standard deviation of 0.3 mm.

set 2, the mini-Wavescope gives a mean value of 8.0 mm with a standard deviation of 0.6 mm, and the PS gives 3.4 mm and a standard deviation of 0.3 mm. In both cases the mini-Wavescope measures more attenuation on the high order modes. There are several possible explanations for this. Non-common path errors may be playing a role as the optics in the mini-Wavescope arm of the setup may be attenuating high spatial frequencies to a greater extent than those of the PS arm. This could be calculated by comparing the OTF for both arms. There may be some systematic effect introduced by the mini-Wavescope reconstruction process. On the other hand, the PS could be introducing some high spatial frequency aberration into the system and deflating the  $l_0$  value.

## 4.5 1d PS with no Diffuser

Measurements were taken for data set 1 using the PS without the diffuser. Due to the increased sensitivity of the sensor in this configuration, it is common for the DALSA CCD to saturate, but it is still possible to extract information about the turbulence.

Table D.1 shows the spatial parameters of the turbulence calculated from the PS data in the 14x14 subaperture configuration using the slope variance method. The inner scale has a mean value of 4.1 mm and a standard deviation of 0.4 mm which is consistent with the inner scale values calculated using this method and configuration of the PS with the diffuser. It was not possible to calculate the outer scale from this data. The increased sensitivity of the PS without the diffuser is most pronounced for the low order modes, and in the framework of this analysis this manifests itself as an amplification of the variances of the low order modes of the slope expansion, particularly piston, which corresponds to  $y$ -tilt. Thus, the attenuation by the outer scale can not be used, and the fits were performed excluding the first five Zernikes.

Figure 4.26 compares the temperature difference dependence of  $r_0$  for data set 1 measured using the PS with and without the diffuser. The parameters of this fit for the case of the PS without the diffuser are  $\log(A) = 2.63 \pm 0.06$  and  $b = -1.07 \pm 0.04$  according to equation 4.22. These compare well to the fit calculated using only the

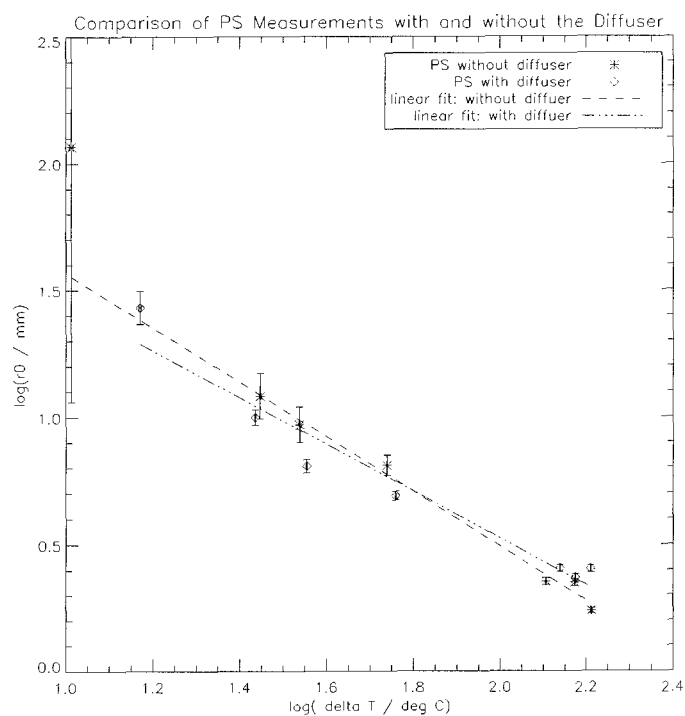


Figure 4.26: **Temperature dependence of  $r_0$  for PS without the diffuser:** This plot shows the  $r_0$  values estimated from the PS data with and without the diffuser for data set 1. The no diffuser data has been scaled to have the same  $r_0$  value at the mean temperature of data set 1 because no calibration was performed for the PS without the diffuser. The trend is very similar, and the coefficients of the fits are given in the text.

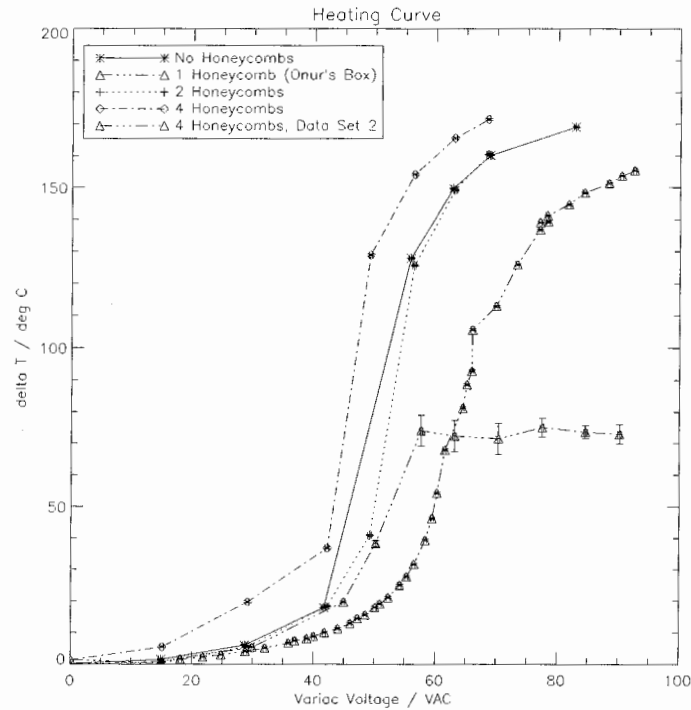


Figure 4.27: **Turbulator Heating Curve:** This plot shows the temperature difference achieved for different variac settings. The different curves represent different lengths of the laminarizing channels in the turbulator. The heating curve of the original turbulator (Onur's box) was also measured.

PS 14x14 with diffuser data:  $\log(A) = 2.4 \pm 0.1$  and  $b = 0.92 \pm 0.09$ . It should be noted that because no calibration curve was taken for the PS without the diffuser, the data for  $r_0$  was scaled to agree with the previous measurements at the mean temperature difference of the no diffuser data. In any case, the trend is nearly the same for all of the measurements.

## 4.6 Other Data Products

### 4.6.1 Turbulator Heating Curves

Figure 4.27 shows data that was collected to measure the ‘heating curve’ of the turbulator, ie., the dependence of the achieved  $\Delta T$  on the variac setting. The common feature of all of the curves in the plot is a steep non-linear increase in the temperature difference after  $\Delta T \sim 40^\circ\text{C}$ . This is one of the difficulties with using the turbulator in its current incarnation. This non-linearity is a property of the ceramic heating elements used in the turbulator (Keskin, 2004). It presents a serious challenge to the calibration of the turbulator by increasing the accuracy of the variac setting necessary to get the desired temperature difference. This coupled with the power law dependence of  $r_0$  on  $\Delta T$  discovered in the experiments outlined above means that a small error in the variac setting can produce a vastly different  $r_0$  inside the mixing chamber.

The different curves in figure 4.27 represent different configurations of the turbulator in terms of the laminarization of the air flow prior to the mixing chamber. The turbulator uses metallic honeycombs to laminarize the flow. The honeycombs come in sheets that are about 1" thick and several layers must be stacked in order to provide channels from the output of the heaters to the mixing chamber. In general the shape of the curves is very similar, but they are shifted in variac voltage. Two layers of honeycombs is nearly the same as none at all, and increasing the number of layers to 4 shifts the curve to lower voltage, indicating that there is less load on the fans in this situation. With four layers in the vertical orientation the curve is shifted in the opposite direction, meaning that there is more load on the fans in this configuration. The curves also point out that the second turbulator does differ from the first. The triangle data point symbols were collected using the first turbulator, designed and characterized by O. Keskin. The temperature difference levels off at a much lower value in this case, and the temperature fluctuations are much larger. The saturation at low temperature difference is not a desirable effect as it limits the minimum  $r_0$  that can be obtained. On the other hand, the large temperature fluctuations indicate

better mixing of the warm and cool air, which is desirable. This difference is likely due to the different plastic casings used to hold the heaters in place.

### 4.6.2 Static Tilts in the Turbulator

The average value of the coefficient of any mode in a Zernike decomposition of the turbulent phase is zero because the atmosphere does not create any static aberrations. This must be the case in the turbulator as well. As a check on the data collected during the course of these experiments, the average values of tilt modes were calculated from the mini-Wavescope data. It should be pointed out that static in this sense refers to an average over time. These are not static aberrations in the sense that they are present in each wavefront.

The results are shown in figure 4.28. The top two plots of the figures show the x-tilt and y-tilt as a function of temperature for both data sets. The static tilt was observed in data set 1 for the horizontal orientation of the turbulator. The y-tilt at the highest temperature difference is roughly a factor of  $\sim 2$  larger than the x-tilt. It was hypothesized that the source of the y-tilt was hot air convecting to the top of the box creating a vertical temperature gradient along the beam path as the air flowed out of the turbulator. This would lead to the factor of two because the beam path through the turbulator is twice the width of the mixing chamber. The vertical orientation of the turbulator was chosen to shorten the beam path through the turbulator, and allow the warm mixed air to flow out of the mixing chamber in the same direction as it would naturally flow by convection. This orientation was chosen for data set 2. The average tilts are shown alongside the results for data set 1 in figure 4.28. The vertical orientation does mediate the effect of the static tilts. The maximum y-tilt is reduced by a factor of  $\sim 3$ , and the maximum x-tilt by factor of  $\sim 4$ . The temperature dependence of the tilts for data set 2 is quite different from that of data set 1. The x-tilt, interestingly, appears to change sign. The y-tilt displays a steady decline after  $\sim \Delta T = 70$ , which is when  $r_0$  begins to increase, as shown in figure 4.23. This supports the deduction that the majority of the hot air is convecting out of the mixing chamber and not mixing in the beam path.

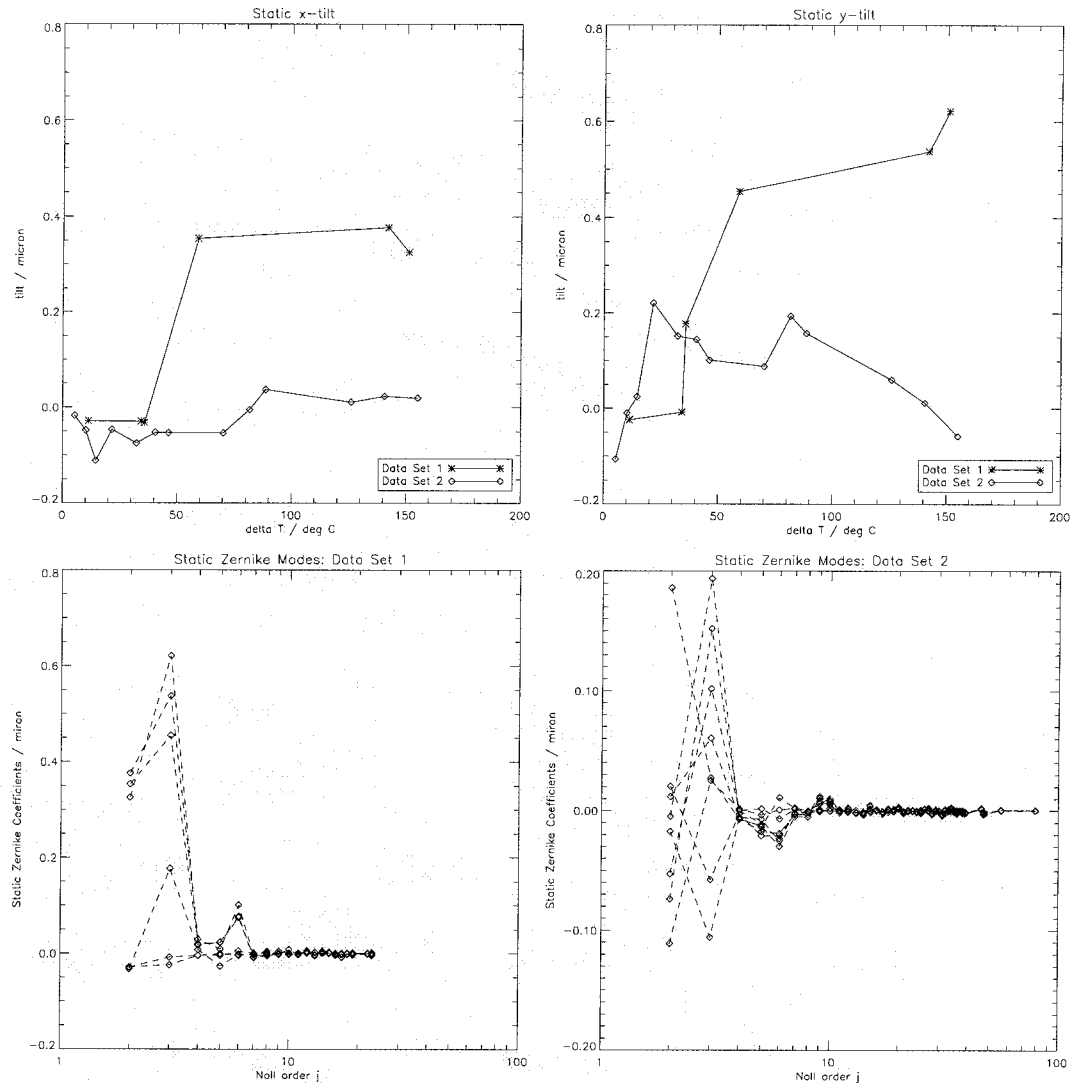


Figure 4.28: **Static Modes in the Turbulator:** The top plots show the temporally averaged Zernike coefficients of the x-tilt mode (left) and y-tilt mode (right) as a function of temperature difference for data set 1 and 2. The static tilts are reduced by the vertical orientation of the turbulator. The bottom plots show the average coefficients for each Zernike mode for data set 1 (left) and data set 2 (right). The different curves are for different temperature differences with the largest coefficients corresponding to larger temperature differences. These plots show that the tilt modes are not the only ones to display this kind of static behaviour.

To confirm that the measured static tilts were in fact due to temperature gradients established within the turbulator, measurements of the air temperature were taken with the Fluke 16 digital multimeter and temperature probe of the air temperature at the edges of the beam inside the mixing temperature. The measurements were taken in the horizontal orientation, across the x direction of the beam (perpendicular to beam path) at a variac setting of 55% (corresponding to roughly a temperature difference of 160°C) and fan speed of 3.35 V. These are approximately the conditions of the highest temperature run in data set 1. The probe is stiff enough to be bent into a position such that it was at the height of the mid-point of the beam and could be held from the outside of the turbulator. This was done to minimize the measurements impact on the air flow. The temperatures measured on each were  $33.8 \pm 0.5^\circ\text{C}$  and  $36.0 \pm 0.5^\circ\text{C}$ . The tilt was calculated to be  $0.7 \pm 0.2\text{rad}$  assuming a constant gradient across the beam and using the dependence of the index of refraction of air found in the CRC Handbook of Chemistry and Physics. The full width of the beam,  $40 \pm 10\text{mm}$ , was used as the turbulator is before the iris. The error in the beam diameter reflects the uncertainty in positioning the end of the probe. In any case, the value for the x-tilt from  $\Delta T = 160$  in data set 1 is  $\sim 4$  rad. Thus, the simple calculation yields a value which is too low; however, this is expected as the size of the effect will increase as the beam propagates and the simple calculation assumes a single layer. It is important to note that calibration problems can also be ruled out as a source of the static aberrations as they are temperature dependent.

The tilt modes are not the only modes that show this behaviour, but they are the most severe. The two lower plots in figure 4.28 show the average values of each mode (ordered according to Noll). The next static modes, in both data sets, are the astigmatism modes ( $j = 5, 6$ ). This is not unexpected as one could imagine two orthogonal gradients to produce some cross-talk with astigmatism. Data set 2 also shows some static behaviour in the trefoil modes.

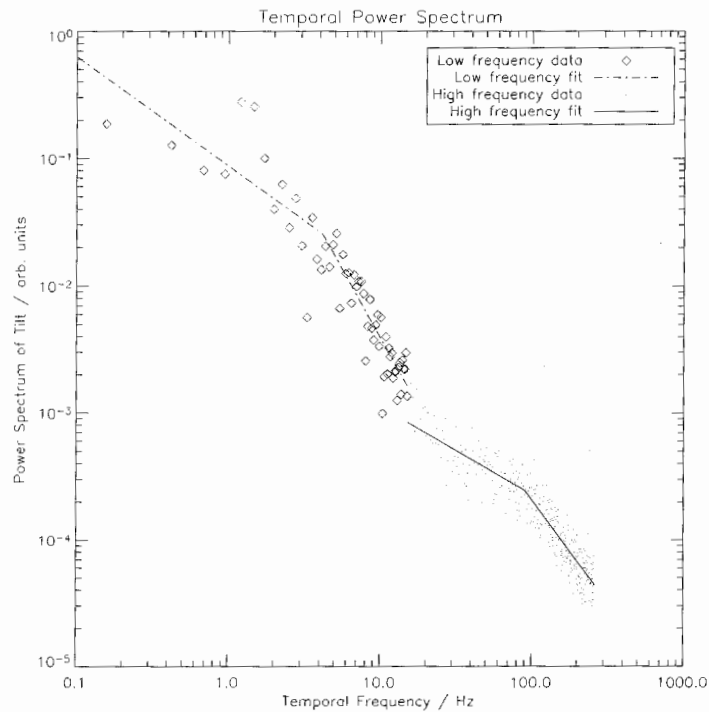


Figure 4.29: **Temporal Power Spectrum, Data Set 2,  $\Delta T = 40$ :** A high frequency fit to the temporal power spectrum of run  $\Delta T = 40$  from data set 2 is shown. The knee frequency is  $f_{knee} = 90 \pm 7$  Hz and the high and low frequency slopes are  $-1.62 \pm 0.06$  and  $-0.7 \pm 0.1$  respectively. This fit corresponds to a proposed second high frequency turbulent layer within the turbulator. The low frequency fit is also shown and its parameters are given in table C.3.

### 4.6.3 Further Temporal Analysis

#### Second Layer in Temporal Power Spectra

Although all of the fits to temporal power spectra calculated from PS data shown in table C.3 were restricted to a frequency range of  $\leq 15\text{Hz}$ , the PS does yield information at higher frequencies due to the much higher frame rate of the DALSA CCD (522 Hz) compared to the Pulnix (30 Hz). All of the temporal power spectra from both data sets for the runs in which the temperature difference alone was changed exhibit the same high frequency behaviour. An example of this is shown in figure 4.29. This plot shows the temporal power spectrum for  $\Delta T = 40$  from data set 2. A fit has been performed in the same manner as those in table C.3. It is clear that there is another regime of a shallow and then steep slope. The knee frequency for this new fit is  $f_{knee} = 90 \pm 7\text{Hz}$  while the high and low frequency slopes are  $-1.62 \pm 0.06$  and  $-0.7 \pm 0.1$  respectively. Thus, this second high frequency layer of turbulence occurs at a characteristic time scale and hence wind speed of  $\sim 20\text{-}50$  times the low frequency layer. Its presence could account for the increased high frequency slope of the previous fits, as the spectrum in the range of  $f \sim 3 - 15\text{ Hz}$  is not strictly the high frequency regime of one type of turbulence but the high frequency regime of one time scale and low frequency regime of another faster time scale. Certainly aliasing of this second high frequency layer could at least account for the increased slope of the high frequency end of the mini-Wavescope temporal power spectra.

The fans used in the construction of the turbulence generator are 12 VDC Circuit Test cooling fans (Part #CFA1212025MS). These fans have an air flow rating of 74.5 cfm.<sup>4</sup> Converting this value to a linear speed of air flowing in a square pipe of cross-sectional area equal to the channel size of the turbulator gives a speed of 1.96 m/s. For a beam size of 20 mm, accounting for the hot and cold channels, gives a time scale of 196 Hz. Assuming that the speed scales linearly with the voltage applied to the fans, 4.41 V for the case of  $\Delta T = 40$ , data set 2 (see table B.2), this gives a frequency of 72 Hz. Thus, a frequency of  $\sim 100\text{ Hz}$  may be expected in the temporal spectrum and this is indeed a ubiquitous feature of all of the spectra with the notable

<sup>4</sup>This unit is cubic feet per minute.

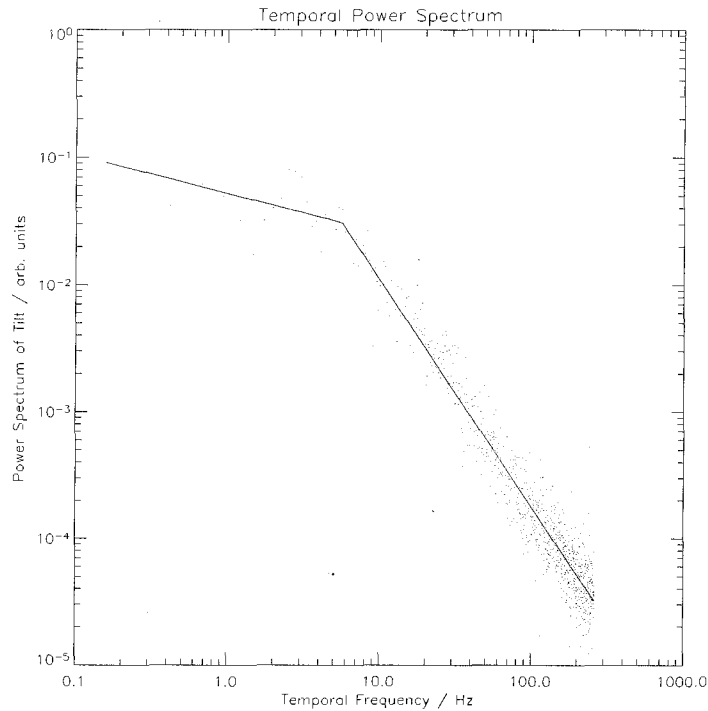


Figure 4.30: **Temporal Power Spectrum, Data Set 2, Wind 900:** This plot shows the temporal power spectrum calculated using the PS data from run wind900 corresponding to a fan voltage of 8.88 V (see table B.2). The fit has been extended for the full frequency range. The new parameters are:  $f_{knee} = 5.6 \pm 0.4$  Hz, low frequency slope:  $-0.30 \pm 0.07$  and high frequency slope:  $-1.79 \pm 0.01$ .

exception of the wind speed runs from data set 2. These will be discussed in the next section.

### Wind Speed

This series of runs in data set 2 were done to investigate the behaviour of the turbulator as the fan speed was varied. The expected behaviour for this experiment was a linear increase of the effective wind speed, parametrized by the knee frequency, in the temporal power spectra with increasing fan speed. As was stated in section 4.4.3, the fan speed for data set 2 was already increased from that of data set 1 ( $\sim 3.3$ V

Table 4.7: Summary of Wind Speed Experiment Parameters.

			SH	PS
run name	variac (VAC)	fan speed (VDC)	$f_{knee}$ (Hz)	$f_{knee}$ (Hz)
$\Delta T = 40$	58.3	4.41	$1.7 \pm 0.6$	$4 \pm 1$
wind 600	67.8	6.04	$4 \pm 2$	$5 \pm 1$
wind 750	77.6	7.48	$4 \pm 2$	$2.4 \pm 0.5$
wind 900	85.9	8.88	$5 \pm 3$	$5 \pm 1$
wind 105	91.8	10.43	$5 \pm 3$	$6 \pm 2$
wind 120	99.9	12.06	$4 \pm 3$	$4.3 \pm 0.7$

to  $\sim 4.4V$ ) because in the vertical orientation of the turbulator, the fan on the hot channel must compete with convection to get the hot air into the beam path. It is also necessary to increase the variac setting with the fan speed to maintain a constant temperature difference, and hence a relatively low value of the temperature difference was chosen for the experiment. See Appendix E.

Table 4.7 summarizes the results of the wind speed experiment. The results are not as was expected. For the majority of the fan speeds the two WFS's agree on the knee frequency with the notable exception on the first point. Regarding just the mini-Wavescope results it appears that the initial increase in the fan speed is enough to double the knee frequency; however, due to the error bars the data is also consistent with no change. This could very well be the case. Figure 4.30 shows the temporal power spectrum of the run wind 900 corresponding to a fan voltage of 8.88 V (see table B.2). The fit has been extended to include the complete range of frequency due to the remarkable linearity of the data. The second layer feature common to all of the temperature difference runs is not clearly visible. It is not visible in runs wind 750, wind 105, and wind 120, and is much less pronounced in run wind 600. See the plots in Appendix E.

The hypothesis drawn from these observations is that a change in the fan speed does not effect the first knee frequency but does change the higher frequency feature, possibly pushing it to even higher frequencies at the limits of what can be detected by the PS CCD. This supports the calculation detailed in the previous section that

Table 4.8: Results of the Airflow Experiments.

conditions	PV ( $\mu\text{m}$ )	RMS ( $\mu\text{m}$ )	VDC	VAC	$T_1$ ( $^{\circ}\text{C}$ )	$T_2$ ( $^{\circ}\text{C}$ )
No $\Delta T$	0.074	0.020	3.31	0	26.5	25.7
unrestricted	0.056	0.014	3.36	69.4	195.3	25.8
restricted	0.058	0.011	3.31	70.0	205	27.6
unrestricted, VDC $\uparrow$	0.474	0.123	4.39	68.8	139.9	27.5
restricted, VDC $\uparrow$	0.163	0.036	4.49	68.8	215.1	29.7

this feature is produced by air moving at the characteristic velocity supplied by the fan.

This suggests that there are two distinct processes occurring in the mixing chamber. The turbulator has a stack of metallic honeycombs which provide channels to laminarize the air flow before it reaches the mixing chamber. Thus, in the high frequency process the air proceeds through the laminarizing stage essentially unimpeded and reaches the mixing chamber at the wind speed provided by the fans. On the other hand, some air is impeded and accounts for the knee frequency measured by mini-Wavescope and PS at 2-5 Hz.

#### 4.6.4 Air flow in the Vertical Turbulator

It has already been mentioned that, in the vertical orientation of the turbulator (shown in figure B.1), the fan speed was changed to improve the mixing of the air. It was hypothesized that restricting the air flow out of the mixing chamber in the vertical orientation of the turbulator would facilitate better mixing and more turbulence. Data was collected using the mini-Wavescope (test `ps.run`) to test this hypothesis. The test reported the average of 100 frames giving the PV and the RMS of the wavefront. The air flow was restricted using a piece of corrugated cardboard with two square holes, approximately 1"x1", cut in the middle, one near the hot channel the other on the cold air side. See figure 4.31

Table 4.8 shows the results. The second row shows that even at very large temperature

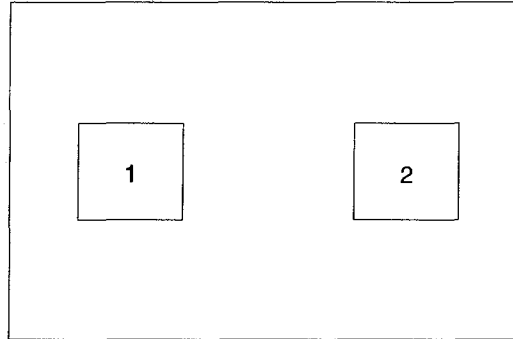


Figure 4.31: **Air flow restriction in the vertical turbulator:** The figure shows a schematic diagram of the sheet of cardboard used to restrict the air flow. Label (1) corresponds to the 1"x1" outlet for the cold air channel and label (2) is the outlet for the hot channel.

differences, the vertical turbulator produces very little turbulence (at low fan speed) as the values of PV and RMS wavefront error have not increased from those of the first row. The third row shows the results of restricting the airflow. The temperature difference is slightly greater, showing that the air is taking longer to escape, but there is still no increase in the turbulence. The fourth row shows the result of the vertical turbulator with increased fan speed. The PV and RMS both increase. Interestingly, if the airflow is restricted at this point, the temperature difference increases, but the strength of the turbulence decreases. This could be an artifact of the particular shape of the holes cut in the cardboard to restrict the airflow, but it is more likely that restricting the airflow in general has an effect on the inner and/or the outer scale. Most likely it dramatically reduces the inertial range by decreasing the outer scale and/or increasing the inner scale. The Zernike coefficients could be analyzed to further study this effect.

A final attempt was made to restrict the airflow in the vertical turbulator while at the same time not decreasing the size of the opening as much as in the previous experiments. This time the top of the mixing chamber was blocked altogether. The hole which formerly housed the window in the horizontal turbulator was opened in the bottom to allow the air to flow out. The airflow is restricted in this case as it must be forced out of the mixing chamber by the fans in the opposite direction to

which it will flow naturally by convection.

Data was collected with the vertical turbulator in this configuration. This is the run named ‘bottom’ from data set 2. This configuration was observed to produce turbulence as evidenced by the  $r_0$  value reported in tables D.4, D.5, D.6 and D.7. The fitting routines failed to extract the spatial parameters from the PS data, however, the mini-Wavescope data gives reasonable values for variances of the Zernike coefficients and the results follow the expected trend very well.

The ‘bottom’ exhibits large static tilts of  $-0.34 \mu\text{m}/\text{subap}$  in x and  $-0.27 \mu\text{m}/\text{subap}$  in y. Thus, as a solution to the airflow problems in the vertical turbulator this too is a failure. Large static tilts were the original reason for going to the vertical turbulator.

# Chapter 5

## Conclusions and Outlook

### 5.1 The Magnitude Gain

It is clear from the study of the Virgo Cluster that the magnitude gain of the PS leads to an increase in available science targets. The number of accessible galaxies rises from 33% of the cluster to 49% using the PS if the magnitude gain is  $\sim 3$  magnitudes on a 30 m telescope. Not only does the number of accessible targets increase, but the portion that can be studied with high Strehl ratio increases. This is due to the reduced WFS noise associated with using the PS to study the galaxies with GS's brighter than the limiting magnitude of the SH WFS. In addition to searching the USNO catalogue, which has practical limitations (see section 3.3), the Bahcall and Soneira model shows that the sky coverage increases by a factor of  $\sim 6$  for a PS with a magnitude gain of 3 at high galactic latitudes such as, for example, where the Virgo cluster is located.

In terms of calculating the magnitude gain from the models, the best value is still uncertain. The initial arguments of Ragazzoni and Farinato, 1999 have been shown to be correct in that the PS propagates less noise on the low-order modes than does the SH WFS. In the case of a 10 m class telescope or an ELT this translates to a magnitude gain of  $\sim 0 \rightarrow 2$  and  $\sim 0 \rightarrow 3$  magnitudes respectively, depending on the

particular noise model of the sensors.

Since the magnitude gain is expected to be largest in the non-modulated regime, the best reconstructor to use in the calculation is that of R. Conan, as it takes into account the actual 2d geometry of the sensor. However, the infinite aperture approximation that makes the signal calculation tractable does not permit a reliable calculation of the variance of the signals. The equation derived does depend on the residual phase variance and has the correct behaviour as this quantity goes to zero; however, to include the effect of the finite width of the PSF, the signals must be calculated for a finite aperture.

In any case, it is also important to think about how this magnitude gain can be realized. It has been pointed out by Esposito and Riccardi, 2001 that the magnitude gain is zero if the residual phase variance is greater than  $\sim 1.5 \text{ rad}^2$ . AO compensation is not effective in the visible because the effect of the atmospheric turbulence is more pronounced at shorter wavelengths. Thus, if the wavefront sensing is done in this band, then the PSF formed on the apex of the pyramid will not be near the diffraction limit and the magnitude gain will be negligible.

## 5.2 Static Modulation with a Diffuser

As figures 4.7 and 4.9 show, the PS implementing modulation using the diffuser does provide a linear response to tilt. The problems associated with using the diffuser discussed in section 4.2.4 can be mediated in two ways. On the DALSA CCD the re-imaged pupil was 84 pixels in diameter. In the 7x7 configuration each subaperture contained 144 pixels and in the 14x14 configuration, 36 pixels. If the focal length of the refocusing lens were to be increased, then the re-imaged pupils can be made arbitrarily small. Thus, by changing the optical layout, each subaperture can be made to have only one pixel in each re-imaged pupil. This would effectively accomplish optically what was done by binning in analyzing the data of the 1d PS and smooth out both the brightness and sensitivity variations. Furthermore, the beam could be expanded to a larger diameter before it passes through the diffuser. This produces

the same effect in that each subaperture would then correspond to a larger area of the diffuser, meaning the brightness and sensitivity variations would again be smoothed out. It should be pointed out that this does not increase the diffusion angle. The angle is independent of the size of the beam which passes through the diffuser, just as with atmospheric turbulence. In addition, the non-uniform sensitivity only requires that the calibration constant be measured for each subaperture. This is really not a ‘show-stopper’ and this type of calibration was calculated in the case of the static aberration. The restriction is that the diffuser must remain in the same position for a given calibration to be valid, and flexibility to take it in and out of the optical set up on the fly was desired for these initial experiments, but is not necessary in a functioning sensor. The brightness variations are more of a concern as they will cause undue limitations of the CCD’s dynamic range; however, if the optical layout is such that the subaperture maps to a restricted number of pixels the light will interfere on the detector, smoothing the intensity in a natural way. Thus, the sensitivity variations can be calibrated out, and the brightness variations can be optically smoothed.

Another, more crucial concern about the diffuser is the size of the diffusing angle. The Angle-of-Arrival variance used by Keskin et al., 2003 is given by

$$\sigma_{AoA}^2 = 0.1698 \left( \frac{\lambda}{D} \right)^2 \left( \frac{D}{r_0} \right)^{\frac{5}{3}} \quad (5.1)$$

and calculating the standard deviation for the strongest turbulence produced in the turbulator,  $\frac{D}{r_0} = 10$ , and the size of the PS subaperture in the 14x14 configuration gives  $\sigma_{AoA} \approx 0.1^\circ$ . Thus, the turbulence produces one-fifth the effect of the diffuser. If the size of the diffusing angle was decreased, the sensitivity of the 1d PS would be increased proportionately. POC does produce smaller diffusion angles, as low as  $0.25^\circ$ , and also produces diffusion films with gradients in the diffusion angle. One of these devices or a diffuser developed in collaboration with the UVIC AO lab may be better suited to the PS.

Looking beyond the lab, a more serious concern with using the diffuser for a real WFS is its chromatic properties. Physical Optics Corporation claims that the diffuser functions independently of wavelength, but this should be tested in the lab. It

is relatively simple to do so. An example experiment would be to illuminate a pinhole with light of various wavelengths, e.g. a bright polychromatic source dispersed with a prism or many monochromatic sources. This light could then be collimated and passed through the diffuser and imaged by a lens system onto a CCD camera. By measuring the size of the image as the wavelength is varied the chromatic dependence of the diffusion angle can be determined. These measurements would allow the chromatic blur of the subapertures to be determined empirically. It is important to ensure that this be taken into account in the error budget.

### 5.3 Modulation by Atmospheric Turbulence

Having a PS operate with no diffusing element is a very attractive idea because it simplifies the sensor: there are no moving parts and no complications introduced by the diffusing element. It has been argued and demonstrated through simulations that the turbulence itself may produce a modulating effect (Costa et al., 2003b). The simulations show the expected behaviour, i.e., that the modulating effect increases with the number of modes both compensated and uncompensated. On the other hand, these simulations rely on the time averaged properties of the turbulence and are effectively addressing the behaviour of a PS using a diffuser which gives a blur corresponding to the temporally averaged properties of the turbulence and not a Gaussian as is the case with the POC LSD's. The important point is that with a temporally and spatially varying aberration like turbulence the diffusing angle depends on both time and space. At any instant for a particular subaperture, it is proportional to the accumulated phase error introduced into the beam passing through the atmospheric cylinder over that subaperture. Thus, if at a particular time, there is a strong turbulent cell over the subaperture in question, the diffusing angle will be larger. Since the diffusing angle determines the sensitivity this means that as the turbulent wavefront evolves so will the sensitivity of the sensor! This is not a desirable effect and effort should be made to understand it.

The UVIC AO lab is in a unique position to study the modulating effects of turbulence on PS measurements by using the turbulator and a DM to essentially repeat the

simulations of Costa, 2003 in laboratory experiments. With a PS in an optical system including a DM and the turbulator, a particular mode can be placed on the DM and its coefficient varied in the presence of turbulence. The reconstructed wavefront can be compared to the input directly and the linear regime mapped out. The lab also has the capacity to do this in open and closed loop if the PS is integrated into the control systems bench. This experiment would provide the answer to the atmospheric modulation question.

In the data collected for this experiment, the modulating effects of the atmosphere can be seen. This is evident in the spatial characterization of turbulator using the PS with no diffuser. The variance of the higher order Zernike modes follow the expected power law, but the lower orders do not. With no modulation, the turbulence does not provide enough wavefront aberration on time scales of  $\sim 500$  Hz to cause the system to be significantly out of the diffraction limit. Thus, the PS has an increased sensitivity to the low order modes, foremost of which is tilt. This leads to an increased variance measured for the low order modes, and is the reason why the outer scale could not be measured: the non-linearity of the sensor produces an apparent amplification of the low order modes! In any case, this is also experimental evidence that there is a magnitude gain because of the increased sensitivity, but it is difficult to estimate because of the saturation of the DALSA CCD when the diffuser is not used.

## 5.4 Open Loop Measurements of Turbulence

The PS was able to characterize open loop turbulence, and provide estimates of the three critical spatial and temporal parameters of the turbulence. This was facilitated by the diffuser. The diffuser provides a large dynamic range over which the measurements are linear and prevents the CCD from saturating even under the large aberrations present in the open loop turbulence.

AO systems are usually run in a closed loop configuration, meaning that the WFS measures the residual phase aberrations in the corrected wavefront, and, hence, its dynamic range is suited to these much smaller errors not those of the incoming

turbulent wavefront. In the realm of the TMT Project, one of the novel AO modes under study is Multi-Object AO. This technique relies on being able to measure open loop turbulence using a high dynamic range WFS. It has been suggested that such a device could consist of a normal SH WFS and a MEM's DM. The DM would provide a corrected wavefront to the SH WFS which could then measure the error. While this device maintains the high sensitivity of the closed loop SH WFS, it adds the complexity of controlling a DM as part of the WFS itself. PS's employing static modulation using a diffuser could be an alternative to this approach. Although it would lack the sensitivity of the SH WFS + DM device, it would not involve the increased complexity of the DM and have no moving parts.

## 5.5 NextGen: PS and Turbulator

### 5.5.1 Future PS Research

There has been extensive discussion between L. Jolissaint, O. Keskin, G. Herriot and the author about the continuation of the work begun in this thesis project. The purpose of the SLODAR experiment was to resolve the turbulent layers inside the mixing chamber of the turbulator and provide a measurement of the  $C_n^2$  profile. This is an important step before using the turbulator with MCAO or MOAO systems because the anisoplanatic properties of the AO system are determined not solely by the strength of the turbulence, i.e.,  $r_0$ , but by the vertical distribution of the turbulent layers. Increasing the strength of the high altitude layers will decrease the anisoplanatic angle because there is more turbulence in the region where the cylinders of light corresponding to the GS and the target do not overlap. The initial experiment showed that the technique and analysis work, but that the height resolution was insufficient to resolve the layers (Jolissaint et al., 2004a). The SLODAR research continues and the experiment is being redesigned by O. Keskin and L. Jolissaint to have a height solution of  $\sim 3$  cm.

In parallel with this the PS project will (may) continue and a design based on the Star

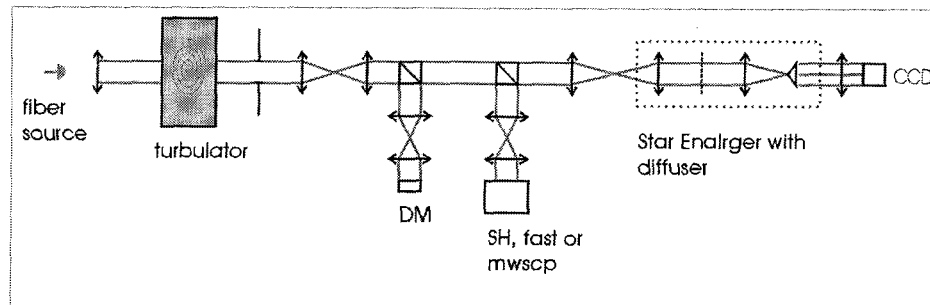


Figure 5.1: **Set-up for Integration and Testing of SE's:** This figure shows a schematic diagram of a setup for integration and testing of the SE's. The DM, iris, SH WFS, and SE detector must all be conjugate planes. This allows for calibration of the SE with the DM, as well as the potential for measuring turbulence.

Enlargers (SE's) used in ESO's MAD will be contracted out (Ragazzoni et al., 2001). The star enlarger gets its name because it has a pair of lenses before the pyramid, just as with the 1d PS, which re-image the GS on the apex of the pyramid. These lenses increase the focal ratio and thereby enlarge the star image. This has several practical advantages: it decreases the roof and edge tolerances, it allows the re-imaged pupils to be de-magnified in the detector plane, the SE can be used with and without the diffuser, and different focal plane masks can be used. This idea modularizes the PS by mounting the lenses and pyramid (and diffuser) on their own support structure. The SE can then be thought of as an optical device with an input of beam of a certain F-number and an output of four beams of a F-number equal to that of the beam after the re-imaging lens which are diverging from one another by an angle proportional to the apex angle of the pyramid.

Integration and testing of the SE's could proceed with a bench setup like that shown in figure 5.1. Using this setup specific modes can be put on the DM and the PS response measured allowing the full interaction matrix to be obtained. The amplitude of the modes can also be adjusted to study the non-linearity of the PS without modulation as was done in the PYRAMIR project (Costa et al., 2004b). Experiments can also be carried out to measure the response of the PS to specific modes in the presence of turbulence as was suggested above.

A lot of interesting avenues of research open up once the SE's are calibrated. The SE's could be used in the SLODAR setup. The measurements provided by the SE's can be combined to perform a tomographic reconstruction of the turbulent volume in the turbulator (Tallon and Foy, 1990; Ragazzoni et al., 1999). This can be done in two configurations: with each SE measuring the total integrated phase error along the line of sight to a particular GS and with the pupils re-imaged at different altitudes. These correspond to the star-oriented and layer-oriented wavefront sensing techniques discussed in the introduction. These measurements could then be compared to the  $C_n^2$  profile measured using SLODAR. This type of measurement has only been performed once to date, at the TNG telescope using a single star asterism (Ragazzoni et al., 2000c). The wavefront sensing was not done with PS's or SH WFS's but with a one-sided curvature wavefront sensing technique not employed on AO systems (Hickson and Burley, 1994; Hickson, 1994; Ribak, 1995). R. Dekany's research group at Palomar is extending this experiment on-sky using four SH WFS's; however, control over the atmospheric conditions the number, height (for simulating LGS's), brightness and geometrical configuration of the GS's, as well as the capacity for comparison with the SLODAR technique, makes the laboratory a powerful proving ground for tomography and layer-oriented wavefront sensing.

Another line of experimentation has been suggested by G. Herriot and it addresses the magnitude gain. The magnitude gain of the PS can only be realized if the PSF on the apex of the pyramid approaches the diffraction limit. Significant AO compensation is only achieved in the infrared. With an SE integrated into the closed loop AO system, measurements could be made for  $r_0$ 's scaled appropriately for the infrared and the visible. These measurements could be used to assess whether or not it is feasible to realize a magnitude gain with available infrared detectors.

### 5.5.2 Turbulator Development

The next iteration in the development of the turbulator stems from the measurements made in the course of this thesis project. The static modes in the turbulator must be removed, particularly the tip-tilt as it is the largest, and will consume the most of the

dynamic range of the WFS's and DM's. To do this it has been proposed to split each channel into two channels to allow opposing flows of warm to cool and cool to warm air. In this way there should be opposing gradients in the mixing chamber and the associated tilts will cancel. The gradient on the other axis is due to convection of the warm air. To remove this gradient the airflow must be aligned with the convective flow.

A separate issue is the non-linearity of the heaters. This impacts the repeatability of the turbulator, as discussed in section 4.6, because the  $\Delta T$  rises very sharply and  $r_0$  shows a power law dependence on  $\Delta T$ . Thus, a small error in the variac setting can lead to a very different  $\Delta T$  and  $r_0$ . This problem can be addressed by creating a reservoir of hot air. In this case, the fan does not force air through the heater, but pulls it out of the reservoir. For a given variac setting and fan speed the reservoir and the hot air stream will reach an equilibrium temperature. The larger the reservoir and the lower the fan speed the more linear the relationship between variac setting and  $\Delta T$  should be. The size of the reservoir required can be calculated from the airflow rating of the fans chosen for the new turbulator.

The final issue with the turbulator, as it is currently implemented, is related to the fans. In the atmosphere, turbulence arises when streams of air at differing temperatures mix. This is the case in the turbulator as well; however, in the atmosphere the usual paradigm is that the air has already mixed and the mixed air is moved across the telescope aperture by the wind. This is the well known Taylor or Frozen Flow Hypothesis (Tyson, 1998). In the turbulator the mixing is done directly in the beam path. This eliminates the possibility of frozen flow. The degree to which atmospheric turbulence follows frozen flow is still being debated, but a closer emulation of the atmospheric processes will give better results. To address this concern, the process of mixing in the turbulator must be separated from the 'wind'. The hot and cold air could be forced together by two separate sets of fans much as it is now. The mixed air could then be propelled by a third fan across the beam path. To assess the degree

---

of frozen flow in this configuration one could compute the temporal correlation function of the tilts measured in subapertures in rows aligned with the direction across the beam in which the wind blows. If there is indeed frozen flow, there will be a peak in the correlation function at a time lag corresponding to  $\sim \frac{nd}{v}$  where  $n$  is separation in numbers of subapertures,  $d$  is the subaperture size, and  $v$  is the wind speed.

# Appendix A

## PS Signal Variance Derivation

To calculate the signal variance,  $\sigma_S^2$ , of the PS, it is considered to be equivalent to the Foucault knife-edge test, and the model in V erinaud, 2004 will be used. The basic equation is equation 2.17. In this case the knife edge is parallel to the y-axis in the focal plane.  $|U_p^+(x, y)|^2$  describes the intensity observed when the knife edge blocks the  $x < 0$  half plane of the focal plane and  $|U_p^-(x, y)|^2$  is the intensity observed when the knife edge blocks the  $x > 0$  half plane. Equation 2.23 gives the signal of the PS. Substituting equation 2.22 in to equation 2.23 and manipulating the result, the signal can be re-written as

$$S = \frac{1}{\pi} \int_{-\infty}^{\infty} \frac{\sin(\phi(t, y) - \phi(x, y))}{t - x} dt. \quad (\text{A.1})$$

The approximation

$$\sigma^2 \left[ Q = \frac{N}{D} \right] \approx \frac{\sigma^2[N]}{\langle D \rangle^2} \quad (\text{A.2})$$

will be used to calculate the signal variance. The mean of the denominator in equation 2.17 is simply  $A^2$  as the intensity follows Poisson statistics. The variance of the numerator is much more involved and it will be developed independently.

To calculate the variance of the numerator, the approximation that  $\phi \ll 1$  is used

and thus small angle approximation for sin applies. Re-writing equation A.1

$$S = \frac{1}{\pi} \left( \int_{-\infty}^{\infty} \frac{\phi(t, y)}{t - x} dt - \int_{-\infty}^{\infty} \frac{\phi(x, y)}{t - x} dt \right) \quad (\text{A.3})$$

it can be seen that the first term is a convolution, while the second term leads to

$$\int_{-\infty}^{\infty} \frac{1}{t - x} dt = \begin{cases} -\ln \left| \frac{x+(1-y^2)^{1/2}}{x-(1-y^2)^{1/2}} \right| & , x^2 + y^2 < 1 \\ -\ln \left| \frac{x+(1-y^2)^{1/2}}{x-(1-y^2)^{1/2}} \right| + i\pi & , y^2 < 1 < x^2 + y^2 \\ 0 & , 1 < y^2. \end{cases} \quad (\text{A.4})$$

where the different regions correspond to the features of the pupil image seen after the knife-edge test (i.e. the inside of the pupil and the halo). (Linfoot, 1946) Linfoot's notation has been used. The x and y coordinates of the pupil are normalized such that the pupil is scaled to the unit circle. This result is used to obtain equation 2.16 and is shown plotted inside and outside the pupil in figure 2.7. Since the second integral in equation A.3 is a product of the above integral with  $\phi(x, y)$  and  $\phi(x, y)$  is zero outside the pupil, only the first case in equation A.4 is needed.

The variance of the first term of equation A.3 is calculated as follows

$$\begin{aligned} \sigma^2 \left[ \int_{-\infty}^{\infty} \frac{\phi(t, y)}{t - x} dt \right] &= \sigma^2 \left[ \phi(x, y) \otimes \frac{p.v.}{x} \right] \\ &= \sigma^2 \left[ \frac{\partial}{\partial x} \phi(x, y) \otimes \ln|x| \right] \\ &= \sigma^2 \left[ \mathcal{F} \left[ \frac{\partial}{\partial x} \phi(x, y) \right] \mathcal{F}[\ln|x|] \right] \\ &= \sigma^2 \left[ 2\pi i f_x \mathcal{F}[\phi(x, y)] \frac{1}{2f_x} \right] \\ &= \pi^2 \sigma^2 [\mathcal{F}[\phi(x, y)]] \\ &= \pi^2 \sigma_{\phi}^2. \end{aligned} \quad (\text{A.5})$$

The first step of equation A.5 is a property of distributions. (Conan, 2004) The third step uses the Convolution theorem and Parseval's theorem. The fourth line uses the fact that  $\mathcal{F}[\ln|x|] = \frac{1}{2f_x}$ . Parseval's theorem is used again in the last step. The

variance of the second term of equation A.3 is calculated as follows

$$\begin{aligned}
\sigma^2 \left[ \phi(x, y) \int_{-\infty}^{\infty} \frac{1}{t-x} dt \right] &= \sigma^2 \left[ \phi(x, y) \ln \left| \frac{x+Y}{x-Y} \right| \right] \\
&= \sigma^2 \left[ \phi(x, y) \ln \left| \frac{x+1}{x-1} \right| \right] \\
&= \sigma^2 \left[ \mathcal{F}[\phi(x, y)] \otimes \mathcal{F} \left[ \ln \left| \frac{x+1}{x-1} \right| \right] \right] \\
&= \sigma^2 \left[ \sin(2\pi f_x) \mathcal{F}[\phi(x, y)] \otimes \frac{1}{f_x} \right], \\
&= \sigma^2 \left[ \sin(2\pi f_x) \frac{\partial}{\partial x} \mathcal{F}[\phi(x, y)] \otimes \ln|f_x| \right] \\
&= 4\pi^2 \sigma^2 [\sin(2\pi f_x) \mathcal{F}[x\phi(x, y)] \otimes \ln|f_x|] \\
&= 4\pi^2 \sigma^2 \left[ \sin(2\pi f_x) \mathcal{F}[\phi(x, y)] \otimes (\mathcal{F}[x] \otimes \mathcal{F} \left[ \frac{1}{2x} \right]) \right] \\
&= \pi^2 \sigma^2 [\mathcal{F}[\sin(2\pi f_x)] \otimes \phi(x, y)] \\
&= \pi^2 \sigma^2 [\sin(2\pi x) \phi(x, y)] \\
&= \pi^2 \int_{-\infty}^{\infty} \int_{-\infty}^{\infty} d^2 \mathbf{x} |\sin(2\pi x) \phi(x, y)|^2 \\
&\approx \frac{\pi^2}{2} \sigma_\phi^2
\end{aligned}$$

The first step assumes that calculation is done along the central diameter,  $y=0$ . The second step uses the Convolution theorem and Parseval's theorem. The third step relies on the result for  $\mathcal{F}[\ln|x|]$  and the Shift theorem. The next step uses the same property of distribution mentioned above and the following one makes use of equation 2.56. After that the Convolution theorem is used to rewrite the expression and an inverse Fourier transform is taken. At this point the variance can be evaluated by replacing  $\sin^2$  with its average value.

Using the results of equations A.5 and A.6 the signal variance of the PS can be written as

$$\sigma_S^2 = \frac{6}{\langle A \rangle} \sigma_\phi^2 \quad (\text{A.6})$$

where  $A$  is the amplitude of the electric field phaser in equation 2.22. The limit as the residual phase goes to zero has the expected behaviour

$$\lim_{\sigma_\phi^2 \rightarrow 0} \sigma_S^2 = 0. \quad (\text{A.7})$$

# Appendix B

## Parameters of the Data Sets

This appendix gives the parameters of the two data sets. Table B.1 describes data set 1. This data was collected with the turbulator in its horizontal position. The data was collected in three stages. The mini-Wavescope data was collected first, and then the same variac settings were revisited to acquire the data for the PS both with and without the diffuser in place. The hope was to make measurements at a variety of temperature differences spanning those used previously. (Keskin et al., 2003), and the names of the runs suggest the approximate temperature difference achieved, while the actual  $\Delta T$  is reported in column 7. The non-linear relationship between variac setting and  $\Delta T$  is obvious by examining the values reported in columns 2 and 7. This will be discussed further in section 4.6. Data Set 2 was collected with the turbulator in an alternate orientation and is detailed in table B.2. The first 13 runs were collected at different variac settings, i.e. temperature differences. The runs named ‘wind x’ were collected with the temperature difference maintained at approximately 40°C while varying the fan speed of the turbulator. . The final run was collected in yet another configuration of the turbulator. These data will be discussed in section 4.6.

Figure B.1 shows an overhead view of the turbulator in the horizontal (a) and vertical (b) configurations.

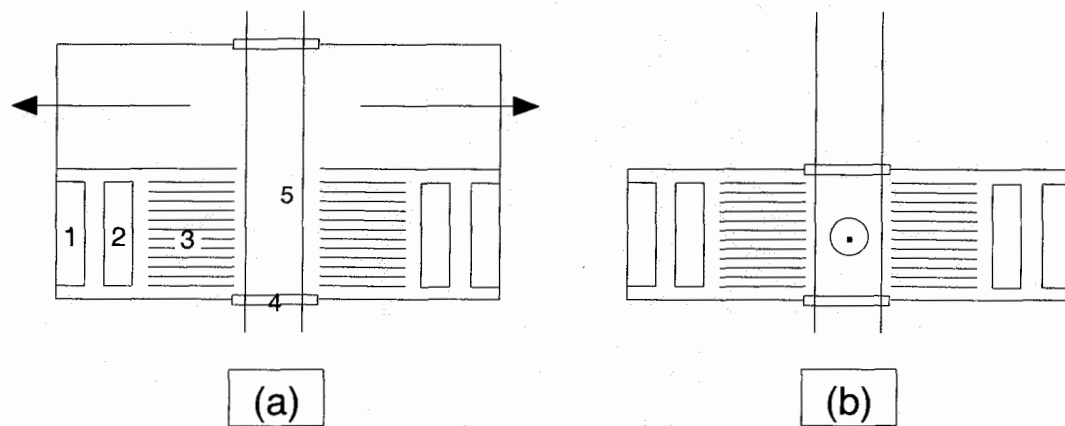


Figure B.1: **Schematic of Horizontal and Vertical turbulators:** This diagram shows schematically an overhead view of the turbulator in the horizontal (a) and vertical orientations (b). The labels in the horizontal turbulator diagram correspond to the basic components of the turbulator: (1) represents the fans, (2) the heaters, (3) the channels provided by the honeycombs discussed in section 4.6, (4) the window (the opposing side also has one), and (5) shows the beam passing through. The arrows indicate that the air flows out the sides of the turbulator. In the vertical case shown in (b) the same labels apply. The circle with the central dot is meant to represent that the air flows out of the page in this configuration.

Table B.1: Data Set 1 (Horizontal Turbulator).

Data Set 1 mini-Wavescope					
run name	date	variac (% $V_{max}$ )	fan speed (V)	Laser (mA)	$\Delta T$ ( $^{\circ}\text{C}$ )
$\Delta T = 10$	2004-10-27	20	3.34	$46.6 \pm 0.3$	$11.3 \pm 0.1$
$\Delta T = 30$	2004-10-27	25	3.33	$46.6 \pm 0.3$	$34.3 \pm 0.1$
$\Delta T = 40$	2004-10-31	26	3.33	$46.1 \pm 0.3$	$35.8 \pm 0.4$
$\Delta T = 55$	2004-10-31	28	3.35	$46.6 \pm 0.3$	$59 \pm 1$
$\Delta T = 140$	2004-10-27	30	3.34	$46.6 \pm 0.3$	$142 \pm 1$
$\Delta T = 150$	2004-10-27	40	3.32	$46.6 \pm 0.3$	$151 \pm 1$
$\Delta T = 160$	2004-10-27	55	3.34	$46.6 \pm 0.3$	$164 \pm 1$
PS with Diffuser					
$\Delta T = 10$	2004-10-31	20	3.32	$47.0 \pm 0.1$	$14.8 \pm 0.1$
$\Delta T = 30$	2004-10-31	25	3.31	$46.9 \pm 0.1$	$27.3 \pm 0.1$
$\Delta T = 40$	2004-10-31	26	3.32	$46.5 \pm 0.1$	$35.8 \pm 0.1$
$\Delta T = 55$	2004-10-31	28	-	-	$57.4 \pm 0.1$
$\Delta T = 140$	2004-10-31	30	3.31	$46.6 \pm 0.1$	$137.6 \pm 0.1$
$\Delta T = 150$	2004-10-31	40	3.33	$46.7 \pm 0.1$	$149.5 \pm 0.3$
$\Delta T = 160$	2004-10-31	55	3.32	-	$162.3 \pm 0.1$
PS without Diffuser					
$\Delta T = 10$	2004-11-01	20	3.32	$46.7 \pm 0.1$	$10.3 \pm 0.1$
$\Delta T = 30$	2004-11-01	25	3.31	$46.7 \pm 0.1$	$28.0 \pm 0.1$
$\Delta T = 40$	2004-11-01	26	3.34	$46.8 \pm 0.1$	$34.5 \pm 0.1$
$\Delta T = 55$	2004-11-01	28	3.34	$46.8 \pm 0.1$	$54.8 \pm 0.1$
$\Delta T = 140$	2004-11-01	30	3.34	$47.0 \pm 0.1$	$127.7 \pm 0.1$
$\Delta T = 150$	2004-11-01	33	3.34	$46.8 \pm 0.1$	$149.0 \pm 0.1$
$\Delta T = 160$	2004-11-01	55	3.34	$46.6 \pm 0.1$	$162.8 \pm 0.4$

Table B.2: Data Set 2 (Vertical Turbulator).

Data Set 2					
run name	date	variac (VAC)	fan speed (VDC)	$\Delta T$ ( $^{\circ}\text{C}$ )	error ( $^{\circ}\text{C}$ )
$\Delta T = 5$	2004-11-15	32.0	4.44	5.2	0.1
$\Delta T = 10$	2004-11-15	41.8	4.44	10.1	0.1
$\Delta T = 15$	2004-11-16	47.2	4.42	14.5	0.1
$\Delta T = 20$	2004-11-16	52.8	4.40	21.5	0.1
$\Delta T = 30$	2004-11-16	56.5	4.40	32.3	0.1
$\Delta T = 40$	2004-11-16	58.3	4.41	40.5	0.1
$\Delta T = 55$	2004-11-16	59.4	4.41	46.3	0.1
$\Delta T = 70$	2004-11-17	61.5	4.41	70.1	0.1
$\Delta T = 80$	2004-11-17	64.4	4.40	81.6	0.1
$\Delta T = 90$	2004-11-17	65.1	4.41	88.6	0.2
$\Delta T = 110$	2004-11-17	69.9	4.40	113.0	0.2
$\Delta T = 125$	2004-11-17	73.3	4.40	126.0	0.2
$\Delta T = 140$	2004-11-17	78.3	4.39	140.5	0.1
$\Delta T = 155$	2004-11-18	92.5	4.41	155.0	0.1
wind 600	2004-11-18	67.8	6.04	40.8	0.1
wind 750	2004-11-18	77.6	7.48	42.5	0.3
wind 900	2004-11-18	85.9	8.88	42.8	0.2
wind 105	2004-11-18	91.8	10.43	40.5	0.2
wind 120	2004-11-18	99.9	12.06	42.2	0.3
bottom	2004-11-18	51.3	4.41	41.4	0.1

# Appendix C

## Data Tables: Temporal Parameters

The data tables in this appendix give all of the parameters of the calculated temporal power spectra.

Table C.1: Data Set 1 Temporal Power Spectra Parameters, PS with no Diffuser.

Data Set 1	$f_{knee}$ (Hz)	error (Hz)	low-frequency slope	error	high-frequency slope	error	$\delta_y$
$\Delta T = 10$	10.1	0.3	-0.75	0.04	-3.35	0.05	0.2
$\Delta T = 30$	8.4	0.3	-0.93	0.04	-3.40	0.05	0.3
$\Delta T = 40$	13.0	0.2	-0.97	0.03	-4.49	0.07	0.3
$\Delta T = 55$	2.2	0.2	-0.47	0.09	-2.09	0.03	0.3
$\Delta T = 140$	16.5	0.5	-1.24	0.03	-3.24	0.09	0.3
$\Delta T = 150$	5.6	0.3	-0.54	0.05	-2.29	0.04	0.3
$\Delta T = 160$	5.0	0.3	-0.49	-0.06	-2.14	0.03	0.3

Table C.2: Temporal Power Spectra Parameters, mini-Wavescope.

Data Set 1	$f_{knee}$ (Hz)	error (Hz)	low-frequency slope	error	high-frequency slope	error	$\delta_y$
$\Delta T = 10$	1.0	0.1	0	1	-1.9	0.2	0.1
$\Delta T = 30$	5	1	-0.7	0.3	-2.9	0.6	0.1
$\Delta T = 40$	4	2	-0.9	0.4	-2.6	0.5	0.2
$\Delta T = 55$	5	2	-0.7	0.3	-2.7	0.7	0.1
$\Delta T = 140$	6	2	-0.9	0.3	-2.5	0.8	0.1
$\Delta T = 150$	3	1	-0.6	0.5	-2.1	0.4	0.1
$\Delta T = 160$	5	2	-0.8	-0.4	-2.3	0.6	0.1
Data Set 2							
$\Delta T = 5$	1.6	0.8	0	0.8	-1.5	-0.2	0.1
$\Delta T = 10$	3	1	-0.3	0.5	-1.8	-0.3	0.1
$\Delta T = 15$	5	1	-0.4	0.3	-2.2	-0.5	0.2
$\Delta T = 20$	5	2	-0.8	0.3	-2.2	-0.5	0.2
$\Delta T = 30$	1.8	0.7	0.1	0.6	-1.8	-0.3	0.1
$\Delta T = 40$	1.7	0.6	0.2	0.6	-1.7	-0.2	0.1
$\Delta T = 55$	2.7	0.7	0.0	0.5	-2.3	-0.3	0.2
$\Delta T = 70$	2.4	0.7	0.0	0.5	-2.0	-0.3	0.2
$\Delta T = 80$	2.7	0.9	-0.1	0.5	-2.2	0.3	0.2
$\Delta T = 90$	3.4	0.9	-0.3	0.4	-2.3	0.4	0.1
$\Delta T = 110$	3.9	0.9	-0.4	0.3	-2.6	0.4	0.1
$\Delta T = 125$	3.3	0.8	-0.3	0.3	-2.4	0.4	0.2
$\Delta T = 140$	4	1	-0.5	0.3	-2.8	0.4	0.1
$\Delta T = 155$	2.7	0.9	-0.2	0.5	-2.3	0.3	0.1
wind 600	4	2	-0.4	0.4	-2.0	0.5	0.1
wind 750	4	2	-0.2	0.5	-1.3	0.5	0.1
wind 900	5	3	-0.1	0.3	-1.3	0.7	0.1
wind 105	5	3	-0.1	0.3	-1.3	0.7	0.1
wind 120	4	3	0.0	0.5	-0.8	0.4	0.1
bottom	1.3	0.7	0.0	0.4	-1.4	0.3	0.1

Table C.3: Temporal Power Spectra Parameters, PS.

Data Set 1	$f_{knee}$ (Hz)	error (Hz)	low-frequency slope	error	high-frequency slope	error	$\delta_y$
$\Delta T = 10$	3	4	-1.0	0.3	-1.4	0.3	0.2
$\Delta T = 30$	3	1	-1.2	0.3	-2.3	0.3	0.2
$\Delta T = 40$	2.6	0.5	0.3	0.3	-2.4	0.2	0.2
$\Delta T = 55$	5	1	-1.0	0.2	-2.9	0.5	0.2
$\Delta T = 140$	5	1	-0.8	0.2	-2.8	0.4	0.2
$\Delta T = 150$	4	1	-0.8	0.2	-2.6	0.3	0.2
$\Delta T = 160$	4.8	0.9	-0.7	0.2	-2.9	0.4	0.2
Data Set 2							
$\Delta T = 10$	1.0	0.4	0.0	0.4	-1.3	0.1	0.2
$\Delta T = 20$	1.3	0.2	0.8	0.3	-1.7	0.1	0.2
$\Delta T = 30$	4.2	0.6	-0.6	0.2	-2.7	0.2	0.2
$\Delta T = 40$	4	1	-0.9	0.2	-2.2	0.3	0.2
$\Delta T = 55$	3.0	0.5	-0.4	0.2	-2.2	0.2	0.2
$\Delta T = 70$	2.3	0.3	0.0	0.2	-2.5	0.2	0.2
$\Delta T = 80$	6.1	0.6	-0.8	0.1	-3.6	0.4	0.2
$\Delta T = 90$	1.6	0.3	0.2	0.3	-2.2	0.1	0.1
$\Delta T = 110$	3.1	0.4	-0.3	0.2	-2.4	0.2	0.2
$\Delta T = 125$	2.0	0.4	0.0	0.3	-2.3	0.1	0.2
$\Delta T = 140$	2.2	0.4	-0.4	0.2	-2.3	0.1	0.2
$\Delta T = 155$	2.3	0.3	-0.1	0.2	-2.3	0.2	0.1
wind 600	5	1	-0.5	0.1	-1.5	0.3	0.2
wind 750	2.4	0.5	0.2	0.2	-1.4	0.2	0.2
wind 900	5	1	-0.3	0.1	-1.5	0.3	0.2
wind 105	6	2	-0.3	0.1	-1.3	0.3	0.2
wind 120	4.3	0.7	0.2	0.2	-1.4	0.2	0.4
bottom	0.8	0.5	?		-1.9	0.1	0.1

# Appendix D

## Data Tables: Spatial Parameters

This appendix contains all the parameters characterizing the spatial properties of the turbulence produced in the lab, calculated from the data taken from the mini-Wavescope and the PS with and without the diffuser. In all cases  $r_0$  is reported at a wavelength of 500 nm. Table D.1 gives the results of the PS without the diffuser. Tables D.2 and D.3 give the results of the Zernike2Seeing program and the Hill-Andrew model fit to the mini-Wavescope data. Spatial parameters were calculated for the PS in both the 7x7 and 14x14 configurations. Tables D.4 and D.5 give the 7x7 results and tables D.6 and D.7 give the 14x14 results. Both subaperture configurations were analyzed using Zernike2Seeing and the slope variance method.

The data for runs  $\Delta T = 5$  and  $\Delta T = 15$  for the PS was corrupted and no results could be obtained.

Table D.1: **Spatial Parameters Calculated using the PS with no diffuser:** The data collected using the PS with no diffuser for data set 1 was used to calculate the spatial parameters of the turbulence using the slope variance method. It was not possible to fit the outer scale for this data. See section 4.5 for details.

	$r_0$ (mm)	error (mm)	$l_0$ (mm)	error (mm)
$\Delta T = 10$	120	270	3.4	12
$\Delta T = 30$	12.1	2.5	4.1	0.9
$\Delta T = 40$	9.4	1.5	4.2	0.7
$\Delta T = 55$	6.5	0.6	3.5	0.5
$\Delta T = 140$	2.26	0.07	4.4	0.1
$\Delta T = 150$	2.24	0.07	4.5	0.1
$\Delta T = 160$	1.73	0.04	4.5	0.1

Table D.2: Zernike2Seeing Results, mini-Wavescope.

Data Set 1	best $r_0$ (mm)	mean $r_0$ (mm)	median $r_0$ (mm)	std. dev. $r_0$ (mm)	$L_0$ (mm)	std. dev. (mm)
$\Delta T = 10$	37	41	32	9	237	170
$\Delta T = 30$	9	11	7	4	172	142
$\Delta T = 40$	8	9	7	3	151	110
$\Delta T = 55$	9	12	9	5	618	540
$\Delta T = 140$	3.3	3.7	3.0	0.9	434	250
$\Delta T = 150$	3.3	3.7	3.1	0.8	432	230
$\Delta T = 160$	3.2	3.5	3.0	0.8	284	170
Data Set 2						
$\Delta T = 5$	34	35	34	3	205	74
$\Delta T = 10$	16	17	17	1	240.	77
$\Delta T = 15$	12	12	13	1	156	53
$\Delta T = 20$	8.1	8.3	8.6	0.6	248	94
$\Delta T = 30$	5.7	5.8	5.9	0.4	242	83
$\Delta T = 40$	5.1	5.2	5.0	0.3	213	51
$\Delta T = 55$	4.2	4.3	4.0	0.3	242	65
$\Delta T = 70$	3.9	4.0	3.6	0.3	244	76
$\Delta T = 80$	3.8	3.8	3.6	0.2	169	33
$\Delta T = 90$	4.0	4.1	3.8	0.4	170.	47
$\Delta T = 110$	3.7	3.8	3.6	0.4	197	64
$\Delta T = 125$	4.3	4.4	4.2	0.5	157	51
$\Delta T = 140$	4.2	4.3	4.1	0.5	150.	47
$\Delta T = 155$	5.2	5.4	5.1	0.8	131	45
wind 600	3.1	3.2	3.1	0.3	253	117
wind 750	2.9	3.0	2.9	0.2	218	70.
wind 900	3.0	3.0	2.8	0.3	177	59
wind 105	3.2	3.2	3.1	0.3	258	112
wind 120	3.1	3.2	3.0	0.4	222	97
bottom	3.9	4.1	3.9	0.6	136	68

Table D.3: Hill–Andrew Results, mini-Wavescope.

Data Set 1	$r_0$ (mm)	error (mm)	$L_0$ (mm)	error (mm)	$l_0$ (mm)	error (mm)
$\Delta T = 10$	40	20	200	700	10	4
$\Delta T = 30$	10.0	0.5	110	30	10.3	0.5
$\Delta T = 40$	8.5	0.6	80	20	10.7	0.4
$\Delta T = 55$	7.9	0.4	170	50	14.5	0.4
$\Delta T = 140$	3.40	0.03	170	10	11.57	0.07
$\Delta T = 150$	3.48	0.03	160	10	11.30	0.07
$\Delta T = 160$	3.34	0.03	130	7	11.30	0.07
Data Set 2						
$\Delta T = 5$	46	8	330	1400	6	2
$\Delta T = 10$	21	1	250	260	7.5	0.5
$\Delta T = 15$	15.2	0.6	168	95	7.72	0.3
$\Delta T = 20$	10.1	0.2	239	75	8.0	0.2
$\Delta T = 30$	7.1	0.08	200.	34	7.95	0.09
$\Delta T = 40$	6.3	0.07	160.	21.	8.11	0.08
$\Delta T = 55$	5.01	0.04	173	16	8.25	0.05
$\Delta T = 70$	4.76	0.03	191	16	8.17	0.05
$\Delta T = 80$	4.50	0.03	122	9	8.29	0.05
$\Delta T = 90$	4.79	0.04	124	9	8.27	0.05
$\Delta T = 110$	4.43	0.03	138	9	8.41	0.05
$\Delta T = 125$	4.98	0.05	95	7	8.31	0.06
$\Delta T = 140$	4.79	0.05	90.	6	8.55	0.06
$\Delta T = 155$	6.0	0.1	80.	7	8.48	0.09
wind 600	4.10	0.01	270	20	6.64	0.03
wind 750	3.77	0.01	190	10	6.13	0.03
wind 900	3.86	0.01	146	8	5.70	0.03
wind 105	4.09	0.01	170	10	5.24	0.03
wind 120	4.02	0.01	150.	9	5.2	0.03
bottom	4.92	0.04	116	9	8.07	0.06

Table D.4: Zernike2Seeing Results, PS 7x7.

PS with Diffuser Data Set 1	best $r_0$ (mm)	mean $r_0$ (mm)	median $r_0$ (mm)	std. dev. $r_0$ (mm)	$L_0$ (mm)	std. dev. (mm)
$\Delta T = 10$	16.8	17.6	14.1	6.2	75	54
$\Delta T = 30$	7.7	10.5	4.1	11.3	200	160
$\Delta T = 40$	4.8	4.9	4.2	2.0	47	26
$\Delta T = 55$	4.1	4.1	3.1	1.4	88	51
$\Delta T = 140$	1.9	2.1	1.6	1.0	56	39
$\Delta T = 150$	1.8	2.0	1.5	0.9	56	34
$\Delta T = 160$	1.9	2.0	1.4	0.9	52	35
Data Set 2						
$\Delta T = 10$	12.4	13.0	11.0	5.2	96	71
$\Delta T = 20$	6.2	6.5	6.0	2.4	88	59
$\Delta T = 30$	4.2	4.5	3.7	1.8	116	78
$\Delta T = 40$	3.7	3.8	3.3	1.3	104	68
$\Delta T = 55$	3.5	3.7	2.9	1.6	90.	59.
$\Delta T = 70$	2.9	3.0	2.4	1.1	119	78
$\Delta T = 80$	3.0	3.0	2.5	1.1	102	62
$\Delta T = 90$	3.6	3.9	2.6	1.9	106	70.1
$\Delta T = 110$	3.8	4.0	2.7	1.0	101	60.
$\Delta T = 125$	3.8	3.7	3.6	1.1	131	80
$\Delta T = 140$	5.7	5.9	5.1	2.4	131	80.
$\Delta T = 155$	4.5	4.4	4.4	1.1	134	84
wind 600	1.9	2.2	1.3	1.1	64	48
wind 750	2.6	3.1	2.1	1.9	64	47
wind 900	2.4	2.5	2.2	0.9	65	44
wind 105	2.6	3.1	1.4	2.1	71	53
wind 120	2.1	2.3	1.9	0.9	64	45
bottom	-	-	-	-	-	-

Table D.5: Slope Variance Parameters, PS 7x7: The fitting routine failed to fit the run 'bottom' from data set 2.

PS with Diffuser Data Set 1	$r_0$ (mm)	error (mm)	$L_0$ (mm)	error (mm)	$l_0$ (mm)	error (mm)
$\Delta T = 10$	26	7	100	200	5	3
$\Delta T = 30$	11	1	300	300	5	1
$\Delta T = 40$	6.3	0.9	50	20	6	1
$\Delta T = 55$	5.5	0.3	110	40		
$\Delta T = 140$	2.6	0.1	70	10	5.8	0.5
$\Delta T = 150$	2.6	0.1	70	10	5.0	0.6
$\Delta T = 160$	2.7	0.2	60	10	5.4	0.6
Data Set 2						
$\Delta T = 10$	10	10	100	100	1	6
$\Delta T = 20$	8	9	110	140	2	17
$\Delta T = 30$	5	2	150	70	2	7
$\Delta T = 40$	4.9	0.5	140	40	2	3
$\Delta T = 55$	4.5	0.3	120	30	3	2
$\Delta T = 70$	3	2	150	90	2	7
$\Delta T = 80$	3.7	0.3	130	30	2	2
$\Delta T = 90$	4.6	0.2	130	40	3	2
$\Delta T = 110$	4.9	0.2	120	40	4	1
$\Delta T = 125$	4.6	0.4	150	50	3	3
$\Delta T = 140$	7.2	0.4	160	80	3	2
$\Delta T = 155$	5	1	150	50	2	4
wind 600	2	2	50	20	2	10
wind 750	3	5	40	40	1	20
wind 900	2	4	40	30	1	20
wind 105	2	5	30	40	1	20
wind 120	2	3	40	30	1	20
bottom	-		-		-	

Table D.6: Zernike2Seeing Results, PS 14x14.

PS with Diffuser Data Set 1	best $r_0$ (mm)	mean $r_0$ (mm)	median $r_0$ (mm)	std. dev. $r_0$ (mm)	$L_0$ (mm)	std. dev. (mm)
$\Delta T = 10$	17.2	20.8	15.0	14.4	78	62
$\Delta T = 30$	7.1	7.4	6.1	2.7	163	114
$\Delta T = 40$	4.6	4.8	3.9	2.1	45	25
$\Delta T = 55$	3.9	3.8	3.0	1.2	82	44
$\Delta T = 140$	1.7	2.0	1.5	1.1	51	34
$\Delta T = 150$	1.7	1.8	1.4	0.8	51	29
$\Delta T = 160$	1.8	2.5	0.6	2.9	47	31
Data Set 2						
$\Delta T = 10$	12.1	12.6	9.4	5.5	88	55
$\Delta T = 20$	6.2	6.3	5.4	2.1	85	53
$\Delta T = 30$	4.1	4.2	3.4	1.4	108	69
$\Delta T = 40$	3.6	3.6	3.0	1.0	98	55
$\Delta T = 55$	3.4	3.4	2.9	1.2	85	52
$\Delta T = 70$	2.8	2.9	2.4	1.1	113	68
$\Delta T = 80$	2.9	2.8	2.5	0.8	96	54
$\Delta T = 90$	3.5	3.5	3.0	1.1	101	62
$\Delta T = 110$	3.7	3.7	2.9	1.3	95	54
$\Delta T = 125$	3.8	3.6	3.4	0.9	127	82
$\Delta T = 140$	5.6	5.5	5.5	1.6	126	77
$\Delta T = 155$	4.4	4.2	3.9	1.1	124	70
wind 600	1.9	2.0	1.5	0.9	63	41
wind 750	2.4	2.5	2.1	0.9	57	32
wind 900	2.4	2.4	2.3	0.9	67	41
wind 105	2.6	5.7	1.4	11.9	71	48
wind 120	2.2	2.3	1.8	0.9	65	42
bottom	0.2	3.9	2.2	4.2	980	<0.1

Table D.7: Slope Variance Parameters, PS 14x14.

PS with Diffuser Data Set 1	$r_0$ (mm)	error (mm)	$L_0$ (mm)	error (mm)	$l_0$ (mm)	error (mm)
$\Delta T = 10$	27	4	100	200	3.8	0.8
$\Delta T = 30$	10.0	0.7	300	200	4.4	0.3
$\Delta T = 40$	6.4	0.4	60	20	4.5	0.3
$\Delta T = 55$	4.9	0.2	80	20	4.3	0.2
$\Delta T = 140$	2.55	0.08	70.	9	4.6	0.1
$\Delta T = 150$	2.35	0.07	57	7	4.5	0.1
$\Delta T = 160$	2.54	0.08	58	7	4.6	0.1
Data Set 2						
$\Delta T = 10$	14	1	100	60	2.6	0.6
$\Delta T = 20$	7.6	0.4	90	30	3.1	0.3
$\Delta T = 30$	5.2	0.2	120	40	3.1	0.2
$\Delta T = 40$	4.6	0.2	110	30	3.3	0.2
$\Delta T = 55$	4.2	0.1	90	20	3.4	0.2
$\Delta T = 70$	3.4	0.1	120	20	3.3	0.1
$\Delta T = 80$	3.5	0.1	90	20	3.5	0.1
$\Delta T = 90$	4.2	0.2	90	20	3.7	0.2
$\Delta T = 110$	4.5	0.2	90	20	3.8	0.2
$\Delta T = 125$	4.3	0.2	110	30	3.5	0.2
$\Delta T = 140$	6.6	0.3	120	40	3.7	0.2
$\Delta T = 155$	5.1	0.2	110	30	3.6	0.2
wind 600	2.11	0.03	47	5.2	2.0	0.2
wind 750	2.5	0.3	38	4	1.1	0.8
wind 900	2.2	0.6	35	8	1	2
wind 105	2.2	0.9	30	10	1	3
wind 120	1.8	0.6	30	10	1	2
bottom	3.32	0.06	$\infty$	4.2	0.1	-

# Appendix E

## Other Data Products

Figure E.1 shows a plot of the variac setting's dependence on the fan speed, which is quite linear. Figures E.2 and E.3 show the temporal power spectra for each of the measured fan speeds at  $\Delta T \sim 40^\circ$ .

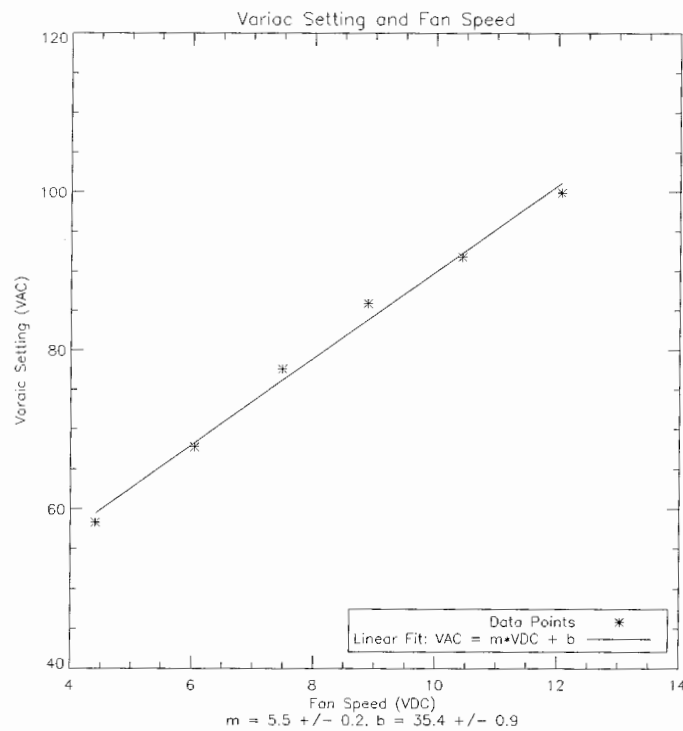
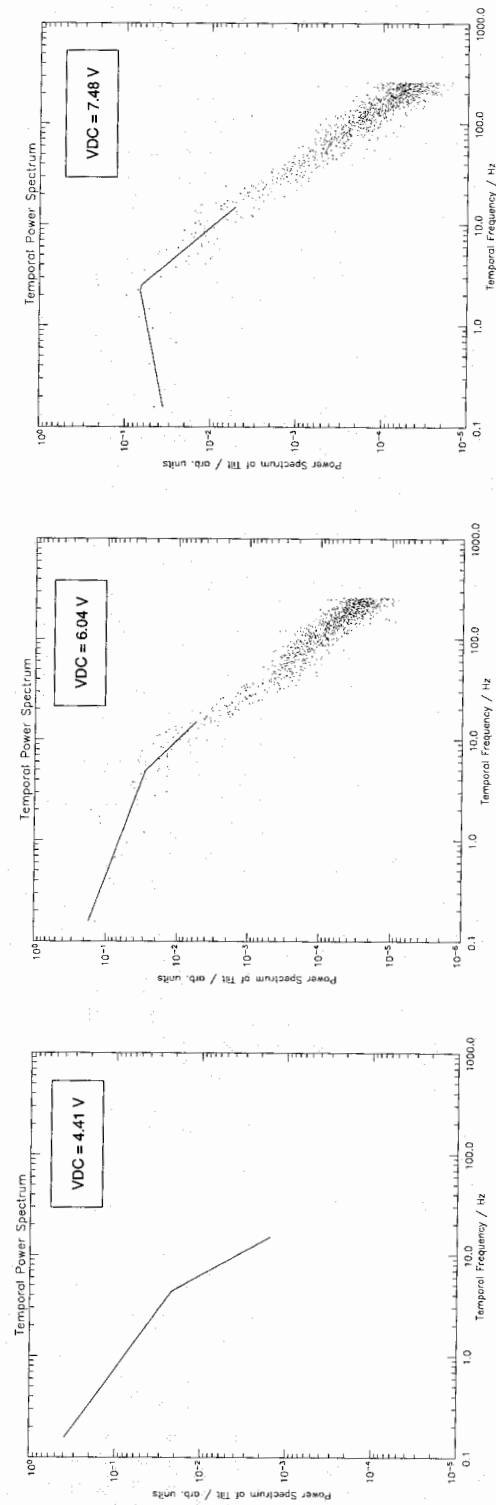


Figure E.1: **Variac setting dependence on fan speed ( $\Delta T \sim 40^\circ\text{C}$ ):** This plot shows the behaviour of the variac setting necessary to produce  $\Delta T \sim 40^\circ\text{C}$  for increasing fan speed. The relationship is remarkably linear with an  $R^2$  value of 0.992. This suggests that the heating curve has the same shape at every fan speed and the curve is simply shifted to higher VAC.



**Figure E.2: Temporal Power Spectra calculated for Runs  $\Delta T = 40, 600, 750$ :** This plot shows the first three runs of the set in which the fan speed was increased. The 'second layer' feature seen in all of the temporal power spectra is evident in the plot on the right corresponding to a fan voltage of 4.41 V. In the middle plot, at a voltage of 6.04 V, the feature is much less evident. In the right hand plot, at 7.48 V, the feature is no longer visible.

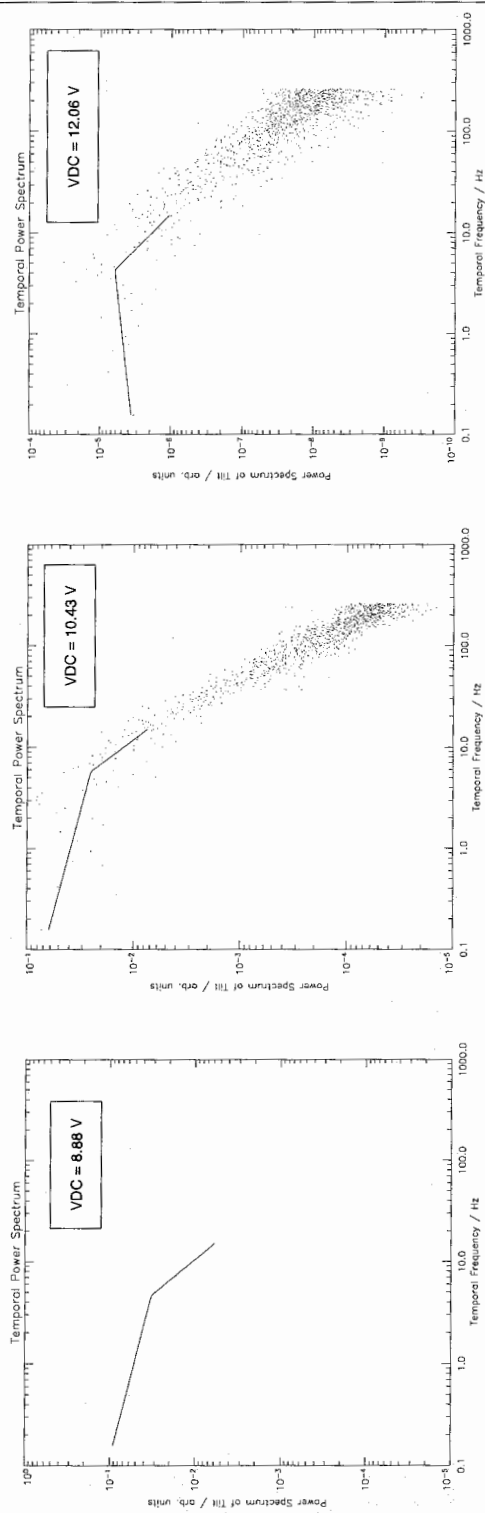


Figure E.3: Temporal Power Spectra calculated for Runs Wind 900, 105, 120: These plots show the temporal power spectra for the 3 highest fan voltages measured, 8.88 V, 10.45 V, and 12.06 V, from left to right. The feature 'second layer' feature is not apparent in any of these plots.

# Bibliography

- Andrews, L. C.: 1992, *Journal of Modern Optics* **39**, 1849
- Babcock, H. W.: 1953, *Publications of the Astronomical Society of the Pacific* **65**, 229
- Bahcall, J. N. and Soneira, R. M.: 1980, *Astrophysical Journal Supplement Series* **44**, 73
- Banerji, S.: 1918, *The Astrophysical Journal* **48**, 50
- Barakat, R.: 1969, *Journal of the Optical Society of America (1917-1983)* **59**, 1432
- Beckers, J. M.: 1988, in *Very Large Telescopes and their Instrumentation, ESO Conference and Workshop Proceedings, Proceedings of a ESO Conference on Very Large Telescopes and their Instrumentation, held in Garching, March 21-24, 1988, Garching: European Southern Observatory (ESO), 1988, edited by Marie-Helene Ulrich., p.693*, pp 693–703
- Beckers, J. M.: 1989, in *Proc. SPIE Vol. 1114, p. 215-0, Active Telescope Systems, Francois J. Roddier; Ed.*, pp 215–217
- Beckers, J. M.: 1993, *Annual Reviews of Astronomy and Astrophysics* **31**, 13
- Binggeli, B., Sandage, A., and Tammann, G. A.: 1985, *The Astronomical Journal* **90**, 1681
- Bloemhof, E. E. and Wallace, J. K.: 2003, in *Astronomical Adaptive Optics Systems and Applications. Edited by Tyson, Robert K.; Lloyd-Hart, Michael. Proceedings of the SPIE, Volume 5169, pp. 309-320 (2003).*, pp 309–320
- Bloemhof, E. E. and Westphal, J. A.: 2002, in *Proc. SPIE Vol. 4494, p. 363-370, Adaptive Optics Systems and Technology II, Robert K. Tyson; Domenico Bonaccini; Michael C. Roggemann; Eds.*, pp 363–370
- Bracewell, R.: 1978, *The Fourier transform and its Applications*, McGraw Hill Series

- in *Electrical Engineering*, McGraw Hill Book Company, second edition
- Cannon, R.: 1996, *Journal of the Optical Society of America A* **13**, 862
- Carbillet, M., Fini, L., Femenía, B., Riccardi, A., Esposito, S., Viard, É., Delplancke, F., and Hubin, N.: 2001, in *ASP Conf. Ser. 238: Astronomical Data Analysis Software and Systems X*, p. 249
- Carbillet, M., Vérinaud, C., Femenía, B., Riccardi, A., and Fini, L.: 2005, *Monthly Notices of the Royal Astronomical Society* **356**, 1263
- Carhart, G. W., Vorontsov, M. A., and Justh, E. W.: 2000, in *Proc. SPIE Vol. 4124, p. 138-147, High-Resolution Wavefront Control: Methods, Devices, and Applications II*, John D. Gonglewski; Mikhail A. Vorontsov; Mark T. Gruneisen; Eds., pp 138–147
- CASCA: 2005, *Long Range Plan: Mid-Term Review*
- Clare, R. and Lane, R.: 2005, *Journal of the Optical Society of America, A* **22**, 117
- Conan, J.: 1980, Ph.D. Dissertation, ONERA
- Conan, R.: 2004, Private Communication
- Conan, R., Avila, R., Sánchez, L. J., Ziad, A., Martin, F., Borgnino, J., Harris, O., González, S. I., Michel, R., and Hiriart, D.: 2002, *Astronomy and Astrophysics* **396**, 723
- Conan, R., Le Louarn, M., Braud, J., Fedrigo, E., and Hubin, N. N.: 2003, in *Future Giant Telescopes. Edited by Angel, J. Roger P.; Gilmozzi, Roberto. Proceedings of the SPIE, Volume 4840, pp. 393-403 (2003).*, pp 393–403
- Costa, J. B., Feldt, M., Wagner, K., Bizenberger, P., Hippler, S., Baumeister, H., Stumpf, M., Ragazzoni, R., Esposito, S., and Henning, T.: 2004a, in *ALT'03 International Conference on Advanced Laser Technologies: Biomedical Optics. Edited by Wang, Ruikang K.; Hebden, Jeremy C.; Priezhev, Alexander V.; Tuchin, Valery V. Proceedings of the SPIE, Volume 5490, pp. 1189-1199 (2004).*, pp 1189–1199
- Costa, J. B., Hippler, S., Feldt, M., Esposito, S., Ragazzoni, R., Bizenberger, P., Puga, E., and Henning, T. F. E.: 2003a, in *Adaptive Optical System Technologies II. Edited by Wizinowich, Peter L.; Bonaccini, Domenico. Proceedings of the SPIE, Volume 4839, pp. 280-287 (2003).*, pp 280–287
- Costa, J. B., Ragazzoni, R., Ghedina, A., Carbillet, M., Vérinaud, C., Feldt, M., Esposito, S., Puga, E., and Farinato, J.: 2003b, in *Adaptive Optical System Tech-*

- nologies II. Edited by Wizinowich, Peter L.; Bonaccini, Domenico. Proceedings of the SPIE, Volume 4839, pp. 288-298 (2003).*, pp 288–298
- Costa, J. B., Stumpf, M., and Feldt, M.: 2004b, in *ALT'03 International Conference on Advanced Laser Technologies: Biomedical Optics. Edited by Wang, Ruikang K.; Hebden, Jeremy C.; Priezhev, Alexander V.; Tuchin, Valery V. Proceedings of the SPIE, Volume 5490, pp. 1304-1314 (2004).*, pp 1304–1314
- Crampton, D.: 1999, *Journal of the Royal Astronomical Society of Canada* **93**, 168
- Diolaiti, E., Ragazzoni, R., and Tordi, M.: 2001, *Astronomy and Astrophysics* **372**, 710
- Diolaiti, E., Tozzi, A., Ragazzoni, R., Ferruzzi, D., Vernet-Viard, E., Esposito, S., Farinato, J., Ghedina, A., and Riccardi, A.: 2003, in *Adaptive Optical System Technologies II. Edited by Wizinowich, Peter L.; Bonaccini, Domenico. Proceedings of the SPIE, Volume 4839, pp. 299-306 (2003).*, pp 299–306
- Ellerbroek, B. L.: 1994, *Optical Society of America Journal A* **11**, 783
- Ellerbroek, B. L. and Tyler, D. W.: 1998, *Publications of the Astronomical Society of the Pacific* **110**, 165
- Esposito, S. and Devaney, N.: 2002, in *Beyond conventional adaptive optics : a conference devoted to the development of adaptive optics for extremely large telescopes. Proceedings of the Topical Meeting held May 7-10, 2001, Venice, Italy. Edited by E. Vernet, R. Ragazzoni, S. Esposito, and N. Hubin. Garching, Germany: European Southern Observatory, 2002 ESO Conference and Workshop Proceedings, Vol. 58, ISBN 3923524617, p. 161*, p. 161
- Esposito, S., Feeney, O., and Riccardi, A.: 2000a, in *Proc. SPIE Vol. 4007, p. 416-422, Adaptive Optical Systems Technology, Peter L. Wizinowich; Ed.*, pp 416–422
- Esposito, S., Pinna, E., Tozzi, A., Stefanini, P., and Devaney, N.: 2003, in *Astronomical Adaptive Optics Systems and Applications. Edited by Tyson, Robert K.; Lloyd-Hart, Michael. Proceedings of the SPIE, Volume 5169, pp. 72-78 (2003).*, pp 72–78
- Esposito, S. and Riccardi, A.: 2001, *Astronomy and Astrophysics* **369**, L9
- Esposito, S., Riccardi, A., and Feeney, O.: 2000b, in *Proc. SPIE Vol. 4034, p. 184-189, Laser Weapons Technology, Todd D. Steiner; Paul H. Merritt; Eds.*, pp 184–189
- Femenia, B., Carbillet, M., Riccardi, A., Esposito, S., and Brusa, G.: 2002, in *Proc.*

- SPIE Vol. 4494, p. 132-143, Adaptive Optics Systems and Technology II, Robert K. Tyson; Domenico Bonaccini; Michael C. Roggemann; Eds.*, pp 132–143
- Femenía, B. and Devaney, N.: 2003, *Astronomy and Astrophysics* **404**, 1165
- Fontanella, J.: 1985, *Journal of Optics, Paris* **16**, 257
- Foy, R. and Labeyrie, A.: 1985, *Astronomy and Astrophysics* **152**, L29
- Fried, D. L.: 1966, *Optical Society of America Journal* **56**, 1372
- Fried, D. L.: 1982, *Journal of the Optical Society of America (1917-1983)* **72**, 52
- Gascoigne, S. C. B.: 1944, *Monthly Notices of the Royal Astronomical Society* **104**, 326
- Gavazzi, G., Boselli, A., Donati, A., Franzetti, P., and Scodreggio, M.: 2003, *Astronomy and Astrophysics* **400**, 451
- Ghedina, A., Cecconi, M., Ragazzoni, R., Farinato, J., Baruffolo, A., Crimi, G., Diolaiti, E., Esposito, S., Fini, L., Ghigo, M., Marchetti, E., Niero, T., and Puglisi, A.: 2003, in *Adaptive Optical System Technologies II. Edited by Wizinowich, Peter L.; Bonaccini, Domenico. Proceedings of the SPIE, Volume 4839, pp. 869-877 (2003).*, pp 869–877
- Goodman, J.: 1996, *Introduction to Fourier Optics*, McGraw-Hill Electrical and Computer Engineering Series, McGraw-Hill Companies, Inc., second edition
- Gwyn, S.: 2005, Private Communication
- Hammer, F., Puech, M., Assemat, F. F., Gendron, E., Sayède, F., Laporte, P., Marteaud, M., Liotard, A., and Zamkotsian, F.: 2004, in *Emerging Optoelectronic Applications. Edited by Jabbour, Ghassan E.; Rantala, Juha T. Proceedings of the SPIE, Volume 5382, pp. 727-736 (2004).*, pp 727–736
- Hampton, P., Veran, J., Bradley, C., Hilton, A., and Agathoklis, P.: 2003, in *Astronomical Adaptive Optics Systems and Applications. Edited by Tyson, Robert K.; Lloyd-Hart, Michael. Proceedings of the SPIE, Volume 5169, pp. 321-330 (2003).*, pp 321–330
- Hampton, P. J., Bradley, C., Hilton, A., and Agathoklis, P.: 2004, in *ALT'03 International Conference on Advanced Laser Technologies: Biomedical Optics. Edited by Wang, Ruikang K.; Hebden, Jeremy C.; Priezzhev, Alexander V.; Tuchin, Valery V. Proceedings of the SPIE, Volume 5490, pp. 1374-1383 (2004).*, pp 1374–1383
- Herriot, G., Morris, S., Roberts, S., Fletcher, J. M., Saddlemyer, L. K., Singh, G., Veran, J., and Richardson, E. H.: 1998, in *Proc. SPIE Vol. 3353, p. 488-499*,

- Adaptive Optical System Technologies*, Domenico Bonaccini; Robert K. Tyson; Eds., pp 488–499
- Hickson, P.: 1994, *Optical Society of America Journal A* **11**, 1667
- Hickson, P. and Burley, G.: 1994, in *Proc. SPIE Vol. 2201*, p. 549-554, *Adaptive Optics in Astronomy*, Mark A. Ealey; Fritz Merkle; Eds., pp 549–554
- Horwitz, B. A.: 1978, *Applied Optics* **17**, 181
- Horwitz, B. A.: 1994, in *Proc. SPIE Vol. 2201*, p. 496-501, *Adaptive Optics in Astronomy*, Mark A. Ealey; Fritz Merkle; Eds., pp 496–501
- Innocenti, C. and Consortini, A.: 2004, *Journal of Modern Optics* **51**, 333
- Johnston, D. C. and Welsh, B. M.: 1994, *Optical Society of America Journal A* **11**, 394
- Jolissaint, L.: 2000, Ph.D. Dissertation, Université de Genève
- Jolissaint, L.: 2003, *PAOLA version 2.3.3 User Manual*, Technical report, HIA
- Jolissaint, L., Keskin, O., Bradley, C., Wallace, B., and Hilton, A.: 2004a, in *Remote Sensing of Clouds and the Atmosphere IX*. Edited by Schäfer, Klaus P.; Comerón, Adolfo; Carleer, Michel R.; Picard, Richard H.; Sifakis, Nicolaos I. *Proceedings of the SPIE, Volume 5572*, pp. 256-261 (2004)., pp 256–261
- Jolissaint, L., Véran, J., and Stoesz, J. A.: 2004b, in *Emerging Optoelectronic Applications*. Edited by Jabbour, Ghassan E.; Rantala, Juha T. *Proceedings of the SPIE, Volume 5382*, pp. 468-477 (2004)., pp 468–477
- Jolissaint, L., Veran, J., and Marino, J.: 2004c, in *ALT'03 International Conference on Advanced Laser Technologies: Biomedical Optics*. Edited by Wang, Ruikang K.; Hebden, Jeremy C.; Priezhev, Alexander V.; Tuchin, Valery V. *Proceedings of the SPIE, Volume 5490*, pp. 151-163 (2004)., pp 151–163
- Jolissaint, L., Véran, J.-P., and Conan, R.: 2005, *Submitted to the Journal of the Optical Society of America, A* **47**, 47
- Keskin, O.: 2003, M.Sc. Thesis, University of Victoria
- Keskin, O.: 2004, Private Communication
- Keskin, O., Jolissaint, L., Bradley, C., Dost, S., and Sharf, I.: 2003, in *Advanced Wavefront Control: Methods, Devices, and Applications*. Edited by Gonglewski, John D.; Vorontsov, Mikhail A.; Gruneisen, Mark T. *Proceedings of the SPIE, Volume 5162*, pp. 49-57 (2003)., pp 49–57
- Kirk, A., Logiudice, V., and Grütter, P.: 2004, Private Communication

- Le Louarn, M.: 2002, *Monthly Notices of the Royal Astronomical Society* **334**, 865
- Le Louarn, M., Hubin, N., Sarazin, M., and Tokovinin, A.: 2000, *Monthly Notices of the Royal Astronomical Society* **317**, 535
- Linfoot, E. H.: 1946, *Proceedings of the Royal Society of London. Series A, Mathematical and Physical Sciences* **186**, 72
- Linfoot, E. H.: 1948a, *Proceedings of the Royal Society of London. Series A, Mathematical and Physical Sciences* **193**, 248
- Linfoot, E. H.: 1948b, *Monthly Notices of the Royal Astronomical Society* **108**, 428
- Lombini, M., Ragazzoni, R., Arcidiacono, C., Baruffolo, A., Bisson, R., Brindisi, A., Coyne, J., Diolaiti, E., Farinato, J., Le Roux, B., Lombardi, G., Marchetti, E., Meneghini, G., Vernet-Viard, E., and Kompero, M.: 2004, in *ALT'03 International Conference on Advanced Laser Technologies: Biomedical Optics*. Edited by Wang, Ruikang K.; Hebden, Jeremy C.; Priezhev, Alexander V.; Tuchin, Valery V. *Proceedings of the SPIE, Volume 5490*, pp. 1247-1255 (2004)., pp 1247–1255
- Malacara, D. (ed.): 1978, *Optical Shop Testing*, Wiley Series in Pure and Applied Optics, John Wiley and Sons
- Markwardt, C.: 1997-2004, *IDL Curve Fitting and Function Optimization*, webpage, [cow.physics.wisc.edu/craigm/idl/fitting.html](http://cow.physics.wisc.edu/craigm/idl/fitting.html)
- Merkle, F. and Beckers, J. M.: 1989, in *Active telescope systems; Proceedings of the Meeting, Orlando, FL, Mar. 28-31, 1989 (A90-30852 12-74)*. Bellingham, WA, Society of Photo-Optical Instrumentation Engineers, 1989, p. 36-42., pp 36–42
- Murphy, D. V., Primmerman, C. A., Zollars, B. G., and Barclay, H. T.: 1991, *Optics Letters* **16**, 1797
- Noll, R. J.: 1976, *Optical Society of America Journal* **66**, 207
- Perennes, F., De Bona, F., and Pantenburg, F. J.: 2001, *Nuclear Instruments and Methods in Physics Research* **467-8**, 1274
- Perennes, F., Ghigo, M., and Cabrini, S.: 2003, *Microelectronic Engineering* **67-68**, 566
- Platzeck, R. and Gaviola, E.: 1939, *Journal of the Optical Society of America (1917-1983)* **29**, 484
- Pugh, W. N., Lobb, D. R., Walker, D. D., and Williams, T. L.: 1995, in *Proc. SPIE Vol. 2534, p. 312-317, Adaptive Optical Systems and Applications*, Robert K. Tyson; Robert Q. Fugate; Eds., pp 312–317

- Ragazzoni, R.: 1996, *Journal of Modern Optics* **43**, 289
- Ragazzoni, R.: 1999, *Astronomy and Astrophysics Supplement Series* **136**, 205
- Ragazzoni, R.: 2000, in *Proceedings of the Backaskog workshop on extremely large telescopes*, pp 175–180
- Ragazzoni, R.: 2004, Private Communication
- Ragazzoni, R., Baruffolo, A., Diolaiti, E., Esposito, S., Falomo, R., Farinato, J., Fedrigo, E., Marchetti, E., Tordi, M., and Viard, E.: 2001, *A Layer-Oriented Wavefront Sensor for MAD aboard VLT*, Technical report, ESO
- Ragazzoni, R., Diolaiti, E., Farinato, J., Fedrigo, E., Marchetti, E., Tordi, M., and Kirkman, D.: 2002a, *Astronomy and Astrophysics* **396**, 731
- Ragazzoni, R., Diolaiti, E., and Vernet, E.: 2002b, *Optics Communications* **208**, 51
- Ragazzoni, R. and Farinato, J.: 1999, *Astronomy and Astrophysics* **350**, L23
- Ragazzoni, R., Farinato, J., and Marchetti, E.: 2000a, in *Proc. SPIE Vol. 4007, p. 1076-1087, Adaptive Optical Systems Technology*, Peter L. Wizinowich; Ed., pp 1076–1087
- Ragazzoni, R., Ghedina, A., Baruffolo, A., Marchetti, E., Farinato, J., Niero, T., Crimi, G., and Ghigo, M.: 2000b, in *Proc. SPIE Vol. 4007, p. 423-430, Adaptive Optical Systems Technology*, Peter L. Wizinowich; Ed., pp 423–430
- Ragazzoni, R., Marchetti, E., and Rigaut, F.: 1999, *Astronomy and Astrophysics* **342**, L53
- Ragazzoni, R., Marchetti, E., and Valente, G.: 2000c, *Nature* **403**, 54
- Rayleigh: 1917, *Philosophical Magazine* **33**, 161
- Ribak, E. N.: 1995, in *Proc. SPIE Vol. 2580, p. 166-172, Optics in Atmospheric Propagation and Adaptive Systems*, Anton Kohnle; Ed., pp 166–172
- Riccardi, A., Bindi, N., Ragazzoni, R., Esposito, S., and Stefanini, P.: 1998, in *Proc. SPIE Vol. 3353, p. 941-951, Adaptive Optical System Technologies*, Domenico Bonaccini; Robert K. Tyson; Eds., pp 941–951
- Rigaut, F.: 2002, in *Beyond conventional adaptive optics : a conference devoted to the development of adaptive optics for extremely large telescopes. Proceedings of the Topical Meeting held May 7-10, 2001, Venice, Italy. Edited by E. Vernet, R. Ragazzoni, S. Esposito, and N. Hubin. Garching, Germany: European Southern Observatory, 2002 ESO Conference and Workshop Proceedings, Vol. 58, ISBN 3923524617, p.11*, pp 11–16

- Rigaut, F. and Gendron, E.: 1992, *Astronomy and Astrophysics* **261**, 677
- Rigaut, F., Kern, P., Lena, P., Rousset, G., Fontanella, J. C., Gaffard, J. P., and Merkle, F.: 1991, *Astronomy and Astrophysics* **250**, 280
- Rigaut, F., Ragazzoni, R., Chun, M., and Mountain, M.: 2000, in *Proceedings of the Backaskog workshop on extremely large telescopes*, p. 168
- Rigaut, F. J., Veran, J., and Lai, O.: 1998, in *Proc. SPIE Vol. 3353, p. 1038-1048, Adaptive Optical System Technologies, Domenico Bonaccini; Robert K. Tyson; Eds.*, pp 1038–1048
- Rousset, G.: 1999, *Wavefront Sensors, Chapter 5 of Adaptive Optics in Astronomy*, Cambridge University Press
- Sprague, R. and Thompson, B.: 1972, *Applied Optics* **11**, 1469
- Stoesz, J. A., Jolissaint, L., Veran, J., and LeDue, J.: 2004a, in *ALT'03 International Conference on Advanced Laser Technologies: Biomedical Optics. Edited by Wang, Ruikang K.; Hebden, Jeremy C.; Priezhev, Alexander V.; Tuchin, Valery V. Proceedings of the SPIE, Volume 5490, pp. 713-720 (2004).*, pp 713–720
- Stoesz, J. A., Veran, J., Rigaut, F. J., Herriot, G., Jolissaint, L., Frenette, D., Dunn, J., and Smith, M.: 2004b, in *ALT'03 International Conference on Advanced Laser Technologies: Biomedical Optics. Edited by Wang, Ruikang K.; Hebden, Jeremy C.; Priezhev, Alexander V.; Tuchin, Valery V. Proceedings of the SPIE, Volume 5490, pp. 67-78 (2004).*, pp 67–78
- Tallon, M. and Foy, R.: 1990, *Astronomy and Astrophysics* **235**, 549
- Tatarskii, V.: 1971, *The Effects of the Turbulent Atmosphere on Wave Propagation*, Isreal Program for Scientific Translations, Keter Press
- Tokovinin, A. and Viard, E.: 2001, *Optical Society of America Journal A* **18**, 873
- Tyson, R.: 1998, *Principles of Adaptive Optics*, Academic press, second edition
- Vérinaud, C.: 2004, *Optics Communications* **233**, 27
- Vérinaud, C., Arcidiacono, C., Carbillet, M., Diolaiti, E., Ragazzoni, R., Vernet-Viard, E., and Esposito, S.: 2003, in *Adaptive Optical System Technologies II. Edited by Wizinowich, Peter L.; Bonaccini, Domenico. Proceedings of the SPIE, Volume 4839, pp. 524-535 (2003).*, pp 524–535
- Vérinaud, C. and Esposito, S.: 2002, in *Beyond conventional adaptive optics : a conference devoted to the development of adaptive optics for extremely large telescopes. Proceedings of the Topical Meeting held May 7-10, 2001, Venice, Italy. Edited by*

- E. Vernet, R. Ragazzoni, S. Esposito, and N. Hubin. Garching, Germany: European Southern Observatory, 2002 ESO Conference and Workshop Proceedings, Vol. 58, ISBN 3923524617, p. 153, p. 153*
- Vérinaud, C.: 2004, Private Communication
- von der Lühe, O.: 1988, *Optical Engineering* **27**, 1078
- Vorontsov, M. A., Justh, E. W., and Beresnev, L. A.: 2000, in *Proc. SPIE Vol. 4124, p. 98-109, High-Resolution Wavefront Control: Methods, Devices, and Applications II, John D. Gonglewski; Mikhail A. Vorontsov; Mark T. Gruneisen; Eds., pp 98-109*
- Wallace, B.: 2005, M.Sc. Thesis, University of Victoria
- Weisstein, E.: 1999-2005, *Fourier Transform*, From MathWorld—A Wolfram Web Resource., <http://mathworld.wolfram.com/FourierTransform.html>
- Welford, W. T.: 1970, *Optics Communications* **1**, 443
- Wilson, R. G.: 1975, *Applied Optics* **14**, 2286
- Winker, D. M.: 1991, *Optical Society of America Journal A* **8**, 1568
- Wizinowich, P., Acton, D. S., Shelton, C., Stomski, P., Gathright, J., Ho, K., Lupton, W., Tsubota, K., Lai, O., Max, C., Brase, J., An, J., Avicola, K., Olivier, S., Gavel, D., Macintosh, B., Ghez, A., and Larkin, J.: 2000, *Publications of the Astronomical Society of the Pacific* **112**, 315
- Zernike, F.: 1934, *Monthly Notices of the Royal Astronomical Society* **94**, 377
- Ziad, A.: 2002, Private Communication to L. Jolissaint